UNIVERSITY OF CALIFORNIA,
IRVINE

Design and phase stability of high entropy alloys for structural applications

DISSERTATION

submitted in partial satisfaction of the requirements
for the degree of

DOCTOR OF PHILOSOPHY

in Materials Science and Engineering

by

Benjamin Erich MacDonald

Dissertation Committee:
Professor Timothy J. Rupert, Chair
Professor Julie M. Schoenung
Professor Daniel R. Mumm

2020

DEDICATION

Dedicated to the Loving Memory of my Grandmother,

Shel Jensen

She was and always will be a motivating force in my life to work hard and remain patient. Shel developed exceptional skills in quilting using her eye for detail and a perfectionist's mindset, both of which I strive for when conducting research.

I am immensely grateful for the time I had to say goodbye, and I will forever uphold my promise to make you proud.

Love you Grandmama

TABLE OF CONTENTS

LIST OF FIGURES ..... *vi*

LIST OF TABLES ..... *x*

ACKNOWLEDGEMENTS ..... *xi*

CURRICULUM VITAE ..... *xix*

ABSTRACT OF THE DISSERTATION ..... *xxiv*

Chapter 1 : Introduction to high entropy alloy design *1*

1.1 Overview **1**

1.2 Emergence of high entropy alloys **2**

1.3 The four core effects **3**

1.3.1 The high entropy effect **4**

1.3.2 Severe lattice distortion **5**

1.3.3 Sluggish diffusion **6**

1.3.4 Cocktail effect **8**

1.4 High entropy alloy definition **8**

1.5 Classification of high entropy alloys **9**

1.5.1 Standout 3d-transition metal high entropy alloys **9**

1.5.2 Standout refractory metal high entropy alloys **11**

1.6 Modeling high entropy alloys **12**

1.7 Dissertation objectives **16**

Chapter 2 : Influence of phase decomposition on mechanical behavior of an equiatomic CoCuFeMnNi high entropy alloy *18*

2.1 Background **18**

2.2 Experimental methods **21**

2.2.1 Material preparation **21**

2.2.2 Mechanical testing **22**

2.2.3 Microstructural characterization **22**

2.2.4 Computational thermodynamics **23**

2.3 Results **23**

2.3.1 Homogenization of the as-cast microstructure **23**

2.3.2 Cold rolled and 0.5 hour post deformation annealing treatments **26**

2.3.2.1 Evolution of tensile behavior 26
2.3.2.2 X-ray diffraction 27
2.3.2.3 Microstructural analysis of post deformation annealing treatments 28
2.3.3 Extended post deformation annealing treatments 31
2.3.3.1 600 °C 32
2.3.3.2 800 °C 34
2.4 Discussion 35
2.4.1 Phase decomposition 35
2.4.2 Mechanical behavior 40
2.5 Summary 43
Chapter 3 : Influence of constituent element concentration on the mechanical behavior of solid solution CoCuFeMnNi high entropy alloys 45
3.1 Background 45
3.2 Experimental methods 46
3.3 Results and discussion 47
3.3.1 Microstructural evolution 48
3.3.2 Mechanical behavior 53
3.4 Summary 57
Chapter 4 : Influence of phase decomposition on mechanical behavior in a nanocrystalline non-equiatomic CoCuFeMnNi high entropy alloy 59
4.1. Background 59
4.2. Experimental methods 61
4.2.1. Computational thermodynamics 61
4.2.2. Material preparation 61
4.2.3. Differential scanning calorimetry 62
4.2.4. Microstructural characterization 62
4.2.5. Mechanical testing 64
4.3. Results 64
4.3.1. Microstructural analysis of as-homogenized and as-HPT state 64
4.3.2. Thermodynamic calculations and thermal analysis 66
4.3.3. Microstructural analysis of the post deformation heat treatments 68

4.3.4. Tensile properties 73
4.4. Discussion 75
4.4.1. Phase stability 75
4.4.2. Mechanical behavior 78
4.5. Summary 79
Chapter 5 : CALPHAD aided prediction of phase stability in the AlMoNbTiZr refractory high entropy alloy system 81
5.1. Background 81
5.2. Experimental methods 82
5.3. Results and discussion 83
5.3.1. CALPHAD prediction of the AlMoNbTiZr system 83
5.3.2. First batch compositional deviation and CALPHAD validation 86
5.3.3. Phase formation and thermal stability in candidate compositions 95
5.3.4. Influence of Al content on mechanical behavior 100
5.4. Summary 101
Chapter 6 : Conclusions 103
Chapter 7 : Recommendations for further research 107
REFERENCES 110

LIST OF FIGURES

Figure 1. Schematic illustration of the random solid solution structure unique to HEAs composed of arbitrary elements A, B, C, D, and E organized on a distorted face centered cubic crystal structure reprinted from reference [17]. 3

Figure 2. Schematic plot of the site energy along an arbitrary diffusional path in pure elements or dilute solid solutions as opposed to HEAs, reprinted from reference [15]..... 7

Figure 3. Ashby map presenting fracture toughness as a function of tensile yield strength including HEAs and many other material systems, reprinted from reference [25]. 11

Figure 4. Compressive strength as a function of temperature for ten published HEA compositions compared with tensile strength as a function of temperature for three commercially available superalloys, reprinted from reference [16]. 12

Figure 5. A schematic flow diagram of the CALPHAD assessment approach, reprinted from reference [28]. 15

Figure 6. Microstructural analysis for the as-cast and homogenized samples of the equiatomic CoCuFeMnNi alloy including (a) the XRD pattern of the as-cast equiatomic CoCuFeMnNi alloy exhibiting two overlapping sets of FCC peaks, (b) a BSE micrograph of the as-cast state that reveals low Z contrast Cu-lean dendritic regions and high Z contrast Cu-rich interdendritic region, (c) the XRD pattern demonstrating a single FCC phase after hot rolling and homogenization of the as-cast material, (d) a BSE micrograph showing equiaxed grains after homogenization, (e) TEM micrograph of a triple junction of grains in the homogenized sample along with a SAED pattern of the highlighted area indexed to the FCC [011] zone axis, and (f) STEM EDS of the homogenized sample that exhibits a uniform distribution of all five constituent elements. 25

Figure 7. (a) Comparison of the tensile engineering stress-strain curves for the as-cast and homogenized samples, (b) plot of the average yield strength, ultimate tensile strength, and strain at failure for the cold rolled sample and 0.5 hour PDA annealing treatments, and (c) engineering stress-strain curves for the cold rolled, 600°C, 800°C, and 900°C 0.5 hour PDA annealing treatments. 26

Figure 8. (a) XRD patterns of the cold rolled sample and samples PDA treated for 0.5 hours at a range of temperatures (b) magnified view of 70° to 80° to show the (220) peak evolution..... 28

Figure 9. (a) BSE micrograph of the overall deformed microstructure present in the equiatomic CoCuFeMnNi alloy cold rolled after PDA treated at 600 °C for 0.5 hours, (b-g) STEM EDS analysis of particles observed within the deformed microstructure..... 29

Figure 10. (a) BSE micrograph of the overall deformed microstructure persisting in the equiatomic CoCuFeMnNi alloy cold rolled after PDA treated at 800°C for 0.5 hours, (b-g) STEM EDS analysis of recrystallized nuclei found within the deformed microstructure. 30

Figure 11. SEM EDS analysis of the equiatomic CoCuFeMnNi alloy cold rolled and PDA treated at 900°C for 0.5 hours. 31

Figure 12. Results of extended time PDA treatments at 600 °C (a) XRD patterns of the cold rolled sample and PDA treated samples at 600°C for 0.5, 2. and 24 hour, (b) tensile engineering stress-strain curves of the cold rolled sample and PDA treated samples at 600°C for 0.5, 2. and 24 hours, and STEM EDS and SAED analysis at a previous grain boundary in the equiatomic CoCuFeMnNi alloy cold rolled and PDA treated at 600°C for 24 hours, (c) STEM micrograph of the previous grain boundary, (d) EDS concentration map for Fe revealing B2 phases, (e) the SAED of the Fe-Co rich precipitate labelled B2 in (c), (f) EDS concentration map for Cu revealing nuclei of Cu-rich FCC phase, (g) EDS concentration map for Ni confirming the segregation of Ni in the phases present, (h) SAED of the Cu-Mn rich nucleated grain labelled Cu-rich FCC in (c). 32

Figure 13. Results of extended time PDA treatments at 800 °C (a) XRD patterns of the cold rolled sample and PDA treated samples at 800°C for 0.5, 2. and 24 hours, (b) tensile engineering stress-strain curves of the cold rolled sample and PDA treated samples at 800°C for 0.5, 2. and 24 hours, and BSE micrographs of the equiatomic CoCuFeMnNi alloy cold rolled sample PDA treated at 800°C for 24 hours (c) low magnification and (d) high magnification. 35

Figure 14. (a) Equilibrium step diagram of the equiatomic CoCuFeMnNi alloy from 400°C to 1600°C calculated by the CALPHAD approach using ThermoCalc software with the TCHEA 3.0 database and a comparison of phase composition experimentally measured from STEM EDS of the equiatomic CoCuFeMnNi alloy cold rolled sample PDA treated at 600°C for 24 hours and predicted from equilibrium CALPHAD calculations for the alloy at 500°C where all three phases are predicted (b) Fe-Co rich B2 phase, (c) Cu-rich FCC phase, and (d) the matrix FCC phase. . 40

Figure 15. XRD patterns of the as-HPT state for both the non-equiatomic (top) and equiatomic (bottom) compositions exhibiting broad peaks corresponding to a single FCC phase. 49

Figure 16. XRD patterns of the samples heat treated at 1000 °C for 30 minutes after HPT (HPT + HT) for both the non-equiatomic (top) and equiatomic (bottom) compositions exhibiting narrow peaks corresponding to a single FCC phase. 51

Figure 17. BSE micrographs of (a) the equiatomic composition heat treated after HPT and (b) the non-equiatomic composition heat treated after HPT revealing grain morphology through channeling contrast. 52

Figure 18. Representative engineering stress-strain curves for the as-HPT samples and heat treated after HPT samples of both the equiatomic and non-equiatomic compositions..... 54

Figure 19. SE micrographs showing the fracture surfaces topography of (a) the as-HPT equiatomic composition, (b) the as-HPT non-equiatomic composition, (c) the heat treated after HPT equiatomic composition, and (d) the heat treated after HPT non-equiatomic composition. 56

Figure 20. (a) XRD pattern of the as-homogenized $Co_{26}Cu_{10}Fe_{27}Mn_{10}Ni_{27}$ at.% HEA indexed to a single FCC phase (b) SEM BSE micrograph of the as-homogenized microstructure. 65

Figure 21. TEM analysis of the as-HPT microstructure including (a) automated crystal orientation mapping (ACOM) texture map, (b) ACOM phase map indexing the entire microstructure to the FCC matrix phase, (c) elliptical fit grain size distribution, and (d) STEM EDS compositional map. 66

Figure 22. (a) CALPHAD step diagram of the designed $Co_{26}Cu_{10}Fe_{27}Mn_{10}Ni_{27}$ at.% composition mapping the equilibrium phases and their relative amount as a function of temperature and (b) differential scanning calorimetry curves for the coarse grain as-homogenized sample and the nanostructured as-HPT sample. 67

Figure 23. (a) XRD patterns of the as-HPT, HPT and heat treated at 600 °C for 30 min, and HPT and heat treated at 1000 °C for 30 min; (b) BSE SEM micrograph of the HPT and heat treated at 600 °C for 30 min sample; and (c) BSE SEM micrograph of the HPT and heat treated at 1000 °C for 30 min sample. 69

Figure 24. TEM analysis of the HPT and heat treated at 600 °C for 30 min microstructure including (a) ACOM texture map, (b) ACOM phase map indexing the FCC matrix phase and B2 precipitates, (c) elliptical fit grain size distribution of the matrix FCC phase, and (d) elliptical fit grain size distribution of the precipitate B2 phase. 71

Figure 25. (a) STEM EDS compositional map the HPT and heat treated at 600 °C for 30 min microstructure, and a comparison of phase composition experimentally measured from STEM EDS of the HPT and heat treated at 600 °C for 30 min sample to the predicted composition from equilibrium CALPHAD calculations for the alloy at 600 °C for (b) the matrix FCC phase, and (c) the B2 phase. 72

Figure 26. (a) Engineering stress-strain curves representative of the as-HPT sample, the HPT and heat treated at 600 °C for 30 min sample, and the HPT and heat treated at 1000 °C for 30 min sample; (b) fracture surface of the as-HPT sample exhibiting regions of ductile cup and cone topology and regions of cleaved fracture; (c) fracture surface of the HPT and heat treated at 600 °C for 30 min sample exhibiting finer cup and cone topology; (d) fracture surface of the HPT and heat treated at 1000 °C for 30 min sample exhibiting coarse uniform cup and cone topology. ... 73

Figure 27. Thermodynamic calculations by the CALPHAD method including (a) an equilibrium isopleth diagram mapping stable phases at a range of temperatures as a function of the addition of Al to the equiatomic MoNbTiZr composition and equilibrium step diagrams plotting the

amount of stable phases as a function of temperature for the three compositions studied: (b) equiatomic MoNbTiZr, (c) $Al_4(MoNbTiZr)_{96}$ at.%, and (d) $Al_8(MoNbTiZr)_{92}$ at.%. 86

Figure 28. (a) Equilibrium isopleth diagram mapping stable phases at a range of temperatures as a function of the addition of Al to the experimentally determined MoNbTiZr non-equiatomic composition and equilibrium step diagrams plotting the amount of stable phases as a function of temperature for the three compositions formed in the first batch: (b) with no Al, (c) with 4.3 at.% Al, and (d) with 9.8 at.% Al. 89

Figure 29. Microstructural analysis of the alloy with no Al from the first batch (a) XRD patterns for the as-cast state and after heat treatment at 1300 °C for 10 hours, (b) SEM EDS mapping of the as-cast state, and (c) SEM EDS mapping of the heat treated state. 91

Figure 30. Microstructural analysis of the alloy with 4.3 at.% Al from the first batch (a) XRD patterns for the as-cast state and after heat treatment at 1500 °C for 10 hours, (b) SEM EDS mapping of the as-cast state, and (c) SEM EDS mapping of the heat treated state. 93

Figure 31. Microstructural analysis of the alloy with 9.8 at.% Al from the first batch (a) XRD patterns for the as-cast state and after heat treatment at 1500 °C for 10 hours, (b) SEM EDS mapping of the as-cast state, and (c) SEM EDS mapping of the heat treated state. 95

Figure 32. (a) X-ray diffraction patterns of the as-cast samples with increasing Al content showing increasingly broad peaks corresponding to the convolution of two BCC patterns and SEM EDS mapping of (b) MoNbTiZr sample in the as-cast state exhibiting slight chemical segregation in the solidification structure and (c) $Al_8(MoNbTiZr)_{92}$ at% sample in the as-cast state exhibiting significant chemical segregation in the solidification structure. 96

Figure 33. (a) X-ray diffraction patterns of the homogenized samples with increasing Al content showing a single relatively narrow BCC pattern for each sample and (b) SEM EDS mapping of Al4(MoNbTiZr)96 at% sample after homogenization exhibiting equiaxed grains and uniform chemistry. 98

Figure 34. (a) Representative SEM micrograph of the <110> oriented single crystal micropillar prior to testing, (b) compressive stress-strain curves for each alloy with intentional offset for visibility, and (c) micrographs of the postmortem micropillars corresponding to the stress-strain curves in (b) demonstrating clear formation of slip traces at 45° to the loading direction. 101

LIST OF TABLES

Table 1. Values of mixing enthalpy ΔHmix [kJ/mol] calculated by Miedema's model for atomic pairs between all constituent elements and the atomic radius of each constituent element in the alloy system. 20

Table 2. Yield strength, ultimate tensile strength, strain at failure, and percent area reduction for all four samples tensile tested. 55

Table 3. Mechanical properties of the as-HPT sample, the HPT and heat treated at 600 °C for 30 min sample, and the HPT and heat treated at 1000 °C for 30 min sample measured from the engineering stress-strain curves in Figure 26..... 75

Table 4. Values of mixing enthalpy ΔHmix [kJ/mol] calculated by Miedema's model for atomic pairs between all constituent elements in the AlMoNbTiZr RHEA system and the atomic radius of each element. 84

Table 5. Detailed compositional analysis of the first batch of candidate alloys using DCPES... 87

Table 6. Semi-quantitative compositional analysis using SEM-EDS for the second batch of RHEAs. 99

ACKNOWLEDGEMENTS

I must begin by acknowledging my truly exceptional advisor, Dr. Enrique J. Lavernia. My perseverance through this program and success is owed to his invaluable support, guidance, and expertise. Over the past five years, Enrique has provided me with so many amazing opportunities and always encouraged me to pursue my interests while I grew as a material scientist. Working with Enrique has instilled in me numerous habits for success and a meaningful life. To name a few, he taught me to always keep an open mind at every step of the process, entrust responsibility in others to forge strong and fruitful relationships, and to always keep an eye on the big picture: to see the forest from the trees. Due to unfortunate circumstances, our contact has been limited during the conclusion of my thesis research. But in this time, I have had the opportunity to reflect on current challenges and ask myself: *What would Enrique do*? Each time I can recall a meeting or email in which Enrique proposed effective solutions with respect for all parties involved. The grace with which Enrique faces hardships is a true sign of his character. I am proud to be his Ph.D. student and eagerly await what the future may hold.

My deepest gratitude goes to my committee members Dr. Timothy J. Rupert, Dr. Julie M. Schoenung, and Dr. Daniel R. Mumm. Tim has always been a strong voice during my time at UCI, from courses to my preliminary exam, it has been a pleasure to learn from him and collaborate with his research group. During the preparation of this dissertation, Tim volunteered to step in as an advisor for me and his support has definitely helped in progressing through this process and enhanced the quality of this dissertation. I am incredibly fortunate that Julie has remained a constant through my research career. I started as an undergraduate student researcher in her research group at UC Davis, knowing little of the innerworkings of graduate research. My time in her group was the most important preparation for my graduate experience. I am grateful for her

move to UCI, which has allowed her to remain a valuable mentor and collaborator. Dan was kind enough to allow me to spend my first quarter at UCI conducting research with his group. While I entered with an understanding of the importance of fundamental science in research, I quickly gained an appreciation for the applications side with Dan's expertise and various projects. I am glad he has remained a mentor through course instruction and acting as a committee member.

I would like to acknowledge additional mentors that have been very influential in my academic career both past and present. Through middle school and high school, I attended tutoring session for various subjects at Tutoriale in Castro Valley, CA, which was ran by Dr. Charles Conrad. Dr. Conrad not only tutored me in math and chemistry but provided me with my first job as an office assistant at the tutoring center. Dr. Conrad and the other tutors at the center were very key in developing my understanding of higher education and set me down the road I am still on today; I thank them dearly for that. Prior to my time at UC Davis, I spent several years at Las Positas Community College (LPC) in Livermore, CA. When I began at LPC I was told I should pursue engineering, due to my interest and capacity for math and science. At that time, I could vaguely differentiate between the role of a civil engineer from a mechanical engineer and was unsure of what field I wanted to pursue. Keith Level, the sole engineering faculty at LPC, was instrumental in developing my awareness of the various fields of engineering and my eventual selection of materials science. I am appreciative of Keith, not because he advocated for me to select material science, but because he did an exceptional job at presenting the nuances of each field of engineering equally, through instruction, guest lectures, as well as industry tours. This really instilled confidence that this choice was my own and built an authentic passion in me for the field of materials science that I hold to this day. I continue to find exceptional people entering my life who I have much to learn from. I would like to acknowledge Diran Apelian who has recently

become a significant influence in my professional development, and I am looking forward to all that I may learn from him.

I will always be glad for my decision to attend UCI for my Ph.D. because it allowed me to work with such an extraordinary materials science and engineering department. My time at UCI coincided the transition from the joint department of chemical engineering and materials science to two individual departments within the school of engineering. This has allowed me to interact with a variety of people at UCI that I have enjoyed working with. Although she no longer works with the department of materials science, I want to acknowledge Liz Randall for always being a kind and friendly face when visiting the department office and helping with so many little details from shipping samples internationally to filing paperwork. Steve Weinstock was one of the first staff of the department that welcomed me to UCI, a memorable sushi dinner with Darryl Mack, and became an essential part of "getting stuff done" by always being able to put me in touch with the right people during my time at UCI. It has been a pleasure to work with this department and I look forward to its continued growth and success.

By far, the most impressive skill Julie and Enrique possess is their ability to assemble and manage a spectacularly cohesive, productive, and diverse research group. Due to my extended history with this group I have had the pleasure of working with several generations of the group. While the students and postdoctoral scholars inevitably progress to other stages, several *constants* remain and work to maintain the ethos of the group.

Yizhang Zhou has been incredibly helpful throughout my thesis research and I have learned the details of everything from technical reports to project managers to publishing and grant writing. His synergy with Enrique is unmatched and ability as a team player is a trait I look up to. Another *constant* that I must acknowledge is Baolong Zhang, a scientist whose passion for research knows

no bounds. I have enjoyed every minute of working with Baolong, particularly when brainstorming approaches to his creative ideas for experiments.

At the core of the group stands Darryl Mack who has a unique ability to get anything done. As lab manager, Darryl has facilitated the experiments of countless students, me included, and established productive, sanitary, and safe laboratories. I shadowed Darryl as an undergraduate in UC Davis where I learned much about applying a healthy dose of common sense to technical problems and worked to hone my mechanical intuitions as he has. During the transition of the research laboratories from UC Davis to UCI, I learned one of Darryl's best mantras: *Do it right or do it twice*. Darryl designs spaces and experiments with class and a vision of the big picture that is shared by few and I am incredibly lucky to be exposed to his approach. He takes a level of pride in his work that translates to a highly presentable research space that is rarely seen in academic settings and I have developed the same pride in my work that I will take with me for the rest of my life. I have to acknowledge not only Darryl but the entire Mack family for acting as my adopted Southern California family; your support has been a constant motivation during my time at UCI.

As mentioned previously, I have participated in several generations of this research group through my academic career. I must acknowledge the previous generation of students and postdoctoral scholars, of which I was an undergraduate researcher: Matthew Dussing, Dr. Hanry Yang, Dr. Josh Yee, Dr. Chen Dai, Dr. Kaka Ma, Dr. Lilia Kurmanaeva, Dr. Daolong Zhang, and Dr. Tao Hu. In particular I want to thank Dr. Brandon Saller for initially bringing me into the group to work with him on his thesis research. Not only did these group members mentor me but I watched and learned from their interactions to see how a group successfully collaborates and encourages each other. I like to think I promoted a lot of those behaviors in the generation of students I worked with during my thesis research, but the reality is that working with them was

effortless. I would like to acknowledge Dr. Umberto Scipioni Bertoli, Dr. James Haley, Dr. Xin Wang, Dr. Thale Smith, Katherine Wellmon-Terrassa, Stoney Middleton, and Parnian Kiani for all their support and comradery through the years; I couldn't have wished for a better group to spend my time in lab with. Dr. Zhiqiang Fu, in particular, for bringing me into the fold of high entropy alloy research and mentoring me through the early years of my thesis research. As I finish my time with the group a new generation of students and postdoctoral scholars have come, and I look forward to following their success as they progress. Best of luck to Katie Acord, Kehang Yu, Arturo Meza, Sasha Vyatskikh, Dr. Alex Dupuy, Sen Jiang, Justin Cortez, Salma El-Azab. And while our time together was brief, I want to thank Dr. Cheng Zhang for all of his guidance with the refractory alloy work of this dissertation; I have enjoyed working with him and I am always impressed by his work ethic.

During my time at UCI a had the opportunity to mentor many undergraduate students through individual research courses to the UCI bladesmithing project. Calvin Belcher has been an ideal student and I am very grateful for the opportunity to mentor him and I am proud to see him progress from an undergraduate student to a Ph.D. student.

One of the aspects of my thesis research that I have enjoyed the most is collaboration. I have had the special opportunity to work with so many intelligent and capable researchers around the world, and without them I would not have been able to conduct the systematic and in-depth studies that are contained in this dissertation. I must acknowledge the entire team at Karlsruhe Institute of Technology (KIT), particularly Dr. Horst Hahn for his leadership, mentorship, and kind hospitality when I visited KIT. I thank Dr. Julia Ivanisenko for her expertise in the high pressure torsion process; her input is always impactful for our research. Finally, from KIT Lakshmi Mantha who is an exceptional microscopist and scientist. She and I have worked closely over the entire

five years of my thesis research and I have enjoyed all of it. I wish Lakshmi the best of luck in the conclusion of her own Ph.D. research and look forward to future collaborations. I would also like to acknowledge Dr. Nick Derimow and Dr. Reza Abbaschian of UCR for inviting me to collaborate with them on several projects. I learned a great deal about solidification mechanisms from Nick's unique liquid phase separating HEAs and I am glad I could supplement your excellent experimental work with thermodynamic modeling.

I gratefully acknowledge support from the US Army Research Office (W911NF-16-1-0269) and the Alexander von Humboldt Research Award for Senior Researchers as well as the BIAM-UCI Research Center (research agreement #210263) on various studies within this dissertation. I would also like to thank the staff of the UCI IMRI and LEXI facilities for their management and instruction for key characterization tools that I used throughout my thesis research. Also, I thank Jörg Meyer the official scientific glassblower at UCI for his assistance in forming fuse quartz ampules that were essential to all of the heat treatments reported in this dissertation.

I would like to end with my family and friends that stood by me through this entire process. I will never be able to thank my parents enough for the love and support they have given me my entire life. I really cannot put into words every single thing they have contributed and sacrificed to enable me to stand where I am today. My mother Dion has always been there for me to listen to my troubles and celebrate my accomplishments. She has worked incredibly hard in her life and career as a registered nurse and I am incredibly proud of her values, patience, and commitment. My father David is an adept motorcycle mechanic and machinist who laid the groundwork early on for my success in engineering by teaching me one of the most important skills an engineer can have: *how to turn a wrench*. Even more, I think his understanding of engine theory and ability to

describe the inner workings of two stroke engines or carburetor without graphical aid really helped to spark my imagination and trained me to mentally visualize systems, which has become a crucial aspect of my research in studying the evolution of microstructures in materials. He also gave me an eclectic taste in music, which has come in handy during long hours in lab or in front of a computer screen. I want to thank my big brother Scott for doing all the things a big brother does. Growing up with Scott led me to mature a little faster and this has really prepared me for life. I think I have been able to better assess important choices at each stage of my life because of him. The most inspiring person I have looked up to in my life is my grandfather Donald Jensen. His command of so many fields and the experiences in life is always something I am amazed of. He has told me countless stories and helped me to realize the importance of history. This allowed me to develop an important perspective on my life that places me humbly among the events and characters of the world. I have applied this context to my study of the field of materials science by looking back to understand the people and events that developed the foundation and paved the way for my research to be possible. I would also like to acknowledge my grandmother Edith Parrott who has always been lovingly supportive in my life. I am particularly grateful of our numerous trips to museums and art galleries, where I think she cultivated my appreciation of aesthetic and design, which has proven essential to developing everything from material compositions to experimental approaches throughout my thesis research.

I owe my sanity during the conclusion of my thesis research to my amazing girlfriend. She has been so supportive and patient with me throughout this process. I look forward to what the future holds.

To my friends, no matter what the distance all of you have been powerful motivators and valuable distractions when research wore me thin. To the boys, Justin Powell, Daniel Blacher, and

David Duncan, for their continued friendship since grade school. I would like to acknowledge Arick Jones, a close friend and previous roommate during my time at UC Davis. Arick is a like-minded engineer that is always ready for any conversation from tasting notes of a new beer to technical materials talk. Also, I must acknowledge Garin Anderson for his commitment to clearing his schedule and finding a great concert to attend with me every time I returned to the bay area no matter how short the trip. Although they have been mentioned previously, I must reiterate how much I appreciate the friendships of my past lab mates Umberto Bertoli Scipioni and Stoney Middleton. Umberto is one of the few people I have ever met whose brain seems to really tick the same as mine. Stoney and I mix like oil and vinegar in the best possible way. Last but not least my entire cohort that I started at UCI with. I could not have asked for a better group to progress through this program with. I am proud of all that have persevered and the community we made together.

CURRICULUM VITAE
Benjamin Erich MacDonald

EDUCATION

Ph.D. Materials Science and Engineering *September 2020*
University of California, **Irvine**

M.S. Materials Science and Engineering *2017*
University of California, **Irvine**

B.S. Materials Science and Engineering *2015*
University of California, **Davis**

EXPERIENCE

Technical

QUESTEK INNOVATIONS LLC
Materials Design Engineer Intern *01/2020-02/2020*

- Supported internal and client programs to develop new high-performance materials through integrated computational materials engineering (ICME) techniques
- Responsibilities included materials characterization, CALPHAD based materials modeling, reporting to clients through documents and presentations, and proposal writing

KARLSRUHE INSTITUTE OF TECHNOLOGY
Visiting Scholar, Institute of Nanotechnology *07/2018*

- Learned advance TEM techniques: in situ heating and precession electron diffraction
- Successfully processed FCC based high entropy alloys via severe plastic deformation to investigate the role of grain refinement on thermal stability of the principal phase

UNIVERSITY OF CALIFORNIA, IRVINE
Graduate Researcher, Laboratory of Dr. Enrique J. Lavernia *01/2016-Present*

- Collaborated with an international team of researchers to establish design methodology for high entropy alloys for structural applications
- Managed multiple projects in high entropy alloy design, focusing on CALPHAD based approaches to screening candidate compositions, thermal stability of solid solution and intermetallic phases in complex compositions, and characterization of nanostructured alloys
- Regularly contributed to the technical content of various grant applications
- Demonstrated practical skills and leadership by acting as the ‘super-user’ of laboratory equipment including the mechanical testing facilities, Wire-EDM, and differential scanning calorimeter; managing daily operation, composing standard operating procedures, training new users, troubleshooting, and regular maintenance

UNIVERSITY OF CALIFORNIA, DAVIS

Undergraduate Researcher, Laboratory of Dr. Julie M. Schoenung *04/2014-07/2015*

- Investigated the thermal stability of intermetallic phases and their individual contributions to the mechanical behavior of an Al-Fe binary alloy prepared via powder metallurgy
- Engineered and integrated a material recovery apparatus into the material processing method of cryogenic ball milling to enable the processing of high value alloys
- Operated and serviced a spray atomization system to prepare powders of various alloys to be used as feedstock material for additive manufacturing

Mentoring

Graduate Student Advisor, TMS Bladesmith Team, UC Irvine *06/2018-05/2019*

- Actively supervised all tasks to assure timely submission of the forged W-2 tool steel blade with a differential heat treatment to be showcased at the 2019 TMS Bladesmith Competition
- Conceived and presented a lecture series to connect bladesmith tradition to material science fundamentals for the students

Mentor, Individual Research with Dr. Enrique J. Lavernia *03/2017-05/2019*

- Mentored undergraduate Calvin H. Belcher in his independent project focused on the development of a small-scale induction melting system for rapid alloy synthesis
- Taught proper design of experiment (DoE) methodology and strategies for outlining technical reports and presentations to effectively convey research to a diverse audience

Teaching Assistant, Individual Research with Dr. Farghalli Mohamed *01/2018-03/2018*
01/2017-03/2017

- Supervised undergraduates in the retrofitting of a mechanical testing apparatus designed to study creep deformation in metal alloys

Peer Tutor, Dept. of Chem. Engineering and Materials Science, UC Davis *10/2014-12/2014*

- Tutored upper-division materials science thermodynamics course in collaboration with the professor and teaching assistant

Leadership

Vice President of the UCI CheMS Graduate Student Association (GSA) *09/2017-06/ 2018*

- Organized departmental events in collaboration with the GSA president and faculty including prospective student visitation, first year orientation, and student body panel discussions

Ambassador to the Faculty of the UCI CheMS GSA *09/2016-09/2017*

- Attended departmental faculty meetings on behalf of the GSA to act as a conduit for the voice of the student body

Vice-Chair of the Material Advantage Student Chapter at UC Davis *05/2014-06/2015*

- Coordinated outreach activities oriented towards prospective/current students as well as the general public to promote material science

PUBLICATIONS

Journal Papers

J1. L.S. Mantha, B.E. MacDonald, J. Ivanisenko, H. Hahn, E.J. Lavernia, S. Katnagallu, C. Kübel, "Grain boundary segregation induced precipitation in a MnFeCoNiCu complex concentrated alloy", Full-Length Article, In Preparation.

J2. A.L. Vyatskikh, B.E. MacDonald, A.D. Dupuy, H. Hahn, E.J. Lavernia, J.M. Schoenung, "High entropy silicides: CALPHAD aided prediction and thin film fabrication", Letter, In Preparation.

J3. B.E. MacDonald, X. Wang, C. Zhang, F. Guo, Y. Kang, X. Xie, Y. Zhou, J.M. Schoenung, E.J. Lavernia, "CALPHAD aided prediction of an $Al_xMoNbTiZr$ refractory complex concentrated alloy system", Letter, In Preparation.

J4. B.E. MacDonald, L.S. Mantha, Z. Fu, J. Ivanisenko, W. Chen, Y. Zhou, C. Kübel, H. Hahn, E.J. Lavernia, "Effect of phase decomposition on mechanical behavior in a nanocrystalline non-equiatomic CoCuFeMnNi high entropy alloy", Full-Length Article, In Preparation.

J5. C. Zhang, C. Zhu, P. Cao, X. Wang, F. Ye, K. Kaufmann, L. Casalena, B.E. MacDonald, X. Pan, K.S. Vecchio, E.J. Lavernia, "Aged metastable high-entropy alloys with heterogeneous lamella structure for superior strength-ductility synergy", *Acta Materialia*, Accepted for publication, 2020.

J6. C. Zhang, B.E. MacDonald, F. Guo, H. Wang, C. Zhu, X. Liu, Y. Kang, X. Xie, Y. Zhou, K.S. Vecchio, E.J. Lavernia, "Cold-workable refractory complex concentrated alloys with tunable microstructure and good room-temperature tensile behavior", *Scripta Materialia*, Vol. 188, pp. 16-20, 2020.

J7. N. Derimow, B.E. MacDonald, E.J. Lavernia, R. Abbaschian, "Duplex phase hexagonal-cubic multi-principal element alloys with high hardness", *Materials Today Communications*, Vol. 21, pp. 100658, 2019.

J8. B.E. MacDonald, Z. Fu, Z. Li, W. Chen, Y. Zhou, D. Rabbe, H. Hahn, E.J. Lavernia, "Influence of phase decomposition on mechanical behavior of an equiatomic CoCuFeMnNi high entropy alloy", *Acta Materialia*, Vol. 181, pp. 25-35, 2019.

J9. Z. Fu, A. Hoffman, B.E. MacDonald, Z. Jiang, W. Chen, M. Arivu, H. Wen, E.J. Lavernia, "Atom probe tomography study of an Fe25Ni25Co25Ti15Al10 high-entropy alloy fabricated by powder metallurgy", *Acta Materialia*, Vol. 179, pp. 372-382, 2019.

J10. A. Munitz, I. Edry, E. Brosch, N. Derimow, B.E. MacDonald, E.J. Lavernia, R. Abbaschian, "Liquid phase separation in AlCrFeNiMo0. 3 high-entropy alloy", *Intermetallics*, Vol. 112, pp. 106517, 2019.

J11. Z. Fu, B.E. MacDonald, A.D. Dupuy, X. Wang, T.C. Monson, R.E Delaney, C.J. Pearce, K. Hu, Z. Jiang, Y. Zhou, J.M. Schoenung, E.J. Lavernia, "Exceptional combination of soft magnetic and mechanical properties in a heterostructured high-entropy composite", *Applied Materials Today*, Vol. 15, pp. 590-598, 2019.

J12. U. Scipioni Bertoli, B.E. MacDonald, J.M. Schoenung, "Stability of cellular microstructure in laser powder bed fusion of 316L stainless steel", *Materials Science and Engineering A*, Vol. 739, pp. 109-117, 2019.

J13. N. Derimow, L.J. Santodonato, B.E. MacDonald, B. Le, E.J. Lavernia, R. Abbaschian, "In-Situ Imaging of Molten High-Entropy Alloys Using Cold Neutrons", *Journal of Imaging*, Vol. 5, Issue 2, pp. 29, 2019.

J14. Z. Fu, J.L. Wardini, B.E. MacDonald, H. Wen, W. Xiong, D. Zhang, Y. Zhou, T.J. Rupert, W. Chen, E.J. Lavernia, "A high-entropy alloy with hierarchical nanoprecipitates and ultrahigh strength", *Science Advances*, Vol. 4, Issue 10, pp: eaat8712, 2018.

J15. Z. Fu, B.E. MacDonald, D. Zhang, B. Wu, W. Chen, J. Ivanisenko, H. Hahn, E.J. Lavernia, "Fcc nanostructured TiFeCoNi alloy with multi-scale grains and enhanced plasticity", *Scripta Materialia*, Vol. 143, pp. 108-112, 2018.

J16. Z. Fu, B.E. MacDonald, Z. Li, Z. Jiang, W. Chen, Y.Zhou, E.J. Lavernia, "Engineering heterostructured grains to enhance strength in a single-phase high-entropy alloy with maintained ductility", *Materials Research Letters*, Vol. 6, Issue 11, pp. 634-640, 2018.

J17. K.L. Terrassa, J.C. Haley, B.E. MacDonald, J.M. Schoenung, "Reuse of powder feedstock for directed energy deposition", *Powder Technology*, Vol. 338, pp. 819-829, 2018.

J18. Z. Fu, B.E. MacDonald, T. C. Monson, B. Zheng, W. Chen, E.J. Lavernia, "Influence of heat treatment on microstructure, mechanical behavior, and soft magnetic properties in an fcc-based Fe29Co28Ni29Cu7Ti7 high-entropy alloy", *Journal of Materials Research*, Vol. 33, Issue 15, pp. 2214-2222, 2018.

J19. Z. Fu, W. Chen, Z. Jiang, B.E. MacDonald, Y. Lin, F. Chen, L. Shang, E.J. Lavernia, "Influence of Cr removal on the microstructure and mechanical behavior of a high-entropy Al0.8Ti0.2CoNiFeCr alloy fabricated by powder metallurgy", *Powder Metallurgy*, Vol. 61, Issue 2, pp.106-114, 2018.

J20. B.E. MacDonald, Z. Fu, B. Zheng, W. Chen, Y. Lin, F. Chen, L. Zhang, J. Ivanisenko, Y. Zhou, H. Hahn, E.J. Lavernia, "Recent progress in high entropy alloy research", *JOM*, Vol. 69, Issue 10, pp. 2024-2031, 2017.

Papers in Conference Proceedings

C1. B.E. MacDonald, Z. Fu, J. Ivanisenko, H. Hahn, E.J. Lavernia, "Influence of constituent element concentration on the mechanical behavior of solid solution CoCuFeMnNi high entropy alloys", *Proceedings of Processing and Fabrication of Advance Materials XXVII*, Sweden, 2019

Presentations

P1. [invited] "Current Perspectives in High Entropy Alloys", B.E. MacDonald, webinar, Institute of Nanotechnology, Karlsruhe Institute of Technology, Karlsruhe, Germany, 2020.

P2. [invited] "Current Perspectives in High Entropy Alloys", B.E. MacDonald, webinar, Department of Materials Science and Engineering, University of California, Irvine, Irvine, CA, USA, 2020.

P3. "CALPHAD Aided Design of MoNbTiZr-based High Entropy Alloys", B.E. MacDonald et al., poster presentation at the 149th TMS Annual Meeting & Exhibition, San Diego, CA, USA, 2020.

P4. [invited] "Achieving ultrahigh strength in a high entropy alloy via high density of hierarchical nanoprecipitates", B.E. MacDonald et al., presentation at the 148th TMS Annual Meeting & Exhibition, San Antonio, TX, USA, 2019.
P5. [invited] "CALPHAD Screening and Mechanical Behavior in the AlMoNbTiZr Alloy System", B.E. MacDonald et al., presentation at the 148th TMS Annual Meeting & Exhibition, San Antonio, TX, USA, 2019.
P6. "Mechanical Behavior and Phase Evolution in the MnFeCoNiCu high Entropy Alloy System", B.E. MacDonald et al., poster presentation at the 148th TMS Annual Meeting & Exhibition, San Antonio, TX, USA, 2019.
P7. "Mechanical Behavior and Thermal Stability of a Dual-Phase Complex High Entropy Alloy", B.E. MacDonald et al., presentation at the 147th TMS Annual Meeting & Exhibition, Phoenix, AZ, 2018.
P8. [invited] "Exploring mechanical behavior and thermal stability in a complex high entropy alloy system", B.E. MacDonald et al., presentation at the 1st International Symposium on Advanced Structural Materials, Chongqing University, Chongqing, China, 2017.
P9. "Exploring the effects of grain refinement in non-equiatomic high entropy alloys", B.E. MacDonald et al., poster presentation at the 146th TMS Annual Meeting & Exhibition, San Diego, CA, USA, 2017.

PROFESSIONAL SERVICE

Reviewer for the following journals:	**Dates**
Materials Science and Engineering A	2016-Current
Journal of Materials and Design	2018-Current
Journal of Alloys and Compounds	2019-Current
Philosophical Magazine	2019-Current
Materials Research Letters	2019-Current

Memberships in Professional Organizations	**Dates**
The Minerals, Metals, and Materials Society (TMS)	2014-Current
ASM International	2014-Current
Association for Iron & Steel Technology (AIST)	2014-Current
The American Ceramics Society (ACerS)	2014-Current

Awards and Recognition Received

Award	**Dates**
Federal Work Study Award	August 29, 2016
Outstanding Senior Award, MSE Department, UC Davis	May 27, 2015
Phillips 66 Scholar Award	May 27, 2014
Dean's List, College of Engineering, UC Davis	Winter quarter 2014, Fall quarter 2013

Recognition	**Dates**
Nominated by the School of Engineering at UC Irvine for the Chancellor's Club Fund for Excellence Fellowship	October 18, 2019

ABSTRACT OF THE DISSERTATION

Design and phase stability of high entropy alloys for structural applications

by

Benjamin Erich MacDonald

Doctor of Philosophy in Materials Science and Engineering

University of California, Irvine, 2020

Professor Timothy J. Rupert, Chair

As the field of high entropy alloy research has matured, investigation of phase stability in these alloys, particularly those with complex compositions, has become paramount if they are to be considered for structural engineering applications. The objective of this dissertation research is to study phase stability in targeted high entropy alloy (HEA) compositions as it pertains to the mechanical properties and processability of the material. While the studies presented here implement similar methodology of comparing experimental analysis of different HEAs to computational modeling of the alloys by the CALculated PHAse Diagram (CALPHAD) approach, each study aims to elucidate a unique aspect of phase stability and structural properties in HEAs. The first study describes the phase decomposition in a CoCuFeMnNi HEA and how the reported secondary phases influence mechanical behavior to establish these behaviors for the typical starting composition for an HEA system: equiatomic. Thermomechanical processing, followed by systematic annealing treatments, revealed the formation of two distinct secondary phases within the equiatomic face-centered cubic (FCC) matrix: Fe-Co rich ordered B2 precipitates that contributed precipitation hardening and Cu segregation, due to its immiscibility with the other constituents, eventually forms a Cu-rich chemically disordered FCC phase. The thermal stability and chemistry of these phases are compared to those predicted on the basis of CALPHAD analyses.

In the second study, a novel non-equiatomic composition within the CoCuFeMnNi HEA system is developed to reduce the stability of the Cu-rich FCC and determine the role of constituent concentration on the mechanical behavior of alloys in the CoCuFeMnNi system. The equiatomic and non-equiatomic compositions were processed by high pressure torsion (HPT) and the mechanical behavior of the single FCC phase alloys before and after high temperature heat treatments are compared to determine the role of Mn and Cu in solid solution strengthening for these alloys. The third study assesses the phase stability in the nanocrystalline non-equiatomic composition $Co_{26}Cu_{10}Fe_{27}Mn_{10}Ni_{27}$ at.% HEA and the implications of secondary phase formation on the mechanical behavior. After processing the material by HPT to achieve a nanocrystalline FCC matrix, thermal analyses and microstructural characterization of heat treated samples track the precipitation and dissolution behavior of Fe-Co rich B2 precipitates. The CALPHAD approach correctly predicted the composition and volume fraction of each phase after heat treatment. The presence of the B2 phase increased the stiffness and strength of the nanocrystalline HEA while causing embrittlement. The final study of the dissertation continues to focus on the phase stability but transitions to the refractory HEA system AlMoNbTiZr. The addition of Al to the equiatomic MoNbTiZr base, is predicted and validated to increase the stability of multiple BCC solid solutions. Al additions below 8 at.% enhanced the formation of a secondary BCC upon solidification while maintaining a single-phase BCC region at elevated temperatures. The hardness of the alloys increased with the increase of Al and deformation behavior in single-crystal micropillar samples are markedly different with and without Al. Together, these studies present an effective approach to assess phase stability in HEAs and design them for structural applications.

Chapter 1 : Introduction to high entropy alloy design

1.1 Overview

Since their discovery in 2004, high entropy alloys (HEAs) have generated significant interest from the materials science community due to unique phase formation as well as reports of exceptional mechanical performance in select compositions. The design of HEAs marks a distinct departure from conventional alloy design through the transition to a multi-principal element design approach. For example, while compositions of conventional Al alloys possess more than 90 at.% aluminum with minor amounts of alloying elements, HEAs are generally based on five or more elements in a near equiatomic composition. Particular compositions solidify a unique random solid solution crystalline structure, in which each of the constituent elements has a near equal probability of occupying a given lattice site of a face centered cubic (FCC), body centered cubic (BCC), or hexagonal closed pack (HCP) lattice. The initial hypothesis for the formation of these random solid solution phases was that the relatively high entropy of mixing, due to the complex composition, was stabilizing the simple phase formation observed [1]. The field of HEAs now understands that entropy alone does not dictate the phase formation in complex compositions based on the results of detailed studies on well-known HEA compositions that observed decomposition of the random solid solution phase after extended annealing heat treatments [2]. With the current understanding of HEAs, there has been a shift in research emphasis from targeting single random solid solution alloys to the development of complex HEAs with desirable multi-phase microstructures. To address the vast number of potential compositions in the expansive compositional space defined by HEAs, high throughput approaches serve to explore and screen potential HEA compositions for structural applications [3–5]. These approaches rely on the predictive thermodynamic modeling of possible compositions using the calculation of phase diagrams by the CALculated PHAse

Diagram (CALPHAD) approach [6]. Significant challenges surround the current efforts of HEA research including evaluating the reliability of current CALPHAD methods for HEAs, exploring the effect of microstructural variations, and including grain structure and dislocation density, on mechanical properties and phase stability in HEAs.

1.2 Emergence of high entropy alloys

The earliest reports of high entropy alloys (HEAs) date back to 2004 when two research groups of Cantor et al. of Oxford University and Yeh et al. of National Tsing Hua University published simultaneously on the development of crystalline multicomponent alloys [7,8]. Cantor's work originated from an undergraduate thesis in the late 1970's that was adapted into another project in 1998. Yeh, who was the first to coin the term "high entropy alloy", published several other studies in 2004 [9–12]. The basis of these works was the synthesis of metallic alloys that contained five or more constituent elements in near equiatomic concentration. Upon characterization of these alloys, far less phases are formed than expected by the Gibbs phase rule [7]. In addition, some compositions achieve a single crystalline structure where each constituent element has an equal probability of populating a given lattice site. This random solid solution (RSS) is schematically drawn in Figure 1, where elements A through E occupy an FCC atomic lattice structure. The uncommon observations from these reports sparked the interest of the materials science community. Since 2004, the field of HEA research has grown significantly with a total of approximately 650 publications in 2017 alone. The contents of these publications focus on elucidating mechanisms driving exceptional properties found in these alloys, fundamental understanding of the unique structure possessed, and developing the capability to predict HEA compositions. Many review articles [13–18] a book [19] and technical reports [20] have been published providing a comprehensive look at all the expansive research on HEAs and highlight

the wide range of potential applications both structural and functional from use as structural components at both cryogenic and elevated temperatures to use for solid state cooling. The following includes key findings in the field as they pertain to the scope of my thesis work.

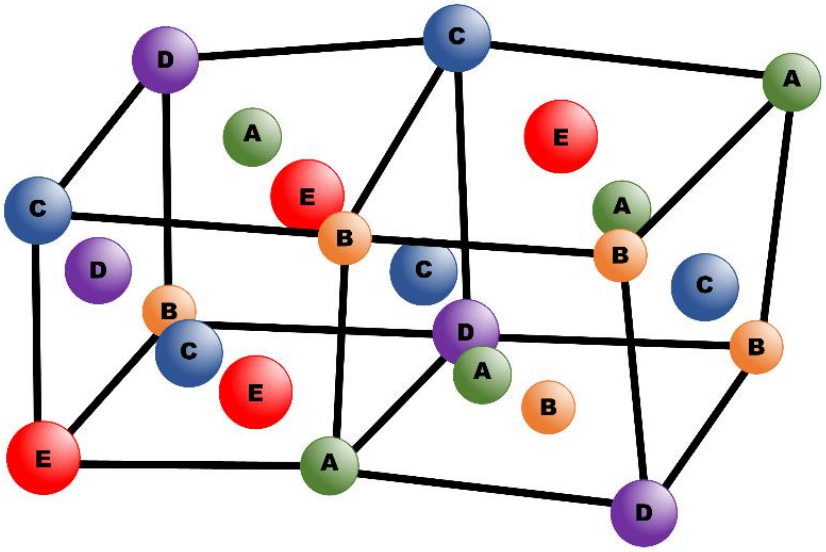

Figure 1. Schematic illustration of the random solid solution structure unique to HEAs composed of arbitrary elements A, B, C, D, and E organized on a distorted face centered cubic crystal structure reprinted from reference [17].

1.3 The four core effects

In an attempt to explain the observations of simple RSS phases in early HEA studies, Yeh proposed in 2006 the following four core effects of multi-principal element composition [1]. One, the high entropy effect explains the formation of an RSS phase by thermodynamic stabilization due to a maximization of mixing entropy. Two, severe lattice distortion inherent to the RSS has a significant effect on the mechanical and physical properties. Three, sluggish diffusion kinetics that potentially cause the nanocrystalline stability and corrosion resistance observed in HEAs. Four, the cocktail effect that treats HEAs as a composite material of elements selected for desired properties. As the field has grown and more experimental results have been published on a variety

of HEA compositions, the validity of these four core effects has been investigated. The following addresses the concepts of each effect and summarize the community's current understanding.

1.3.1 The high entropy effect

The most notable core effect, that gives the alloys their name, is the high entropy effect. Yeh et al. used the ideal case for total free energy of mixing to explain the RSS phase of HEAs. The free energy of mixing can be expressed as:

$$\Delta G_{mix} = \Delta H_{mix} - T\Delta S_{mix}$$

where the free energy ΔG_{mix} can be related to the enthalpy ΔH_{mix} and the entropy ΔS_{mix} of a state, elemental or mixed, for a system at a given temperature. From Boltzmann's equation, an approximation to ΔS_{mix}, the configuration entropy ΔS_{config} of a state, can be related to the number of constituents *n*:

$$\Delta S_{config} = -R \sum_{i=1}^{n} X_i \ln X_i$$

where R is the gas constant and X_i is the concentration of the i^{th} constituent. As the number of constituents of the system increases, the entropy of an RSS approaches a maximum that dominates over the enthalpy of formation for pure elemental phases and intermetallic phases, stabilizing the formation of an RSS.

The correlation between configuration entropy and the presence of RSS phases in HEAs has been contested by microstructural observations. In general, when considering many of the published microstructures of HEA compositions, collected by Miracle in his recent review on HEAs, most possess both intermetallic phases along with an RSS phase [16]. The multi-phase nature of many of these HEAs provides evidence that the number of constituent elements may not

be the defining quality of HEAs. Recently, Pickering et al. found the most well studied single RSS FCC HEA CrMnFeCoNi exhibited precipitation after annealing at 700 °C for up to 1000 hours [2]. This observation has reinforced the fact that it is essential to consider all components off the Gibbs free energy equation when determining what phases are stable in a given composition, regardless of the complexity of said composition.

1.3.2 Severe lattice distortion

The concept of severe lattice distortion in RSS phases is an extension of the mechanisms of traditional solid solution strengthening. In the case of conventional alloys, when solute elements are substitutionally alloyed into a lattice of the solvent element, the atomic size misfit causes strain to develop in the surrounding lattice that leads to minor distortion of the repeating structure. When there is no differentiation between solute and solvent, as is the case for most HEAs, it is expected that every lattice site will have some displacement from the perfect crystal lattice site. One of the clearest observations of this distortion to date is the diminished peak intensities of HEA X-ray Bragg diffraction patterns. Yeh et al. systematically studied the effect of increasing the number of constituent elements in the alloy system AlSiCrFeCoNiCu on the intensity of the resulting X-ray diffraction pattern [21]. Yeh et al. found that incrementally increasing the compositional complexity one element at a time from pure Cu to AlSiCrFeCoNiCu decreased the peak intensity. The increasing distortion of the lattice continually deviates from a perfect lattice, creating less Bragg scattering events to occur in a manner similar to the thermal effect.

The distortion of the lattice is undoubtedly present in RSS phases but the severity of the distortion has recently been studied by Owen et al. via total scattering measurements using neutron radiation [22]. From these measurements, Owen et al. obtained the pair distribution function of CrMnFeCoNi which is directly related to the distribution of the interatomic spacing on a local

atomic level, unlike the average values determined from Bragg diffraction. From the results, Owen et al. found the HEA does possess the most lattice strain compared to similar, but less complex, compositions within the alloy system; but these values were not exceptionally larger. This is an important observation that must be considered when analyzing HEAs, particularly when discussing mechanical behavior as to not misappropriate lattice strain to explain disproportional increases in mechanical strength.

1.3.3 Sluggish diffusion

The third effect from the RSS proposed by Yeh et al. is the decrease of diffusion kinetics in HEAs. Yeh et al. describes the atomic diffusion in HEAs as “sluggish” mainly due to the local lattice potential fluctuations caused by the different constituent elements in the RSS. Figure 2 provides a schematic plot of the lattice potential energy as a function of position along an arbitrary diffusion path in two cases, a RSS HEA and a pure element or dilute solid solution [15]. From the disorder of the RSS, the local lattice potential energy can form deep traps that inhibit diffusion. This concept is often used to qualitatively explain some of the exceptional properties of reported HEAs, including corrosion resistance and thermal stability.

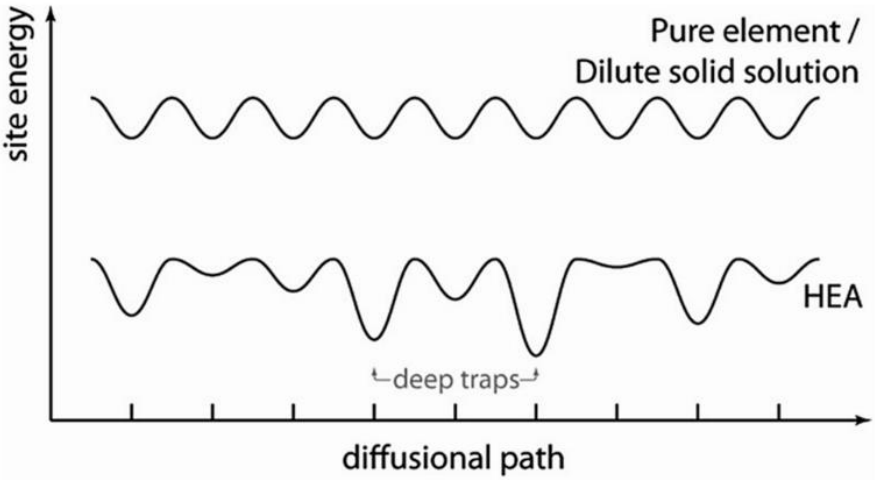

Figure 2. Schematic plot of the site energy along an arbitrary diffusional path in pure elements or dilute solid solutions as opposed to HEAs, reprinted from reference [15].

The effort to quantify this sluggish diffusion is limited to two publications that report diffusion coefficients [23,24]. Tasi et al. published the first report of diffusion rates in HEAs in which the self-diffusion coefficients of the elements in the CrMnFeCoNi system were calculated by annealing "quasi-binary diffusion couples" [23]. Tasi et al. compared the results to austenitic steels and pure metal systems and found that for every element in the HEA, the self-diffusion rate was lowest in the HEA. Vaidya et al. conducted a study on the tracer diffusion of Ni in CrFeCoNi and CrMnFeCoNi and compared the results to other FCC systems [24]. When the diffusivity of Ni is compared to the inverse homologous temperature, slower diffusion of Ni was observed for larger configurational entropy. While both studies confirm slower diffusion kinetics in HEAs, the relative decrease is not exceptionally large. It is important to point out the sensitivity of diffusivity measurements, which depend exponentially on the activation energy normalized by the melting temperature. Errors in activation energy measurements can lead to orders of magnitude difference in the resulting diffusivity. To develop a better understanding of diffusion phenomena in HEAs, carefully designed experiments on a range of alloy systems are needed.

1.3.4 Cocktail effect

The final effect put forth by Yeh et al. was the cocktail effect. The cocktail effect refers to the selection of elements for an HEA composition based specifically on the properties that the element will contribute to the resulting HEA. This concept is an extension of the design method for composites where materials are combined based on their individual properties to produce a material with a balance of these properties. In this case, HEAs are effectively a composite of elements, chosen to create an alloy that possesses desired properties. An example of this design approach is the inclusion of Al and Cr in an alloy to improve oxidation resistance at high temperature. This combinatorial approach to alloy design is not unique to HEAs and is generally used throughout conventional alloy design. Regardless of its novelty, the approach is useful for exploring more potential HEA compositions.

1.4 High entropy alloy definition

It is evident from the four core effects that as the community's understanding advances, the criteria for defining HEAs evolves. The first formal definition of HEAs by Yeh established both a compositional requirement, of five or more principal constituent elements each with an atomic percent of 5-35 at.%, along with the requirement that the configurational entropy must be greater than or equal to 1.5R [1]. This distinction based on the configurational entropy created other regimes described by Yeh as medium entropy alloys, with a configurational entropy value between R and 1.5R, and low entropy alloys, essentially traditional alloys that possess a configurational entropy value below R. As the community began to understand that high configurational entropy is not the sole determination of whether a composition would achieve an RSS phase, more strict definitions were put forth for HEAs. Specifically, only alloys containing five of more elements in near equiatomic concentrations that maintain a single RSS should be

designated as HEAs. If this definition were to be imposed, all compositions that produce microstructures with any secondary phases would need another designation. Alternative names such as multi-principal element alloys, compositionally complex alloys and complex concentrated alloys have all been proposed but renaming the field is impractical at this stage of research [15]. The well accepted definition of HEAs is a crystalline system based off four or more elements each constituting 5-35 at.%. The microstructure must contain at least one RSS phase and may include intermetallic, ordered, and/or precipitate phases. Additional alloying elements (less than 5 at.%) can be included into HEAs if the composition produces at least one RSS phase. These limitations create bounds that incorporate many HEAs to date and is expected to accommodate the growing complexity associated with engineering promising HEA systems for application.

1.5 Classification of high entropy alloys

When considering HEAs for structural applications, two distinct classes of HEAs have emerged with promising properties: 3d-transition metal HEAs and refractory HEAs. 3d-transition metal HEAs include almost exclusively 3d-transition metals within the alloy composition, with the exception of Al in certain cases, and in general stabilize an FCC RSS phase. Refractory HEAs on the other hand, possess compositions based on refractory elements, found in subgroups four to six on the periodic table, and tend to form a BCC RSS phase. These two classes of HEAs are briefly introduced with a focus on the standout mechanical properties reported for each.

1.5.1 Standout 3d-transition metal high entropy alloys

CrMnFeCoNi, the Cantor Alloy, has been studied extensively in the single FCC phase state with several noteworthy mechanical properties. Gludovatz et al. synthesized the equiatomic CrMnFeCoNi composition via arc melting followed by cold forging, a rolling process, and annealing to achieve a sheet sample with a refined equiaxed grain structure [25]. The fracture

toughness and tensile yield strength of this material is compared to the same properties of common material systems in Figure 3 [25]. While the yield strength of this material does not surpass all metals and alloys shown, the fracture toughness is exceptionally high in part due to the formation of planar glide dislocations that form cell structures, promoting strain hardening during plastic deformation. Otto et al. arc melted and cold rolled the CrMnFeCoNi alloy to examine the variation in mechanical behavior at cryogenic temperatures [26]. CrMnFeCoNi exhibited increased yield strength at cryogenic temperatures with maintained ductility caused by the addition of deformation induced nanoscale twinning that further enhanced strain hardening, preventing the onset of necking in each sample. This observation along with the exceptional fracture toughness makes CrMnFeCoNi a promising candidate for cryogenic applications but further research is needed to assess the feasibility of its implementation.

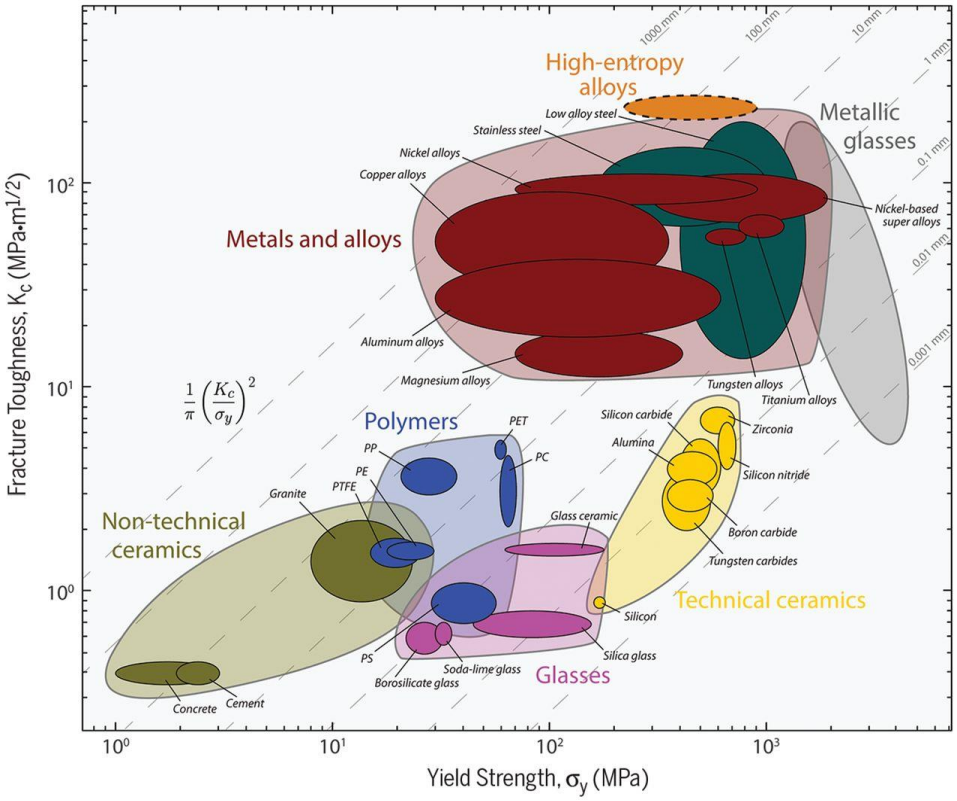

Figure 3. Ashby map presenting fracture toughness as a function of tensile yield strength including HEAs and many other material systems, reprinted from reference [25].

1.5.2 Standout refractory metal high entropy alloys

Refractory HEAs demonstrate high thermal stability and comparable mechanical properties to commercial Ni-based superalloys. Miracle et al. collected the compressive yield strength as a function of temperature for ten HEAs containing a BCC RSS and compared the results to the tensile yield strength of three commercially available nickel based superalloys as seen in Figure 4 [16]. Out of the ten HEAs, $Al_{0.4}TiZrNbHf_{0.6}Ta$, AlTiVNb, TiZrNbHfTa, VNbMoTaW, and TiVZrNb contain a single BCC RSS (note compositions in reprinted figure are ordered alphabetically). It is important to emphasize that the values for the commercial superalloys correspond to tensile data while the HEAs here correspond to compressive data, complicating the

direct comparison of the two. Still, the performance of these alloys is attractive when considering the relative simplicity of microstructural features as compared to the superalloys.

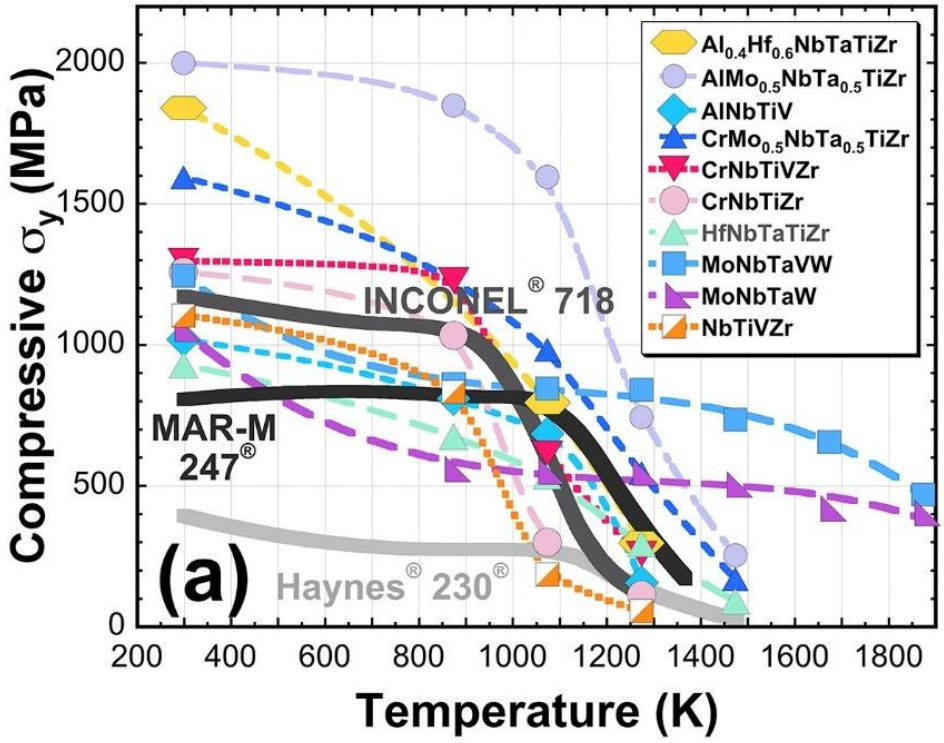

Figure 4. Compressive strength as a function of temperature for ten published HEA compositions compared with tensile strength as a function of temperature for three commercially available superalloys, reprinted from reference [16].

1.6 Modeling high entropy alloys

Possibly the most challenging aspect of researching HEAs is probing the vast compositional space available. When considering the possible number of precise compositions generated from varying principal elements, concentrations of principal elements, and concentrations of alloying elements, Miracle et al. used combinatorial equations to calculate hundreds of millions of possibilities [16]. Therefore, crucial to the research field is the development of phase prediction techniques to target candidate compositions. To address this challenge, several empirical rules and parameters were initially proposed to predict phase

formation [27]. More recently, computational modeling has been implemented to rapidly screen compositions based on their simulated microstructure. Calculated phase diagram CALPHAD modeling has emerged in recent years as an effective approach for predictively screening potential HEA systems and compositions for desirable microstructures. Most notable is the efforts by ThermoCalc, a company well known for their commercial CALPHAD software, who have developed a specialized database to be specifically used when considering HEA compositions [6].

A flow diagram of the assessment procedure of the CALPHAD approach according to Lukas et al. is presented in Figure 5. In the CALPHAD approach, available theoretical and experimental data are used to assess the parameters of a given phase's Gibbs energy model [28]. The Gibbs energy models are then implemented in computational thermodynamics functions, that depend on temperature, pressure, and composition, to determine equilibrium states. A general form for the total Gibbs energy G_m^θ, for a given phase θ, that is used in the CALPHAD approach is expressed by:

$$G_m^\theta = {}^{srf}G_m^\theta + {}^{phys}G_m^\theta - T \cdot {}^{cnf}S_m^\theta + {}^{E}G_m^\theta$$

where the total Gibbs energy is seen as the summation of the Gibbs energy for an unreacted mixture of the constituents ${}^{srf}G_m^\theta$, the contribution to the Gibbs energy due to a physical model ${}^{phys}G_m^\theta$, the negative of temperature multiplied by the configurational entropy ${}^{cnf}S_m^\theta$, and the excess Gibbs energy ${}^{E}G_m^\theta$ [28]. Each of these major terms contains parameters that are selected based on the input of experimental phase diagram data, measured thermodynamic quantities, and theoretical crystallographic information of the phase. To determine the final parameter set to be used in the computations, the CALPHAD approach goes through a detailed optimization to assure reliability of the resulting thermodynamic descriptions. The data used for parameter selection are found in

databases supplied by the software company, ThermoCalc. The databases are compiled with experimental data on lower order systems of the constituent elements considered (i.e., unary, binary and in some cases ternary) [6]. These databases are often specialized to a specific class of alloys for example Al alloys or Ni based superalloys. Within these specialized databases there are certain simplifications and omissions to the dataset of the considered constituents due to the lack of influence on calculations based in conventional composition space (single principal element approach). In order to accurately model complex compositions, as is the case for HEAs, the new database from ThermoCalc assesses all binary systems possible from the constituent elements considered as well as many key ternaries to minimize the number of simplifications. To date, this database has been updated three times and each time more elements are considered in the database, and better assessments of the binary and ternary interactions are achieved to develop a more reliable modeling approach for HEA research. Several publications have demonstrated the validity of CALPHAD computations by comparing them to experimentally formed HEAs [6,29,30]. From the results of these publications it is clear that the ThermoCalc CALPHAD approach is beneficial to the study of HEAs.

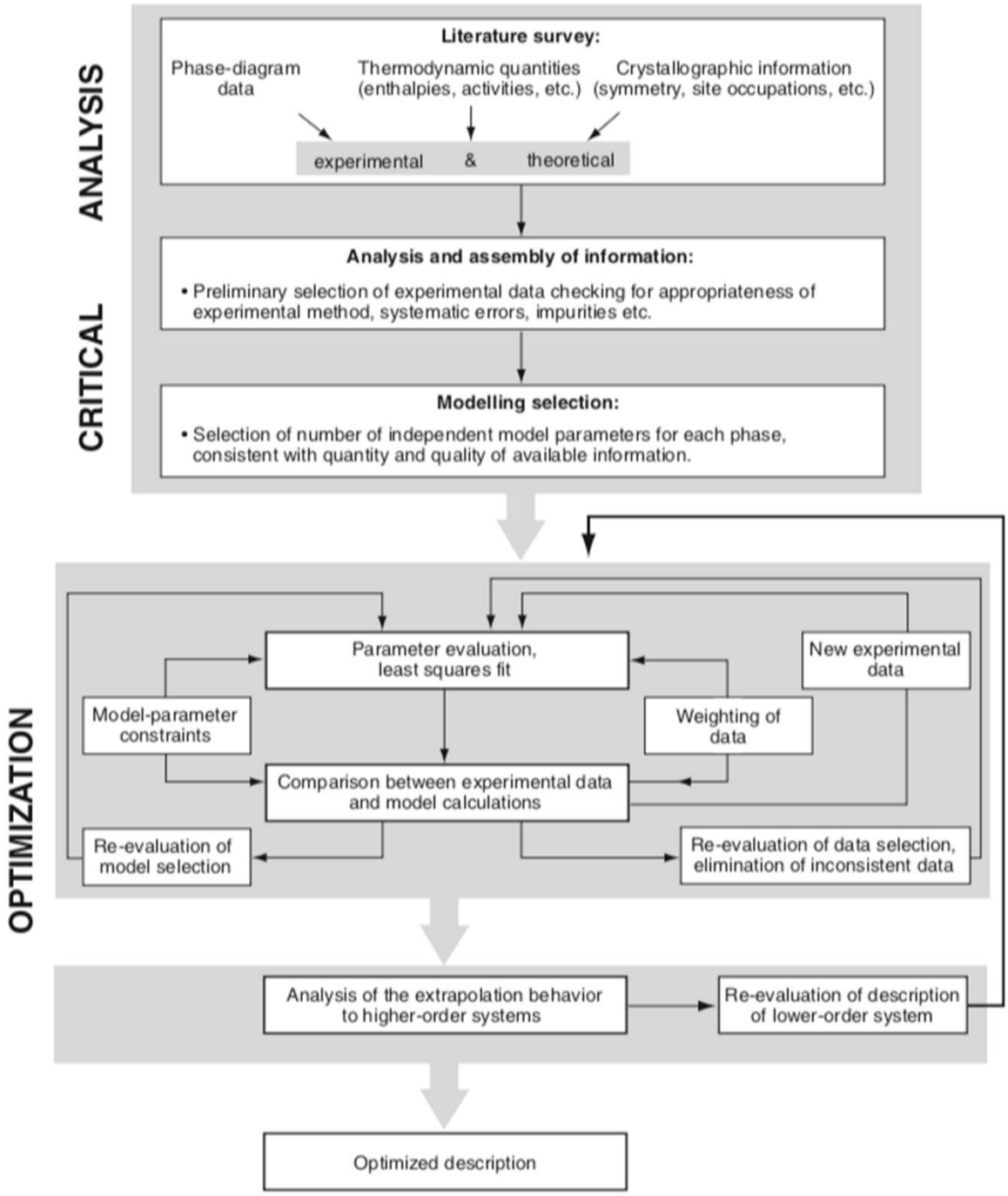

Figure 5. A schematic flow diagram of the CALPHAD assessment approach, reprinted from reference [28].

1.7 Dissertation objectives

The goal of this Ph.D. dissertation is to investigate phase formation and stability in complex HEA compositions after various metallurgical processing routes to better elucidate effective design approaches for HEA compositions with desirable structural properties and processability. To accomplish this goal, we propose the following approach:

I. Establishing a connection between properties of alloy constituents and the resulting phases that evolve within the microstructure;

II. Understanding the role of processing in changing the stability of secondary and primary phases in HEAs;

III. Correlation of experimental characterization with computational thermodynamics to validate the use of CALPHAD for the design of HEAs;

IV. Development of new HEAs with beneficial multiple phase microstructures for structural applications.

The following chapters of the dissertation present four studies conducted using the approach proposed above. First, a phase decomposition and its influence on the mechanical behavior of the equiatomic CoCuFeMnNi HEA processed by cold rolling was investigated to establish these methodologies in an FCC based equiatomic composition HEA. To explore the role of constituent concentration on the mechanical behavior of HEAs in a single FCC phase state, the second study develops a novel non-equiatomic composition within the CoCuFeMnNi HEA system with a reduced concentration of Cu and Mn to examine the influence of each in solid solution strengthening of the FCC HEA in nanocrystalline and coarse grain microstructures. After comparing the two compositions in the single FCC phase state, the phase decomposition that occurs after high pressure torsion and post deformation heat treatment as well as the resulting

mechanical behavior was probed in the non-equiatomic alloy. The final study of the dissertation shifts to a refractory based HEA system of AlMoNbTiZr while the principal factors of phase stability, mechanical behavior and the validation of CALPHAD predictions are the primary goals. The culmination of these studies demonstrates a systematic approach of synergistically coupling CALPHAD methods and experimental validations to design HEAs for structural applications.

Chapter 2 : Influence of phase decomposition on mechanical behavior of an equiatomic CoCuFeMnNi high entropy alloy

2.1 Background

Since the inception of HEAs, research has uncovered interesting fundamental phenomena, such as complex phase stability at intermediate temperatures in these alloys as well as exceptional mechanical performance in select compositions. A majority of the HEAs studied to date are composed of transition metal elements, most notably the equiatomic composition of CoCrFeMnNi coined “the Cantor alloy” after the author of the first report on this alloy [7]. This alloy possesses the signature feature of HEAs, a single disordered solid solution face centered cubic (FCC) phase composed of all five constituents, and exhibits exceptional fracture toughness at room temperature due to the formation of planar glide dislocations that form cell structures, thus promoting strain hardening [25]. Additionally this alloy maintains excellent fracture toughness, even at cryogenic temperatures, through the formation of nanometric deformation twining [26]. These properties are attributed to the relatively low stacking fault energy and relatively high shear modulus of the disordered solid solution FCC, which drives large separations between partial dislocations [31]. While the disordered solid solution phase unique to HEAs has demonstrated noteworthy properties, this structure is found to decompose after extended annealing heat treatments [2,32]. Particularly, the precipitation of a Cr-rich sigma σ phase was evident at 1000 hours at 700 °C [2]. The presence of a single stable disordered solid solution phase in HEAs is rare. In a recent review Miracle et al. found that when considering many published alloys that fall in the complex composition space of HEAs, most possess both intermetallic phases along with a disordered solid solution phase [16]. With the current understanding of secondary phase formation in HEAs, there has been an emphasis shift within the field from targeting single disordered solid solution phase alloys to the development of complex HEAs with desirable multi-phase microstructures [33–37].

Motivated by the above discussion, in the current work we determine the phase decomposition of the equiatomic composition of CoCuFeMnNi and study the role of secondary phases in altering the mechanical behavior of the alloy. The motivation for exploring these constituent elements is grounded in the known decomposition of the Cantor alloy CoCrFeMnNi as well as the consideration of thermodynamic properties of the binary interactions of the constituents. As previously discussed, extended annealing heat treatment of the Cantor alloy led to precipitation of a Cr-rich sigma σ phase formed at grain boundaries throughout the material. Sigma phase formation in stainless steels, an analogous conventional alloy to 3d-transition metal HEAs, is found to embrittle the material, leading to significant reduction in toughness [38]. To avoid sigma σ phase formation, Cr is removed from the alloy system. To promote multiple FCC phases within this alloy, Cu is incorporated into the composition due to the immiscibility of Cu with the other constituent elements. Table 1 presents the values of mixing enthalpy ΔH_{mix} calculated by Miedema's model for atomic pairs between all constituent elements [39]. Comparing these binary pairings of the constituents, Cu possesses the largest mixing enthalpies particularly with Fe and Co. Considering the magnitude of mixing enthalpies for Cu in this system along with the fact that Cu possesses the largest metallic radius, 128 pm, of all the constituents, it is expected that Cu segregation will occur in the equiatomic composition of this alloy system. The possibility of multiple phase formation in CoCuFeMnNi makes this system of interest for studying the stability of phases in HEA compositions and the role of these phases in the mechanical performance of the material.

Table 1. Values of mixing enthalpy ΔHmix [kJ/mol] calculated by Miedema's model for atomic pairs between all constituent elements and the atomic radius of each constituent element in the alloy system.

ΔH_{mix} [kJ/mol]	Mn	Fe	Co	Ni	Cu
Mn	X	0	-5	-8	4
Fe		X	-1	-2	13
Co			X	0	6
Ni				X	4
Cu					X
Atomic radius [pm]	127	126	125	124	128

Experimental studies on the equiatomic CoCuFeMnNi are limited, and conflicting microstructural analysis are reported. Tazuddin et al. first reported on the equiatomic composition of CoCuFeMnNi synthesized by vacuum arc melting followed by homogenization and cold rolling [40]. The authors claim the as-cast alloy exhibits a single FCC phase, and their work addressed the evolution of texture in the rolled samples as well as the tensile behavior for the as-cold rolled and annealed samples. Takeuchi et al. conducted a more detailed characterization of the as-cast material formed through induction melting, in which they found the presence of two FCC phases due to segregation of Cu in the alloy [41]. The authors did not report on the mechanical behavior of this dual FCC microstructure. The final report by Sonkusare et al. confirmed the presence of a dual FCC microstructure observed by Takeuchi et al. with the addition of a Fe-Co rich BCC precipitate after a twelve hour annealing heat treatment at 650 °C [42]. Yet again, no mechanical behavior of the samples with these phases present in the microstructure is reported by the authors.

Most recently, Agarwal et al. investigated the varying deformation behavior between increasingly complex alloys within the CoCuFeMnNi alloy system, but the analysis was focused on samples that do not contain the secondary phases previously reported [43]. Considering the various reports on the CoCuFeMnNi alloy system, there is a need for a careful, systematic evaluation of the phase stability in this alloy, paying particular attention to investigating the role of these phases in the mechanical behavior of the alloy.

To address the above points, equiatomic CoCuFeMnNi was experimentally synthesized and thermomechanically processed followed by systematic post deformation annealing (PDA) heat treatments. The microstructural evolution, specifically phase decomposition, during PDA treatments is studied as a function of temperature as well as time. The tensile properties of the material after each processing point are measured to understand the role of phase decomposition on the mechanical behavior and develop design criteria for multi-phase transition metal HEAs.

2.2 Experimental methods

2.2.1 Material preparation

The alloy was synthesized by induction levitation melting, using bulk Co, Cu, Fe, Mn, Ni (purity > 99.7%) in an equiatomic ratio as feedstock material. The material was melted under an Ar atmosphere and cast into a Cu crucible to solidify. This step was repeated four times to achieve chemical uniformity throughout the ingot. Note that the ingot was rotated before each remelting. The ingot was melted a fifth time and then cast into a cylindrical stainless steel die measuring ⌀ 50 mm × 220 mm. The resulting ingot was machined down to remove contaminations from the die then sectioned using electrical discharge machining. To homogenize the as-cast material, bars measuring 120 mm × 35 mm × 12 mm underwent thermomechanical processing. The bars were hot rolled at a temperature of 900 °C for a thickness reduction of ~50% followed by a heat

treatment in an Ar atmosphere at 1000 °C for 4 hours then quenched in water. A portion of the homogenized material was further processed by cold rolling at ambient temperature for a thickness reduction of 60%. The cold rolled material was then sectioned, and various PDA treatments were conducted as described in the results. For each PDA treatment, samples were encapsulated in a fused quartz ampule that was purged with argon and under vacuum during the treatment. All PDA treated samples were quenched into ambient temperature water by breaking the ampule while submerged under water.

2.2.2 Mechanical testing

To assess the mechanical behavior of the alloy after each processing step, tensile tests were performed using an Instron 8801 universal testing machine equipped with a 100 kN load cell and a video extensometer to resolve axial strain. Tensile coupons possessing a 10 mm gauge length, 2.5 mm width, and 1 mm thickness were prepared from the as-cast, homogenized, cold rolled, and PDA treated samples. For all samples that experienced rolling, the rolling direction was oriented along the gauge length. All tests were conducted with a nominal strain rate of $1x10^{-3}$ s^{-1}. Several coupons were tested for each condition to assure reproducibility and the most representative stress-strain curves are presented.

2.2.3 Microstructural characterization

To determine phase composition of each sample, X-ray diffraction patterns were measured using a Rigaku SmartLab X-ray diffractometer (XRD) equipped with a Cu K_α (λ = 0.1542 nm) radiation source. Each run was performed from 20° to 100° with a step size of 0.02° and a speed of 2 steps per second. Each pattern was normalized for comparison.

Analysis of the as-cast, homogenized, and fully recrystallized microstructures was performed on a FEI Quanta 3D field emission gun scanning electron microscope (SEM) equipped

with a pole piece mounted backscatter electron (BSE) detector and an Oxford energy dispersive X-ray spectrometer (EDS). For all rolled samples, micrographs are normal to the rolling direction. All samples were mechanically polished followed by a surface ion milling.

Scanning transmission electron microscopy (STEM) with EDS analysis was performed on a JEOL JEM-2800 TEM operating at 200 kV and equipped with dual EDS detectors. Selected area electron diffraction (SAED) was performed on a JEOL JEM-2100F TEM operating at 200 kV. Specimens were prepared for TEM analysis by mechanical thinning foils of each sample using SiC grit paper followed by ion-milling using a dual ion-beam Gatan PIPS to create electron transparent regions.

2.2.4 Computational thermodynamics

As a retrospective analysis of phase decomposition in this alloy, the CALPHAD approach was employed using ThermoCalc software with the high entropy alloy database version three "TCHEA3". Within this database, all possible binary systems of the five constituent elements for this high entropy alloy have been critically assessed for the full range of compositions and temperatures. According to ThermoCalc, for the possible ternary systems, seven have been critically assessed and one tentatively assessed, leaving two ternary systems unassessed. The data from these assessed systems are used to generate the property diagram for the higher order equiatomic CoCuFeMnNi system.

2.3 Results

2.3.1 Homogenization of the as-cast microstructure

After induction levitation melting and casting, the solidified equiatomic CoCuFeMnNi alloy possess a dendritic dual FCC microstructure. Figure 6 (a) contains the XRD pattern of the as-cast material and Figure 6 (b) shows a BSE micrograph revealing both dendrite and

interdendritic regions. The XRD pattern exhibits a major FCC pattern along with a minor FCC pattern that is shifted to lower two-theta values, indicative of a larger lattice parameter [25]. EDS point analysis determined the dendritic regions are enriched in Fe and Co while the interdendritic regions are enriched in Cu and Mn; Ni is nominally constant throughout the phases.

The resulting microstructure from hot rolling and homogenization of the as-cast material is shown in the BSE micrograph of Figure 6 (d). After this homogenization, the microstructure possesses an equiaxed grain structure with a 30 μm mean grain diameter. The XRD pattern in Figure 6 (c) exhibits a single FCC pattern but to confirm the elements are uniformly distributed, TEM analysis was conducted on the homogenized sample. Figure 6 (e) contains a SAED pattern with a single set of reflections corresponding an FCC phase along the [011] zone axis. In addition to the SAED, STEM EDS of the homogenized sample found no preferential clustering of any constituent elements.

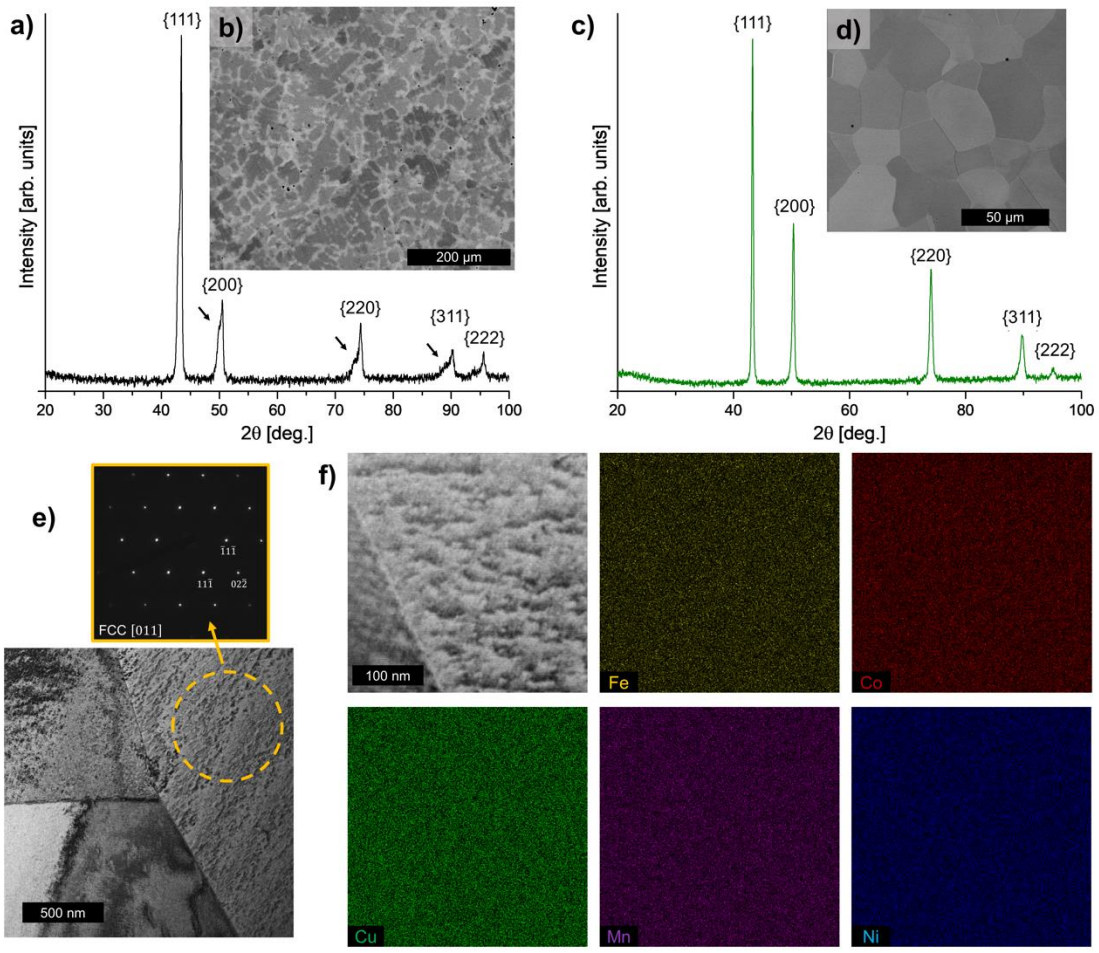

Figure 6. Microstructural analysis for the as-cast and homogenized samples of the equiatomic CoCuFeMnNi alloy including (a) the XRD pattern of the as-cast equiatomic CoCuFeMnNi alloy exhibiting two overlapping sets of FCC peaks, (b) a BSE micrograph of the as-cast state that reveals low Z contrast Cu-lean dendritic regions and high Z contrast Cu-rich interdendritic region, (c) the XRD pattern demonstrating a single FCC phase after hot rolling and homogenization of the as-cast material, (d) a BSE micrograph showing equiaxed grains after homogenization, (e) TEM micrograph of a triple junction of grains in the homogenized sample along with a SAED pattern of the highlighted area indexed to the FCC [011] zone axis, and (f) STEM EDS of the homogenized sample that exhibits a uniform distribution of all five constituent elements.

The mechanical behavior of the as-cast material and the homogenized material are compared in Figure 7 (a). Homogenizing the material led to a decrease in the yield strength of nearly 140 MPa, from 420 MPa in the as-cast state to 280 MPa in the homogenized state. Additionally, the ductility was improved by 10% after homogenizing, from roughly 32% strain at failure in the as-cast state to over 40% strain to failure.

2.3.2 Cold rolled and 0.5 hour post deformation annealing treatments

To systematically study phase decomposition from the single phase state achieved after homogenization, a range of PDA treatments were conducted on cold rolled samples from 500 °C to 1000 °C with an increment of 100 °C. The duration of these PDA treatments was kept constant at 0.5 hours.

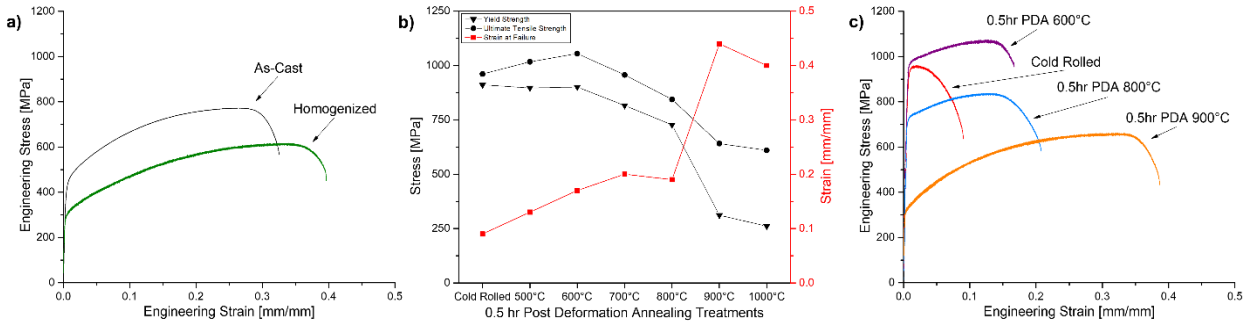

Figure 7. (a) Comparison of the tensile engineering stress-strain curves for the as-cast and homogenized samples, (b) plot of the average yield strength, ultimate tensile strength, and strain at failure for the cold rolled sample and 0.5 hour PDA annealing treatments, and (c) engineering stress-strain curves for the cold rolled, 600°C, 800°C, and 900°C 0.5 hour PDA annealing treatments.

2.3.2.1 Evolution of tensile behavior

Figure 7 (b) plots the average yield strength, ultimate tensile strength, and strain at failure for the cold rolled state as well as each 0.5 hour PDA annealing. Cold rolling produces a substantial increase in yield strength, from the homogenized state, to 910 MPa. This high strength is accompanied by limited strain to failure of 9%. After low temperature (before complete recrystallization) PDA treatments, until 600 °C, the material has a maintained yield strength, 900 MPa, as well as improved ductility, 17% strain at failure. After PDA treatments from 600 °C to 800 °C the yield strength of the material incrementally decreases resulting with a yield strength of 730 MPa after 800 °C and maintained ductility with a strain to failure of 19%. 900 °C marks a significant change to the tensile behavior with a decrease in the yield strength to 310 MPa and an

increase in ductility to 44% strain at failure. After PDA treatment at 1000 °C the trend of softening continues. To better illustrate the evolution of the tensile behavior of these samples, the engineering stress-strain curves of PDA temperature points that mark key transitions in properties are presented along with the cold rolled material in Figure 7 (c). These four sample states will be the focus of microstructural analysis to determine phase decomposition.

2.3.2.2 X-ray diffraction

The XRD patterns, measured normal to the rolling direction, of the cold rolled material and after each PDA treatment are presented in Figure 8. From the full range of two-theta (20°-100°) values, the cold rolled material shows slight {220} texturing. Figure 8 (b) is limited to the breadth of the {220} peak for each sample. As the PDA treatment temperature increases from 500 °C to 600 °C, the pattern shows a single peak with a minor shift of the peak to higher two-theta values. At 700 °C and 800 °C the major peak continues to shift to higher two-theta values and a second FCC {220} peak emerges to the left of the major peak. After 900 °C the secondary FCC {220} peak disappears and the major peak shifts back to lower two-theta values, indicative of a dissolution of the secondary FCC phase.

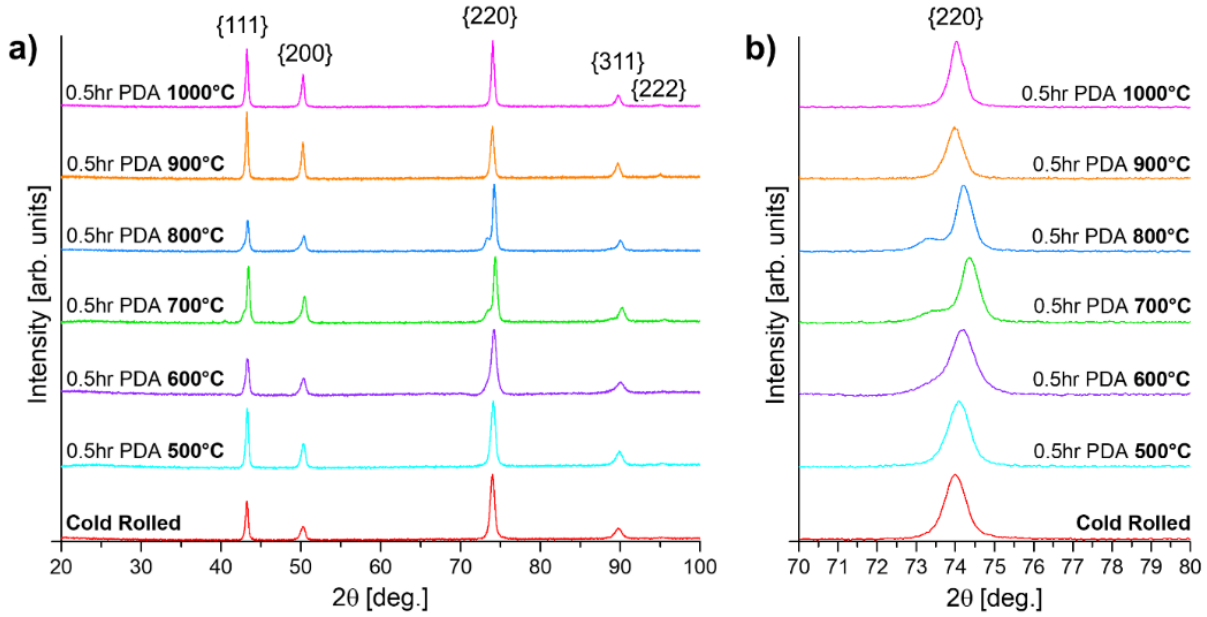

Figure 8. (a) XRD patterns of the cold rolled sample and samples PDA treated for 0.5 hours at a range of temperatures (b) magnified view of 70° to 80° to show the (220) peak evolution.

2.3.2.3 Microstructural analysis of post deformation annealing treatments

While most of the microstructure of the PDA treated samples at 600 °C and 800 °C for 0.5 hours maintained the deformed state from cold rolling, STEM EDS analysis revealed the formation of secondary phases. The BSE micrograph, Figure 9 (a), shows the overall deformed microstructure present in the material after PDA treatment at 600 °C for 0.5 hours. Figure 9 (b) presents a higher resolution examination of the microstructure that reveals fine nanoprecipitates within the deformed material. STEM EDS analysis, Figure 9 (c-g), identified these particles as enriched in Fe and Co. Surrounding these Fe-Co rich nanoprecipitates are regions enriched in Cu. This decomposition of the single FCC matrix phases is confined to regions in the matrix near and on the previous grain boundaries that persist after cold rolling. The Fe-Co rich nanoprecipitates have a mean Feret diameter of 140.6 nm and have an average spacing of 420 nm in the regions of the microstructure they are found.

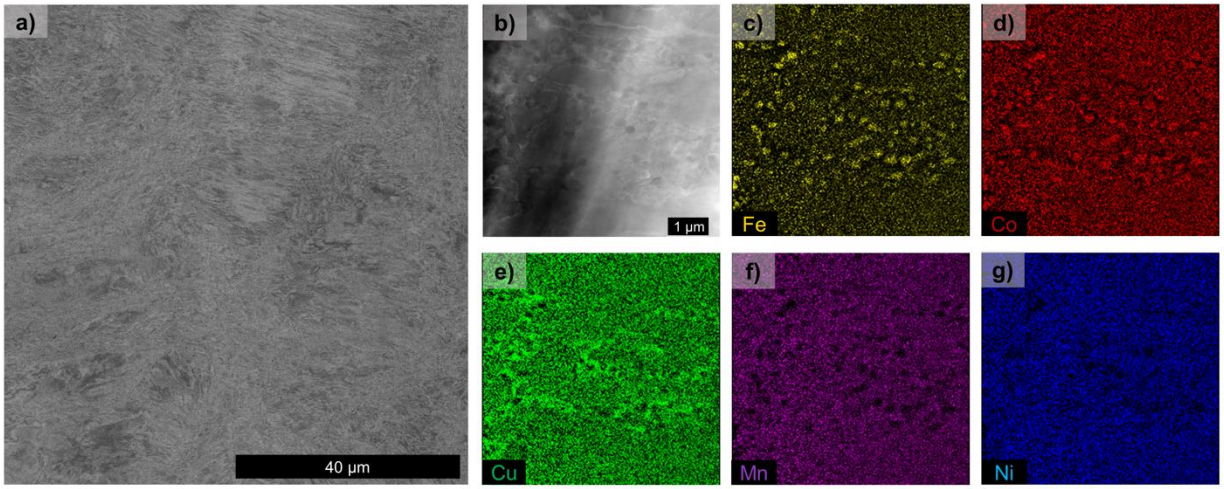

Figure 9. (a) BSE micrograph of the overall deformed microstructure present in the equiatomic CoCuFeMnNi alloy cold rolled after PDA treated at 600 °C for 0.5 hours, (b-g) STEM EDS analysis of particles observed within the deformed microstructure.

Figure 10 shows the microstructure after PDA treatment at 800 °C for 0.5 hours. While a majority of the microstructure maintains a high level of deformation after this PDA treatment, as seen in Figure 10 (a), STEM EDS analysis, Figure 10 (b-g) reveals the onset of recrystallization has occurred with the formation of recrystallized nuclei. The material exhibits pronounced Cu segregation in regions of the deformed microstructure where recrystallized nuclei have formed. The Cu-rich domains are also enriched with Mn but lean of Fe, Co, and Ni. It is important to note that only two FCC phases are present after PDA treatment at 800 °C and no Fe-Co nanoprecipitates are present.

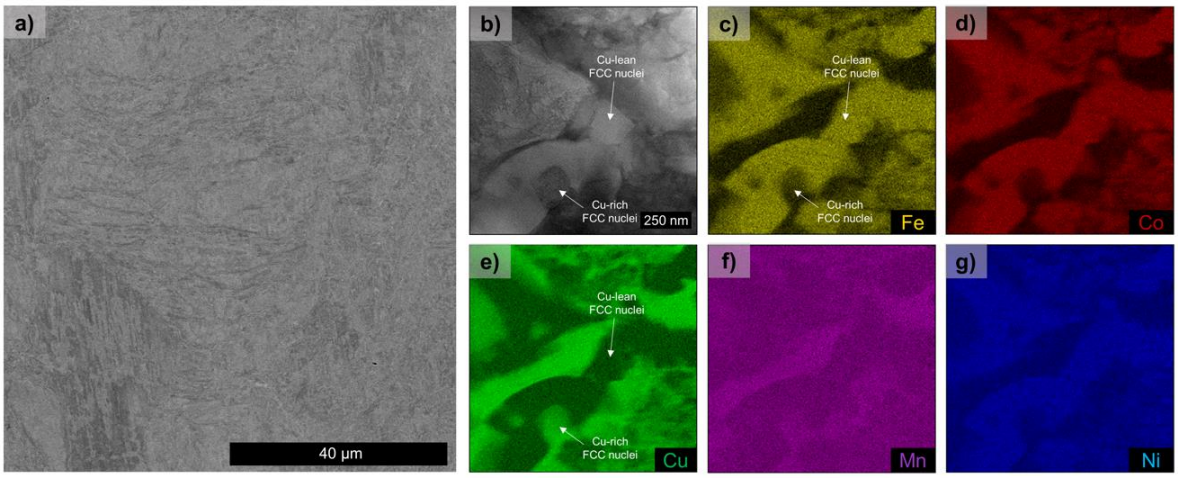

Figure 10. (a) BSE micrograph of the overall deformed microstructure persisting in the equiatomic CoCuFeMnNi alloy cold rolled after PDA treated at 800°C for 0.5 hours, (b-g) STEM EDS analysis of recrystallized nuclei found within the deformed microstructure.

The material PDA treated at 900 °C for 0.5 hours achieved complete recrystallization and initiated early stages of grain growth as seen in the BSE micrograph of Figure 11. The microstructure possesses a uniform equiaxed grain structure throughout with a mean Feret diameter of 8 µm, which is 3.75 times smaller than the initial grain size of the homogenized material. The EDS map in Figure 11 shows the five constituent elements are all uniformly distributed throughout these equiaxed grains.

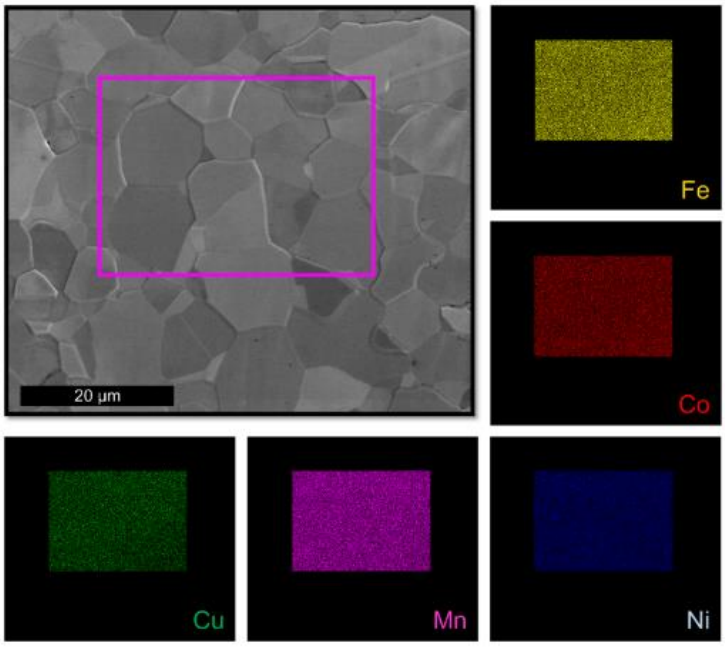

Figure 11. SEM EDS analysis of the equiatomic CoCuFeMnNi alloy cold rolled and PDA treated at 900°C for 0.5 hours.

2.3.3 Extended post deformation annealing treatments

To better understand the role of the secondary phases reported above, additional PDA treatments were conducted at 600 ℃ and 800 ℃ for 2 and 24 hours respectively. The microstructural evolution and mechanical behavior as a function of time are outlined below.

2.3.3.1 600 °C

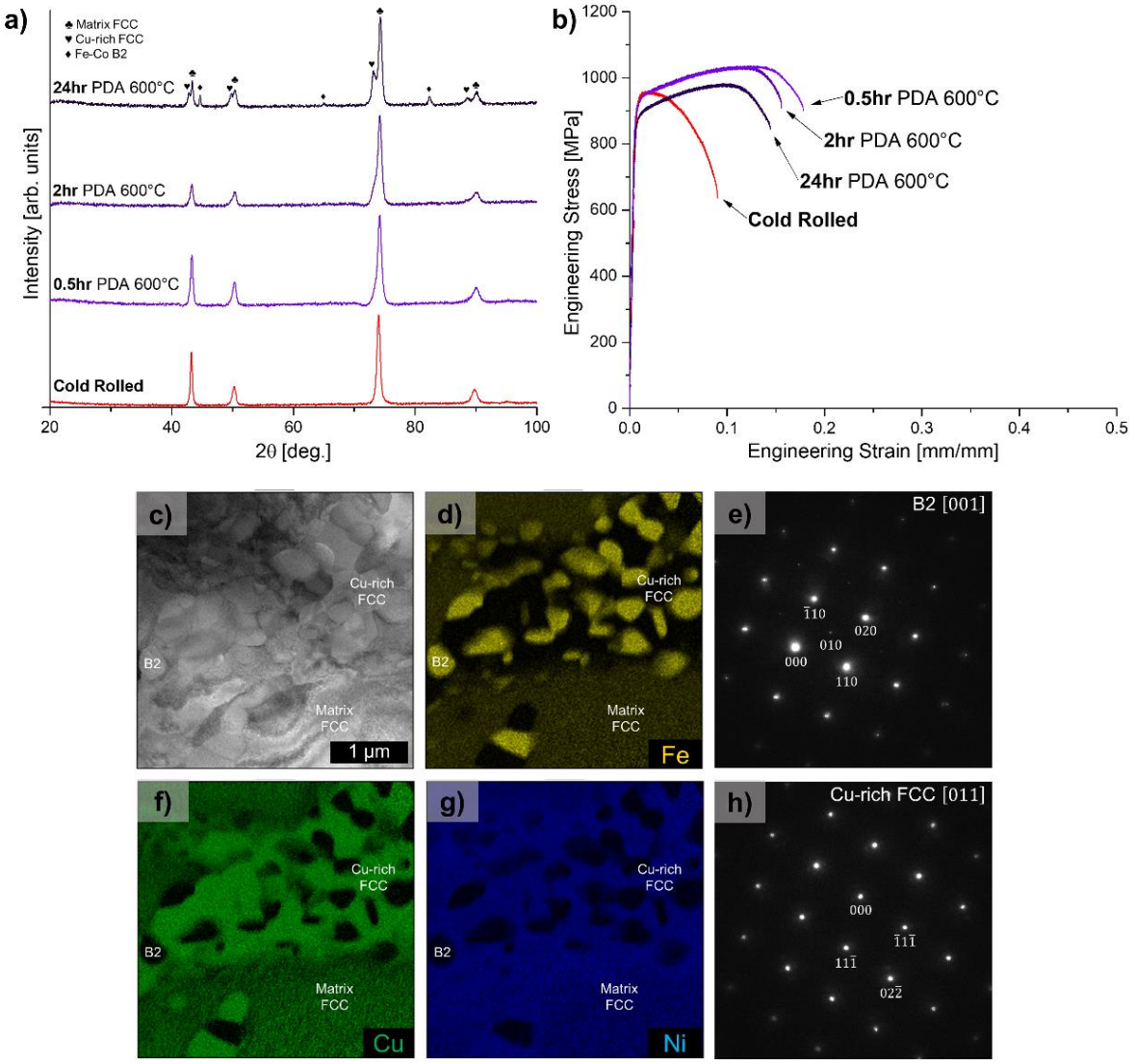

Figure 12. Results of extended time PDA treatments at 600 °C (a) XRD patterns of the cold rolled sample and PDA treated samples at 600°C for 0.5, 2. and 24 hour, (b) tensile engineering stress-strain curves of the cold rolled sample and PDA treated samples at 600°C for 0.5, 2. and 24 hours, and STEM EDS and SAED analysis at a previous grain boundary in the equiatomic CoCuFeMnNi alloy cold rolled and PDA treated at 600°C for 24 hours, (c) STEM micrograph of the previous grain boundary, (d) EDS concentration map for Fe revealing B2 phases, (e) the SAED of the Fe-Co rich precipitate labelled B2 in (c), (f) EDS concentration map for Cu revealing nuclei of Cu-rich FCC phase, (g) EDS concentration map for Ni confirming the segregation of Ni in the phases present, (h) SAED of the Cu-Mn rich nucleated grain labelled Cu-rich FCC in (c).

After PDA treatment at 600 °C for 24 hours, the phase decomposition is appreciable through XRD. Figure 12 (a) compares the XRD patterns of the cold rolled material and the 600 °C PDA samples treated for 0.5, 2, and 24 hours. The XRD pattern for the sample treated for 2 hours maintains a single FCC pattern although slight broadening to lower two-theta values is evident. After the 24 hour PDA treatment, patterns corresponding to the matrix FCC, Cu-rich FCC, and an ordered BCC (B2) phase are distinguishable. STEM EDS mapping in parallel with SAED for the 24 hour PDA treated sample determined the B2 phase corresponds to the Fe-Co rich nanoprecipitates. Figure 12 (c,d,f,g) shows a STEM EDS map containing all three phases, the Fe-Co rich B2 phase, the Cu-rich FCC phase and the near equiatomic matrix FCC phase, present throughout the microstructure of the 24 hour PDA sample. As the PDA treatment time increased, the Fe-Co nanoprecipitates coarsened significantly to a mean Feret diameter of roughly 480 nm. Similarly, the phase produced by Cu segregation, which was limited to films at grain boundaries in the 0.5 hour PDA treatment, nucleated equiaxed grains. The coarsening of these phases allowed for analysis via SAED, illustrated in Figure 12 (e) and Figure 12 (h). SAED of the Fe-Co rich precipitate labelled B2 throughout the micrographs of Figure 12 (c) produced the diffraction pattern seen in Figure 12 (e), which indexes to a BCC [001] zone axis and clearly contains superlattice reflections indicative of an ordered B2 structure. The Cu-rich grain labeled FCC throughout the micrographs of Figure 12 (c) produced the diffraction pattern seen in Figure 12 (h), which indexes to an FCC [011] zone axis, unique to a disordered FCC structure. Figure 12 (b) presents the tensile behavior of the extended PDA treatments at 600 °C. The tensile properties after the 2 hour PDA treatment are nearly identical to the 0.5 hour PDA treatment with a yield strength of 900 MPa and strain at failure of 16%. The 24 hour PDA treatment marked a decrease in yield strength to 860 MPa and strain to failure to 14%.

2.3.3.2 800 °C

Figure 13 (a) shows the XRD patterns of the samples after extended PDA treatments at 800 °C. The secondary FCC pattern present in the 0.5 hour PDA treatment is maintained after 2 and 24 hours. The major FCC peak width narrows with increasing time, making the secondary peaks more distinguishable. BSE micrographs of the 24 hour PDA treatment at 800 °C in Figure 13 reveal a fully recrystallized microstructure composed of two FCC phases. Figure 13 (c) shows a low magnification view of the recrystallized microstructure, which shows the heterogenous distribution of a bright (high Z contrast) phase corresponding to the Cu-rich phase. Figure 13 (d) is a higher magnification view which shows the equiaxed grains of the major FCC phase as well as the narrow domains of the Cu-rich FCC that are found between the major FCC grains. The tensile behaviors of these samples after extended PDA treatments at 800 °C are shown in Figure 13 (b). At 800 °C the 2 hour PDA treatment, samples possess a lower yield strength, of 620 MPa, and increased ductility, with a strain to failure of 24%, as compared to the sample PDA treated for 0.5 hours. After the 24 hour PDA treatment a more significant drop in yield strength, to 380 MPa, is observed as well as an increase in ductility, with a strain to failure of 32%.

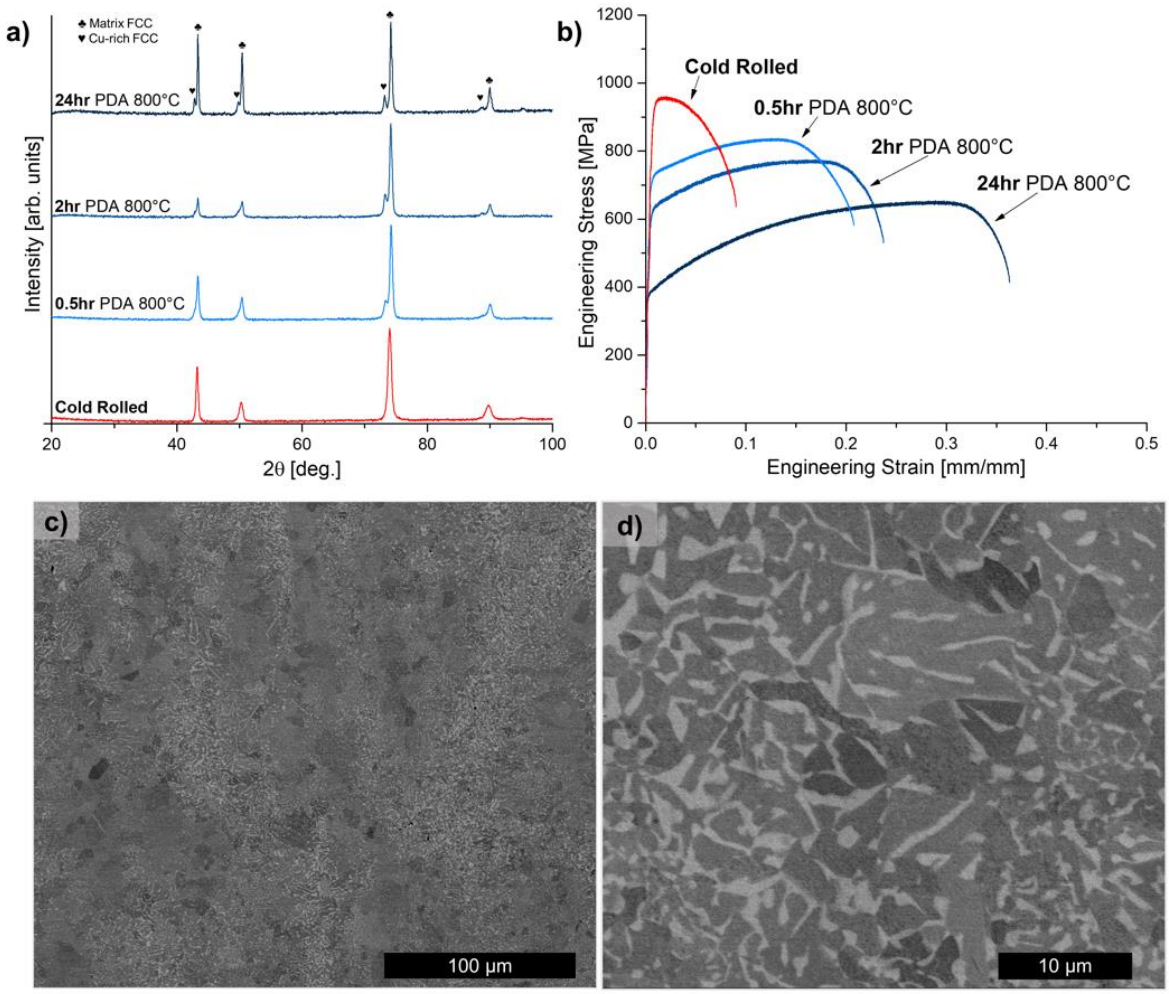

Figure 13. Results of extended time PDA treatments at 800 °C (a) XRD patterns of the cold rolled sample and PDA treated samples at 800°C for 0.5, 2. and 24 hours, (b) tensile engineering stress-strain curves of the cold rolled sample and PDA treated samples at 800°C for 0.5, 2. and 24 hours, and BSE micrographs of the equiatomic CoCuFeMnNi alloy cold rolled sample PDA treated at 800°C for 24 hours (c) low magnification and (d) high magnification.

2.4 Discussion

2.4.1 Phase decomposition

The equiatomic bulk composition of CoCuFeMnNi exhibited three distinct phases that were present in the microstructure at various temperature ranges: the near equiatomic disordered FCC matrix phase, a Cu-rich disordered FCC phase, and the ordered Fe-Co rich B2 phase.

The alloy achieved a single disordered solid solution FCC phase at temperatures above 900 °C as seen in the homogenized material as well as the cold rolled and PDA treated at 900 °C for 0.5 hours. In previous reports of the homogenized single FCC state of this HEA composition, Cu-rich nano clusters are identified through atom probe tomography (APT) and electron diffraction techniques [42,43]. Since Cu-rich clusters are not identified in the homogenized samples reported in this study, their formation could be dependent on the processing parameters namely quench rate after homogenization heat treatments. Further investigation of atomic scale Cu segregation in this alloy and similar Cu containing HEAs is needed to confirm their presence. Nevertheless, this solutionizing window, from roughly 900 °C to the melting point where the reported Cu-rich FCC phase and Fe-Co rich B2 precipitates dissolve into the matrix FCC phase, is attributed to the relatively high configurational entropy of the disordered solid solution phase. According to the Gibbs free energy equation, at sufficiently high temperatures, the entropy of the disordered phase would begin to dominate, leading to high temperature stability of the solutionized phase, as is the case with many HEAs [16].

At lower temperatures, below 900 °C where entropy has less influence on the stability of phases, the immiscibility of Cu with the other constituent elements leads to Cu segregation and ultimately to the formation of a Cu-rich disordered FCC phase. Cu segregation is evident in all samples processed below 900 °C. Figure 8 (b) reveals Cu segregation at 700 °C and 800 °C in terms of the emergence of the secondary {220} peak at lower two-theta values indicative of a larger lattice parameter due to the enrichment of the largest constituent element Cu. But even at lower temperature the major {220} peak seems to shift towards higher two-theta values due to the minor Cu segregation that is not resolvable by XRD due to peak convolution. The STEM EDS results after PDA treatment at 600 °C, as shown in Figure 9, reveal this minor segregation of Cu

that is localized around the Fe-Co rich precipitates. At these relatively low temperatures, where diffusion through the matrix may be sluggish, Cu segregation is limited to interfaces and grain boundaries because they act as preferential nucleation sites for secondary phases as well as preferential diffusion pathways [44]. Figure 10 shows that the PDA treatment at the highest temperature examined that falls below the solutionizing window, produced widespread Cu segregation that was not limited to grain boundaries. Also, from Figure 10 it is evident that this segregation occurs simultaneously with the onset of recrystallization at 800 °C as we see small nuclei beginning to form. Interestingly, both the Cu-rich FCC and the Cu-lean FCC are nucleating during the onset of recrystallization. The EDS in Figure 10 shows qualitatively that the Cu-rich FCC nuclei also contain significant Mn and some Ni, which match the predicted behavior from the enthalpy of mixing for binaries found in Table 1. Mn and Ni possess the lowest enthalpy of mixing for all the constituents of the alloy. Nucleated grains of the Cu-rich FCC also occur within the PDA treatment at 600 °C and at 800 °C for 24 hours owing to the stability of this phase at lower temperatures.

Lastly, the alloy possesses a Fe-Co rich ordered B2 phase that precipitates and grows during lower temperature PDA treatments and eventually dissolves into the matrix between 600 °C and 800 °C. The B2 phase is most evident after PDA treatments at 600 °C. STEM EDS results show that the B2 phase begin to nucleate throughout the microstructure of the alloy after 0.5 hours at 600 °C and coarsen significantly after 24 hours. SAED confirms the ordered nature of these precipitates, which agrees with the results of Sonkusare et al. who observed B2 nano precipitates at similar heat treatment temperatures [42].

The CALPHAD approach, using ThermoCalc's TCHEA database version 3.0, allowed for comparative analysis between the predicted stability of phases to the phases observed

experimentally. An effective method of presenting the equilibrium phases predicted over a range of temperatures for a given composition is generating a step diagram as seen in Figure 14 (a) for the equiatomic composition of the CoCuFeMnNi alloy. From the melting point, 1157 °C, to 727 °C, CALPHAD predicts the formation of a single stable disordered FCC phase with all the constituent elements present. The presence of the Cu-rich disordered FCC phase is predicted from low temperature to 727 °C and the Fe-Co rich B2 phase is predicted from low temperature to 559 °C. While the precise temperature points at which the phases form do not match experiment, the step diagram does agree with the phases observed throughout the thermomechanical processing. The alloy can be homogenized at sufficiently high temperatures to incorporate all constituent elements on a single FCC lattice. The presence of the Cu-rich FCC phase is expected at intermediate temperatures as seen in the PDA treatment at 800 °C and the Fe-Co rich B2 phase is present at low temperatures corresponding to the PDA treatment at 600 °C. One reason for this discrepancy in phase stability is the fact that the experimental material cannot be considered to be at thermal equilibrium. The second can be understood by examining the difference in chemical composition of each distinct phase from experiment and CALPHAD. The coarsening of secondary phases during the 600 °C PDA treatment for 24 hours allows for quantitative EDS measurements of each phase observed. This analysis is plotted against the predicted chemistry of each phase calculated by CALPHAD at 500 °C, the highest temperature that the model predicts the formation of all three phases, in Figure 14 (b-d). When comparing the experimental and predicted data, the chemistry of the stoichiometric ordered Fe-Co B2 phase is in relatively good agreement, with only minor enrichment on Cu and Mn in the experimental data compared to the model. The Cu-rich phase on the other hand, is significantly higher alloyed with Mn and Ni than simulated. The predicted equilibrium Cu-rich phase is calculated as an effectively pure Cu phase, which is unlikely

to occur particularly due to the fact that Cu has the lowest mixing enthalpy with Mn and Ni out of all the constituent elements. Understanding the deviation from the ideal chemistry predicted in CALPHAD to the more alloyed chemistries found experimentally, it is expected that the higher alloyed phases can experimentally be stable at higher temperatures. The modeling of a segregating element in a complex composition seems to be unreliable in ThermoCalc's current iteration of the TCHEA database. Further analysis of this inconsistency will be the subject of future work. It is also important to point out that the matrix disordered FCC phase agrees reasonable with the CALPHAD model. Any inconsistencies in these values could stem from the proximity to the segregated region at the grain boundary in Figure 12 (c).

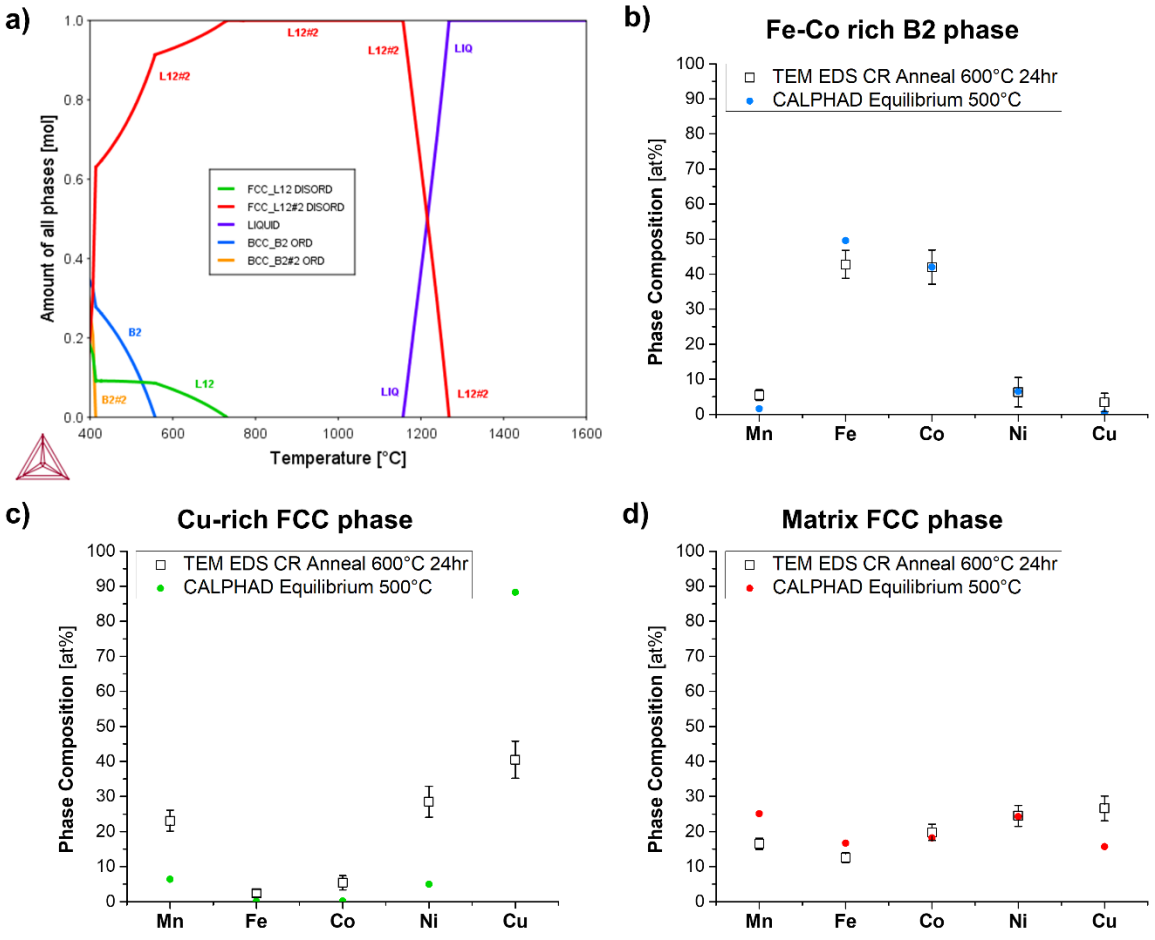

Figure 14. (a) Equilibrium step diagram of the equiatomic CoCuFeMnNi alloy from 400°C to 1600°C calculated by the CALPHAD approach using ThermoCalc software with the TCHEA 3.0 database and a comparison of phase composition experimentally measured from STEM EDS of the equiatomic CoCuFeMnNi alloy cold rolled sample PDA treated at 600°C for 24 hours and predicted from equilibrium CALPHAD calculations for the alloy at 500°C where all three phases are predicted (b) Fe-Co rich B2 phase, (c) Cu-rich FCC phase, and (d) the matrix FCC phase.

2.4.2 Mechanical behavior

The overall trend for the mechanical behavior in the 0.5 hour PDA treatments is indicative of the roles of recovery, recrystallization, and grain growth; a trend well established in thermomechanically processed 3d-transition metal HEAs [45]. However, by comparing specific samples, the role of phase decomposition, specifically the presence of the Cu-rich disordered FCC phase and the Fe-Co B2 phase, on the mechanical behavior becomes apparent. The initial 0.5 hour

PDA treatment at 600 °C demonstrated an effectively maintained yield strength and increased strain to failure compared to the cold rolled material. When considering a single FCC phased metal, the increase in strain to failure below the recrystallization temperature is attributed to the annihilation of some of the dislocations formed after deformation, known as recovery [46]. With fewer dislocations, the contribution of dislocation strengthening will diminish, leading to a reduced yield strength. But within the CoCuFeMnNi alloy, the yield strength is maintained, due to the nucleation of the Fe-Co B2 nano-precipitates. These nano-precipitates likely lead to precipitation hardening as they are sufficiently small, equiaxed, well dispersed, and atomically ordered. To estimate the strength due to these nano-precipitates and compare to the expected loss of strength due to dislocation annihilation, a model for the precipitation shearing mechanism is considered as outlined in reference [47]. When considering precipitates of this size with assumed incoherent interfaces, their strength due to the shearing mechanism that two factors can contribute to the overall strength of the material: order strengthening ($\Delta\sigma_{os}$) or modulus mismatch strengthening ($\Delta\sigma_{ms}$). The larger of the two factors is used as the strength increment the precipitation shearing mechanism. $\Delta\sigma_{os}$ can be calculated by:

$$\Delta\sigma_{os} = M0.81\frac{\gamma_{apb}}{2b}\left(\frac{3\pi f}{8}\right)^{\frac{1}{2}}$$

and $\Delta\sigma_{ms}$ by:

$$\Delta\sigma_{ms} = M0.0055(\Delta G)^{\frac{3}{2}}\left(\frac{2f}{G}\right)^{\frac{1}{2}}\left(\frac{r}{b}\right)^{\frac{3m}{2}-1}$$

where M is the mean orientation factor (3.06 for a FCC polycrystalline matrix), G is the shear modulus of the matrix phase [43], ΔG is the difference in shear modulus between the precipitate and the matrix phase, f is the volume fraction of the precipitates estimated by the measured size and spacing reported in section *3.2.3*, r is the radius of the precipitates, m is 0.85, b is the magnitude

of the burgers vector ($\sqrt{2}/2a$) where a is the lattice parameter calculated from XRD), and γ_{apb} is the antiphase boundary free energy of the precipitate phase [48]. In addition to these calculations, the overall increment of strength is subject to a composite model because the Fe-Co rich nano-precipitates are only present in a region surrounding the previous grain boundaries of the material as described above in *2.3.2.3*. Accounting for this the larger calculated strength increment was that of the order strengthening factor that may be responsible for an estimated 106 MPa. This additional contribution may explain why the yield strength was maintained after PDA treatment at 600 °C for 0.5 hours since this is roughly on the order of magnitude of the drop in strength expected for dislocation annihilation [49].

The importance of their size and distribution in the microstructure can be appreciated when considering the evolution of mechanical behavior during extended PDA treatments at 600 °C. The coarsening of the microstructure from 2 hours to 24 hours leads to a drop in both the yield strength and strain to failure of the material. This trend means that there is a critical size of the B2 phase at which it will no longer contribute to the strength of the material. It is expected, through optimization of the thermomechanical processing of this alloy, that an ideal size and distribution of the Fe-Co B2 phase could be achieved but the goals of this study were to initially identify the role of each phase. In the 0.5 hour PDA treatment, the most significant Cu segregation occurred at 800 °C but the effect of this phase decomposition on the mechanical behavior is convoluted by the onset of recrystallization. At the onset of recrystallization in this alloy, the recrystallized nuclei of both the Cu-rich disordered FCC and the near equiatomic disordered FCC form and it is unclear whether the chemical segregation or the elimination of dislocations contributes to the reduced yield strength and increased strain to failure. In order to better understand the role of the Cu segregation in the formation of the Cu-rich disordered FCC, the mechanical behavior of the PDA treated

sample at 800 °C for 24 hours is compared to that of the PDA treated sample at 900 °C for 0.5 hours. Since the microstructures of these two samples are both fully recrystallized and possess grain sizes on the same order of magnitude, the only distinction between them is the Cu-rich disordered FCC phase formed after PDA treatment at 800 °C for 24 hours. The addition of the Cu-rich disordered FCC phase leads to an increase in the yield strength of 70 MPa and a decrease in the ductility of 10%. These trends of increasing strength and decreasing ductility are also observable when comparing the dual phase of the as-cast material with the single phase of the homogenized material, although the equality of all other the microstructural features is not as clear as in the PDA treated at 800 °C for 24 hours and 900 °C for 0.5 hours. When the Cu-rich disordered FCC phase is present the microstructure contains more phase boundary interfaces that can obstruct dislocation motion leading to enhanced strength with decreased ductility. Understanding the role of this dual phase microstructure can be applied to the design of future FCC based HEAs that exhibit similar phase decomposition.

2.5 Summary

Phase decomposition in equiatomic CoCuFeMnNi was systematically studied through thermomechanical processing followed by post deformation annealing (PDA) treatments. The secondary phases formed in the material during these processing steps were confirmed by CALPHAD and their role on the mechanical behavior elucidated. The following key points can be taken from the current work:

1. The equiatomic CoCuFeMnNi alloy exhibits three distinct phases, the primary equiatomic disordered FCC phase, a Cu-rich disordered FCC, and Fe-Co rich ordered B2 precipitates.
2. Due to the significant immiscibility of Cu with the other constituent elements, Cu segregates within the microstructure during PDA treatments below 800 °C and eventually

leads to the formation of a Cu-rich disordered FCC phase which is stable within the alloy until 800 °C to 900 °C.

3. PDA treatment of the CoCuFeMnNi alloy at 600 °C achieved the nucleation and growth of Fe-Co rich ordered B2 nano-precipitates that are a stable secondary phase until the phase underwent dissolution between 600 °C to 800 °C.
4. ThermoCalc CALPHAD analysis with the TCHEA 3.0 database underpredicts the thermal stability of secondary phases as compared to experimental observation. The analysis agreed with the chemical composition of the Fe-Co rich B2 phase and the matrix disordered FCC but predicted the Cu-rich phase to be a pure Cu phase segregating while experimentally the phase is also alloyed with Mn and Ni.
5. Deconvoluting the recrystallization events within these samples from the role of secondary phases, the Fe-Co B2 phase on the order of 125 nm contributes to the strength of the alloy through precipitation strengthening, and the Cu-rich disordered FCC increases strength while reducing ductility through the introduction of additional phase interfaces.

Chapter 3 : Influence of constituent element concentration on the mechanical behavior of solid solution CoCuFeMnNi high entropy alloys

3.1 Background

As the previous chapter highlighted for the equiatomic CoCuFeMnNi HEA, many 3d-transition metal based HEAs that can achieve a single FCC phase, also exhibit phase decompositions at intermediate temperatures [2,32]. Understanding the possibility of secondary phase formation is important for effectively designing these alloys for experimental study of the effects of composition on the behavior of the alloy. Special care must also be taken to process the material at temperatures where a single phase is stable. Since the majority of currently studied HEAs are FCC based alloys, high pressure torsion (HPT) has been implemented to study nanostructured states of some HEA compositions including CoCrFeMnNi and AlCoCrFeNi [50–55]. In general, these studies report that HEAs achieve similar levels of grain refinement as conventional alloys and pure metals. The increased volume of grain boundaries acts as preferential nucleation sites for secondary phases that are stable at low temperatures. This further demonstrates the importance of processing these alloys at temperatures where a single phase is stable. It is interesting to note, however, that few studies have been conducted on the CoCuFeMnNi HEA system that primarily focus on the equiatomic composition of the alloy synthesized through conventional casting routes [40–42]. These studies found that while the system can exhibit phase decomposition at lower temperatures, the alloy can be homogenized at high temperature to form a single FCC phase. The primary focus of these studies is the investigation of the microstructure of the alloy and thus limited mechanical testing has been published. Most recently, the equiatomic CoCuFeMnNi alloy was compared to the equiatomic compositions of its lower order, quaternary and ternary systems, but no investigation into non-equiatomic compositions of the quinary alloy [43]. While the equiatomic composition of a given HEA system has been the traditional starting

point of experimental studies, recent advances in calculated phase diagram (CALPHAD) approaches have enabled the prediction of stable phases in complex compositions of HEAs [6,29]. In this study, using a CALPHAD approach designed for HEA compositions, non-equiatomic compositions are selected that are predicted to have a stable single FCC phase like the equiatomic composition but with limited concentrations of specific constituent elements. This allows to better understand the role of key constituent elements in the overall mechanical behavior and thermal stability of the alloy. Specifically, in the HEA system CoCuFeMnNi, non-equiatomic compositions with decreased concentrations of Cu and Mn are considered to investigate the role of these two constituent elements.

3.2 Experimental methods

Target compositions from the CoCuFeMnNi alloy system were selected based on thermodynamic predictions using the calculated phase diagram (CALPHAD) approach. ThermoCalc software coupled with a specialized high entropy alloy database: TCHEA 3.0 allowed for the prediction of stable phases at a range of temperatures for compositions within the CoCuFeMnNi alloy system. The selected compositions, equiatomic $Co_{20}Cu_{20}Fe_{20}Mn_{20}Ni_{20}$ at.% and non-equiatomic $Co_{26}Cu_{10}Fe_{27}Mn_{10}Ni_{27}$ at.%, were experimentally synthesized using induction levitation melting with feedstock material of purity >99.7%. The two alloys were melted in an inert environment and cast into a crucible to solidify. The process was repeated four times to ensure uniformity of chemistry within the cast ingots. Discs with a radius of 7.5 mm and a thickness of 0.8 mm were sectioned from the ingots using electric discharge machining (EDM), and homogenized under vacuum at 1100 °C for 12 hours, followed by a water quench. After homogenizing the samples of each alloy to ensure a single FCC phase, HPT was utilized to introduce severe plastic deformation in the discs. HPT was conducted on each disc at room

temperature with a pressure of 4 GPa for four turns at a speed of 0.5 rpm. Additional details of the HPT technique can be found in reference [56]. The resulting discs of both the equiatomic and non-equiatomic alloys were sectioned with the EDM to produce tensile coupons and samples for microstructural characterization. In addition to the as-HPT state, samples of each composition were heat treated after HPT under vacuum at 1000 °C for 30 minutes followed by a water quench.

Microstructural characterization was conducted by X-ray diffraction (XRD) and scanning electron microscopy (SEM). XRD patterns of each sample were measured using a Rigaku Smartlab X-ray diffractometer equipped with a Cu K_α radiation source. A FEI Quanta 3D field emission gun scanning electron microscope with a secondary electron (SE) Everhart-Thornley detector and a backscatter electron (BSE) detector was used to image the microstructure of each sample and fracture surfaces of tensile coupons.

For each alloy the mechanical behavior of the as HPT samples as well as the HPT and heat-treated samples was determined through tensile tests. Tests were carried out on an Instron E 3000 Electropuls universal testing machine with a 5 kN loadcell and a video extensometer to measure strain. Tensile coupons with 4 mm gauge length, 2 mm width and 0.5 mm thickness were cut from discs at the mid-radius position to assure consistency across all samples. All tests were conducted with a nominal strain rate of $1x10^{-3}$ s^{-1}. For each alloy and processing step several coupons were tested to ensure reproducibility.

3.3 Results and discussion

Study of the CoCuFeMnNi alloy system began with the predictions from CALPHAD. Point equilibrium calculations were performed to predict the stable phases of a given composition from the alloy system at a given temperature. By varying each element and determining phase stability, the selection of two compositions for experimental synthesis were chosen: equiatomic

$Co_{20}Cu_{20}Fe_{20}Mn_{20}Ni_{20}$ at.% and non-equiatomic $Co_{26}Cu_{10}Fe_{27}Mn_{10}Ni_{27}$ at.%. From CALPHAD both compositions are predicted to possess a single FCC phase at sufficiently high temperatures until the melting event. Moreover, the equiatomic composition is often targeted when exploring new HEA systems particularly when the alloy achieves a single phase. The non-equiatomic composition was selected specifically to limit the amount of Cu in the alloy. With these two compositions, the role of Cu in the strengthening and processability of this HEA system can be studied. Specifically, the microstructural evolution after severe plastic deformation and after post deformation annealing heat treatment as well as the mechanical behavior of these samples are investigated in the following sections.

3.3.1 Microstructural evolution

The processing of the two HEA compositions induced significant microstructural changes. To systematically study these changes, we characterized samples after key processing steps. In previous work, the homogenization of the as cast materials for both compositions was confirmed to produce a coarse grained, hundreds of micron grain diameter, single FCC phase. To determine the effects of HPT on each composition, XRD patterns of the as-HPT samples are plotted in Figure 15.

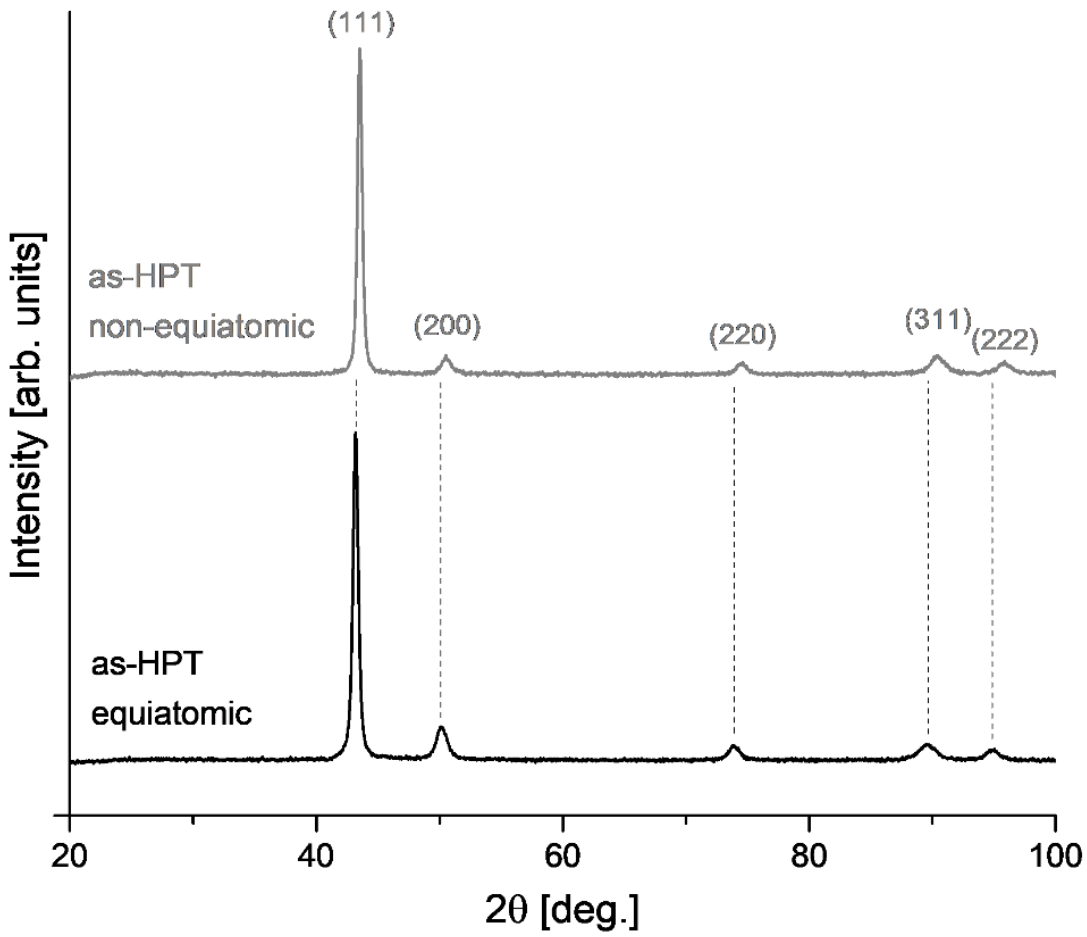

Figure 15. XRD patterns of the as-HPT state for both the non-equiatomic (top) and equiatomic (bottom) compositions exhibiting broad peaks corresponding to a single FCC phase.

After HPT, both compositions maintain a single FCC pattern, as indexed in Figure 15, but the patterns possess appreciable broadening. This broadening is most likely associated with the grain refinement and strain that is expected from severe plastic deformation processing routes such as HPT [57]. While an exact grain size is not determined from the XRD patterns provided, TEM investigation of the as-HPT samples is ongoing and will provide a quantified grain size that is expected to be on the order of 50 nm. Another important observation from the XRD patterns in Figure 15 is the peak shift of the FCC pattern of the non-equiatomic composition to higher two-theta values as highlighted by the vertical dotted lines between the two patterns. Such a shift, which increases with increasing two theta value, is directly related to the variation in lattice parameter

between the two alloy compositions. To calculate the lattice parameter of the FCC phase in each composition, the Nelson-Riley extrapolation method was used [58]. The resulting calculated lattice parameters for the equiatomic and non-equiatomic compositions are 3.625 Å and 3.603 Å respectively. This difference is due in part by the reduction of the concentration of Cu and Mn in the non-equiatomic alloy. Cu and Mn have the largest atomic radii of all the constituent elements at 128 pm and 127 pm respectively, so they contribute most to the lattice parameter of the solid solution FCC phase in each composition.

To assess the thermal stability of the nanostructured samples of each composition while avoiding phase decomposition at intermediate temperatures, heat treatments on the HPT samples were carried out at 1000 °C for 30 min. The temperature was chosen based on the initial CALPHAD that predicted a single FCC phase for both compositions at this temperature. Figure 16 presents the XRD patterns of the samples of each composition after this high temperature heat treatment.

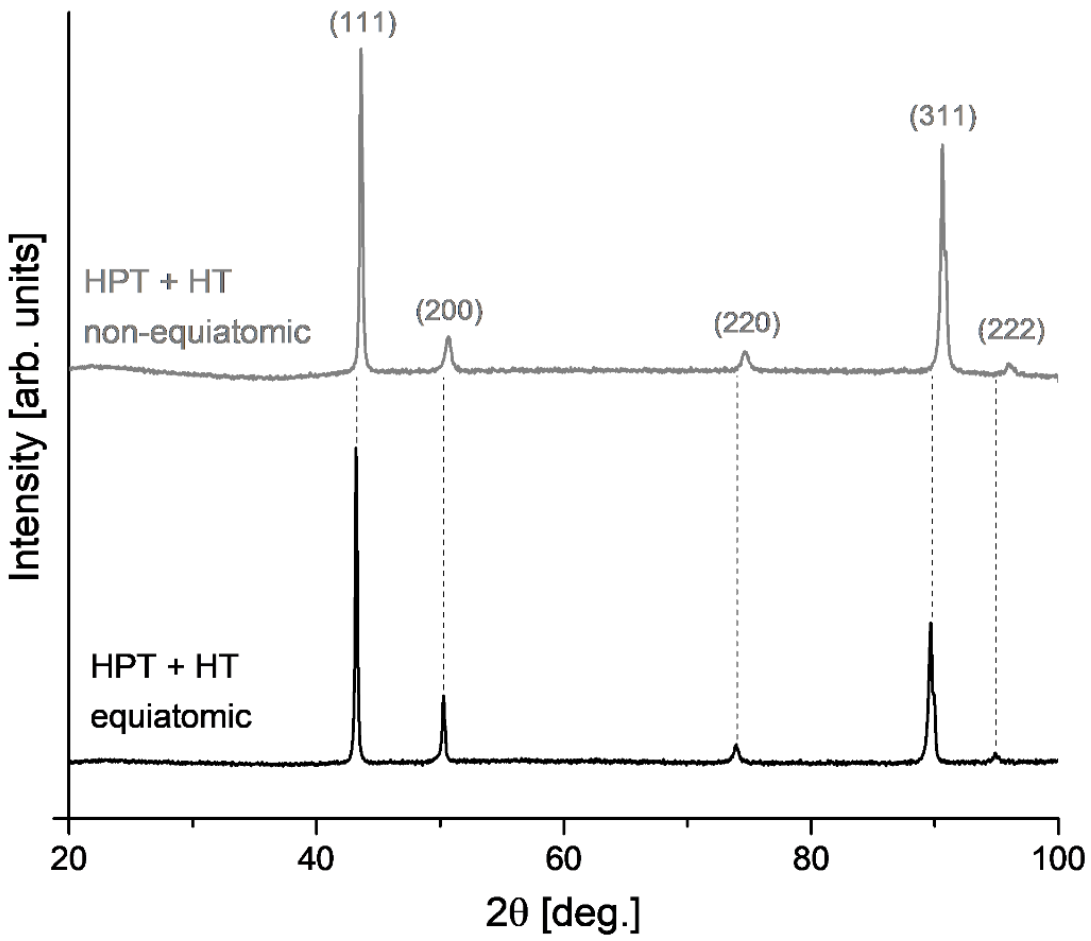

Figure 16. XRD patterns of the samples heat treated at 1000 °C for 30 minutes after HPT (HPT + HT) for both the non-equiatomic (top) and equiatomic (bottom) compositions exhibiting narrow peaks corresponding to a single FCC phase.

After heat treatment, both compositions remain a single FCC phase based on the indexed patterns. Comparing to the as-HPT XRD patterns, both compositions exhibit narrower peaks indicative of grain growth. Shoulders emerge on the {311} peak of both compositions but these were confirmed as the convolution of diffraction of Cu $K_{\alpha 2}$ with the primary Cu $K_{\alpha 1}$ radiation. The peak positions for each composition are consistent with the as-HPT samples confirming the difference in lattice parameter between the two compositions. To confirm that significant grain growth occurred during the heat treatment, these samples were imaged by BSE SEM to resolve

channeling contrast due to varying grain orientation in the single-phase samples. Figure 17 shows representative BSE SEM micrographs of the equiatomic and non-equiatomic compositions.

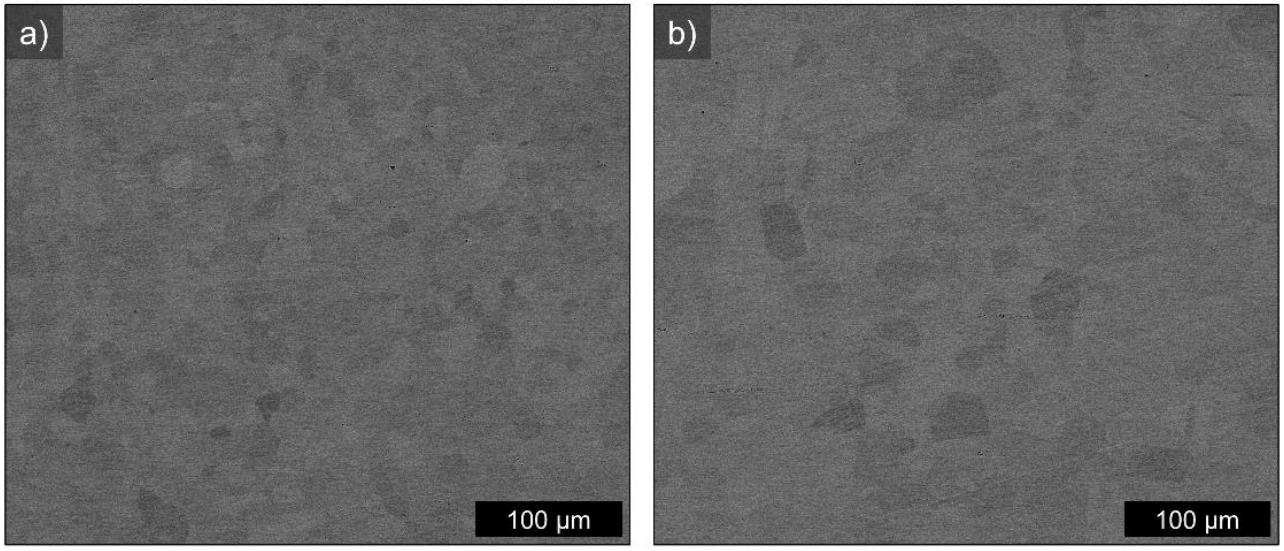

Figure 17. BSE micrographs of (a) the equiatomic composition heat treated after HPT and (b) the non-equiatomic composition heat treated after HPT revealing grain morphology through channeling contrast.

From these micrographs the microstructural features of each composition after HPT and heat treatment can be qualitatively described. Preliminary measurements of the grains resolved in Figure 17 show a general trend of 20-60 µm grains in the equiatomic composition while the non-equiatomic composition contains grains that are larger up to 90 µm. Additionally, these preliminary observations of the microstructure, limited twin like boundaries are observable in the equiatomic composition while in the non-equiatomic composition twin like boundaries are observable throughout. By processing these two compositions in an identical manner, the differences in the thermal stability can be attributed to the variation of constituent concentrations. While the quantification of diffusion in HEAs has been challenging and extensively debated, the current understanding is that the complex interdiffusion of five or more constituent elements can significantly affect diffusion kinetics [59]. Considering the larger grains observed in the non-

equiatomic composition compared to the equiatomic composition, Cu and Mn may play a role in the grain growth kinetics of these alloys. The propensity to form twins within HEAs has been associated with low stacking fault energies, particularly in HEA systems enriched in Co, Ni, and Fe [27]. Since the reduction of Cu and Mn results in a composition enriched in Co, Ni, and Fe it is expected that the stacking fault energy of the non-equiatomic composition is lower than that of the equiatomic composition, thereby contributing to the increased formation of twins observed experimentally [60].

3.3.2 Mechanical behavior

To determine the possible changes in mechanical behavior due to the variation of constituent concentration and the different microstructures characterized above, small scale tensile tests were carried out for each sample. Figure 18 presents representative engineering stress-strain curves for the as-HPT sample and heat treated after HPT sample for both compositions.

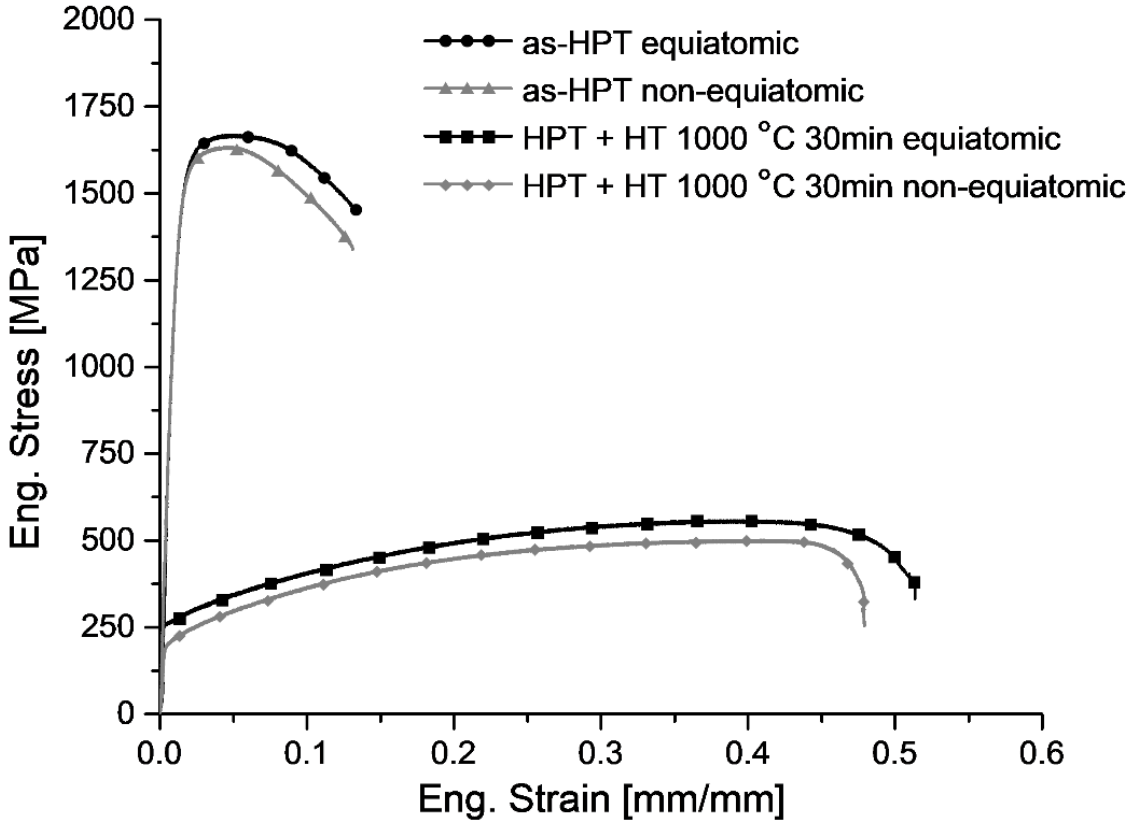

Figure 18. Representative engineering stress-strain curves for the as-HPT samples and heat treated after HPT samples of both the equiatomic and non-equiatomic compositions.

Relevant properties measured from the tensile tests, including yield strength (0.002 mm/mm offset), ultimate tensile strength, strain to failure, and the percent area reduction are summarized in Table 2.

Table 2. Yield strength, ultimate tensile strength, strain at failure, and percent area reduction for all four samples tensile tested.

Sample	Yield Strength [MPa]	Ultimate Tensile Strength [MPa]	Strain at failure [mm/mm]	Area Reduction [%]
Equiatomic as-HPT	1390	1670	13.2	20.3
Non-equiatomic as-HPT	1330	1630	13.1	26.9
Equiatomic HPT + HT	250	560	51.3	66.2
Non-equiatomic HPT + HT	200	500	47.8	81.5

The marked difference between the as-HPT samples of both compositions compared to the heat-treated samples is directly related to the grain size. The as-HPT samples exhibit exceptional yield strength, above 1300 MPa, with limited strain to failure. Most of the strain induced in these samples is associated with local plasticity, after the ultimate tensile strength is reached. These behaviors are common to nanocrystalline metals due to the Hall-Petch strengthening and inability to accommodate large dislocation densities [57]. The heat-treated samples possess significantly lower yield strengths, on the order of 200 MPa, with a large increase in ductility. Moreover, the heat-treated samples demonstrate strain hardening from their yield point to the ultimate tensile

strength. The grain growth that occurred during the heat treatment produced a coarse enough grain structure to accommodate dislocation entanglement within the FCC matrix leading to this observed change in mechanical behavior. Differences in the failure mode of the two processing steps can be appreciated by observing the fracture surfaces captured in the SE SEM micrographs of Figure 19.

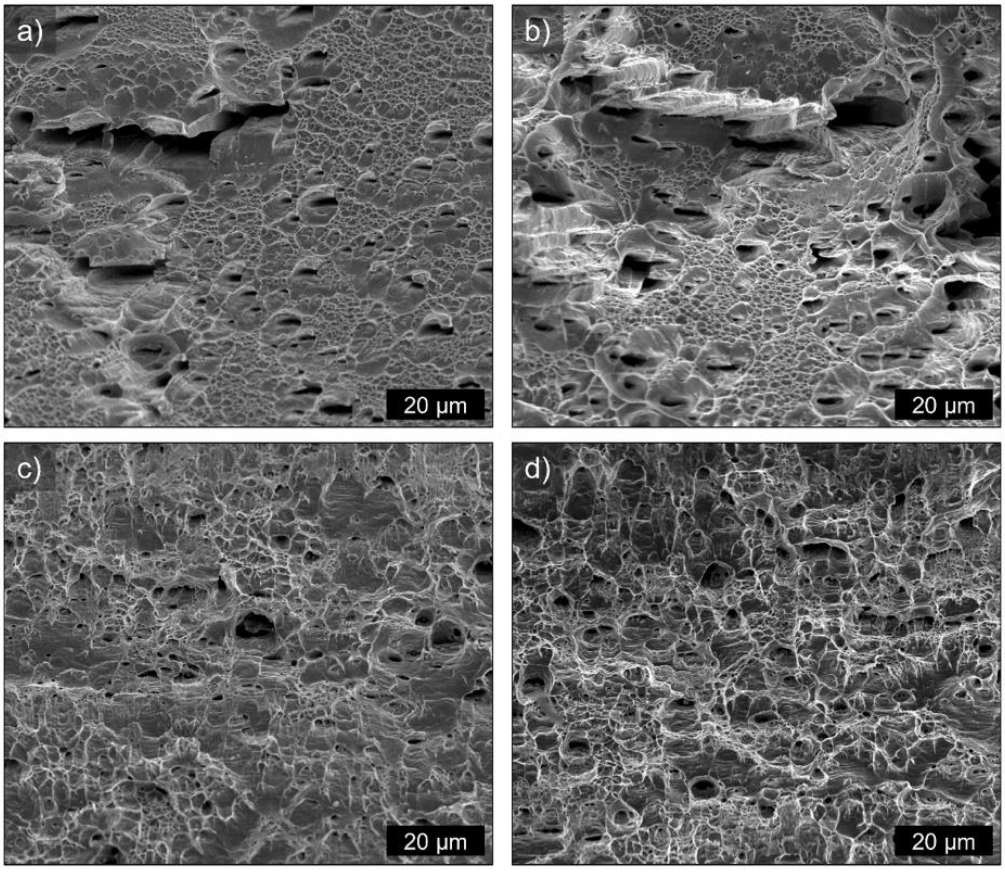

Figure 19. SE micrographs showing the fracture surfaces topography of (a) the as-HPT equiatomic composition, (b) the as-HPT non-equiatomic composition, (c) the heat treated after HPT equiatomic composition, and (d) the heat treated after HPT non-equiatomic composition.

The fracture surfaces of the as-HPT samples possess fine scale dimpled regions corresponding to ductile failure, along with the formation of large-scale voids that have faceted features corresponding to the radial direction of the HPT disc orientation. The fine grain size and the directionality of the strain induced during HPT are expected to contribute to this failure mode.

In comparison the heat-treated samples exhibit uniform dimpled surfaces with fine void formation demonstrating the obvious ductile failure.

The results of the tensile testing of these two compositions illustrate two potential influences of the constituent concentration in this alloy system, specifically the role of Cu and Mn. After each processing step, the yield strength of the equiatomic composition is consistently higher than that of the non-equiatomic composition by roughly 50 MPa. While the exact mechanisms of solid solution strengthening are more difficult to realize for HEAs as compared to conventional alloys, it is anticipated that Cu and Mn contribute to the solid solution strengthening in this alloy system as they could provide the most significant lattice distortion due to their atomic size. Another difference between the equiatomic composition and non-equiatomic composition is that the area reduction that occurs during the tensile test is greater for the non-equiatomic composition under both processing conditions. This could correspond to the difference in the deformation mechanisms active in the two compositions. From the microstructural analysis, the non-equiatomic composition possesses more twins than the equiatomic composition so it is possible that the reduction of Cu and Mn allows for more deformation twinning to occur in the material. While the influence of the constituent variation is minor compared to the effect of microstructure, the contributions of Cu and Mn to solid solution strengthening and deformation behavior are appreciable.

3.4 Summary

Cu and Mn influence the mechanical behavior and thermal stability of the CoCuFeMnNi alloy system. By experimentally forming and processing by HPT the equiatomic composition of this alloy system along with the non-equiatomic composition with reduced content of Cu and Mn, the differences in their behavior are associated to the different contents of Cu and Mn. The non-

equiatomic composition exhibited slightly larger grains than the equiatomic after heat treatment which is attributed to the ability of both Cu and Mn to slow grain growth kinetics. More twinning occurred in the non-equiatomic meaning the reduction of Cu and Mn may have also lowered the stacking fault energy of the alloy. This role may also contribute to the different deformation mechanisms active during tensile loading. The equiatomic composition achieved higher strengths at both the as-HPT state and the heat-treated state, showing the role of Cu and Mn in solid solution strengthening due to their large atomic size compared to the other constituents. From the current study, Cu and Mn are identified to impact the performance of HEAs within the CoCuFeMnNi system.

Chapter 4 : Influence of phase decomposition on mechanical behavior in a nanocrystalline non-equiatomic CoCuFeMnNi high entropy alloy

4.1. Background

With the differences between the equiatomic and non-equiatomic CoCuFeMnNi HEAs in the single FCC phase state established in the previous chapter, the focus of this study shifts to the phase stability of the non-equiatomic composition at intermediate temperatures. The current understanding of HEAs is that the selection of constituent elements and their relative amounts is paramount to the performance of the alloy. The largest subset of HEAs is based on the use of 3d-transition metals to stabilize a major face centered cubic (FCC) phase. This technique dates back to one of the earliest reported compositions, the equiatomic composition of CoCrFeMnNi also known as the Cantor alloy [7]. The Cantor alloy is representative of the initial premise of HEA research because these five elements in an equiatomic composition produce a single FCC crystalline phase, after conventional casting. In this FCC phase, each constituent element has an equal probability of occupying any given lattice site. Since its discovery, the Cantor alloy has been thoroughly studied for its unique fracture toughness at room temperature and cryogenic temperature, attributable to the relatively low stacking fault energy and high shear modulus promoting nano twinning and large separation of partial dislocations [25,31,61]. While the alloy exhibits these properties in the single phase state, phase decomposition is observed in the Cantor alloy after heating at intermediate temperatures which can significantly alter the mechanical behavior of the alloy [2,26,32]. Recent research in the 3d-transition metal subset of HEAs has focused on the development of HEAs that exhibit targeted multi-phase microstructures to improve mechanical behavior for engineering applications [49,62]. Often these studies rely on specialized processing of the material such as severe plastic deformation, including high pressure torsion

(HPT), along with post deformation annealing heat treatments to form secondary phases in the microstructure [50–52,63].

Similar to the Cantor alloy, another well studied FCC based HEA exhibiting phase decomposition is the equiatomic CoCuFeMnNi composition [40–43,64]. Early reports on this alloy document varying observations of phase stability and secondary phase formation [40,42]. Recently the authors of the current study published a systematic investigation of the phase decomposition in the equiatomic CoCuFeMnNi to detail precisely what secondary phases form, how thermally stable they are, and how they contribute to the mechanical behavior of the material [64]. To achieve this, results of systematic heat treatments on experimentally formed samples were compared to the predictions from CALculated PHAse Diagram (CALPHAD) method, which is a computational thermodynamics technique that has recently been modified for application to HEA research [6,5,65,66]. From this work CALPHAD analysis of the equiatomic CoCuFeMnNi was validated by experimental results, determining the alloy exhibits a secondary Cu-rich FCC phase below 900 °C as well as an ordered B2 body centered cubic (BCC) phase enriched in Fe and Co stable below 800 °C. The B2 phase exhibited uniform precipitation in the FCC matrix and contributed to the strength of the material while the Cu-rich FCC phase was irregularly distributed and primarily driven by segregation of Cu due to the immiscibility of Cu with the other constituents. The phase formation in the equiatomic CoCuFeMnNi is fairly complex and so there is a possibility of varying the composition of the alloy within the CoCuFeMnNi system to control the secondary phase formation in a non-equiatomic composition.

Based on the above discussion, the objectives of the current study are, first, to probe the non-equiatomic compositional space of the CoCuFeMnNi system using CALPHAD to minimize Cu segregation at intermediate temperatures. Second, to experimentally prepare the alloy using

HPT to achieve a nanocrystalline microstructure and conduct thermal analysis and heat treat accordingly to investigate the phase stability in this non-equiatomic composition. Finally, we assess the mechanical behavior of various microstructural features from grain size to phase constituents.

4.2. Experimental methods

4.2.1. Computational thermodynamics

Thermodynamic calculations of phase stability were produced by the CALPHAD approach using ThermoCalc software with the high entropy alloy database version three "TCHEA3" [67]. Recently the fraction of assessed ternaries (FAT) has been proposed as an effective metric in comparing the application of TCHEA3 to specific HEA systems [68]. The CoCuFeMnNi HEA system possesses a FAT of 0.8, meaning eight of the ten possible ternaries were assessed within the current version of the database.

4.2.2. Material preparation

A cast ingot of the non-equiatomic $Co_{26}Cu_{10}Fe_{27}Mn_{10}Ni_{27}$ at.% was experimentally synthesized by induction levitation melting of feedstock material with purity >99.7%. The casting occurred in an Ar inert environment and the material was initially cast into a Cu crucible. To achieve chemical uniformity in the resulting ingot, the material was flipped, rotated, and remelted four times. Upon the final melting, the material was cast into a stainless steel die. The resulting ingot was machined to remove any contamination from the die. Wire electric discharge machining (EDM) was implemented to prepare discs of the as-cast material for subsequent processing. The discs with radius of 7.5 mm and thickness of 0.8 mm were sectioned from the mid-radius position of the ingot to avoid the high porosity commonly found in the center of cylindrical ingots. The discs were then mechanically polished to remove any contaminants from EDM and encapsulated

under Ar purged vacuum in fused quartz ampules. After encapsulation, the discs were homogenized at 1100 °C for 12 hours followed by a water quench. The homogenized discs were then processed by HPT to impart severe plastic deformation. The fundamentals of the HPT process have been published in reference [56]. In this study the HPT process was conducted at room temperature with a pressure of 4 GPa with an anvil rotational speed of 0.5 rpm. Each disc was processed for four turns of the anvil. Post deformation annealing (PDA) treatments of the as-HPT material were carried out by first encapsulating the samples as described above and heat treating at 600 °C and 1000 °C for 30 minutes followed by a water quench. Due to the nature of torsional strain developed through HPT, the relative level of strain and microstructural refinement achieved through the process is highly location specific along the radius of the disc. To address this, all samples for analysis were taken from the mid radius position.

4.2.3. Differential scanning calorimetry

Thermal analysis of the as-homogenized and as-HPT material was conducted by differential scanning calorimetry (DSC) with a Netzsch DSC 403 F3 Pegasus® [69]. Samples with approximate dimensions of 2 mm × 0.5 mm × 2 mm were sectioned using EDM from the mid-radius location of both homogenized and as-HPT discs and mechanically polished to remove contaminants. Each sample was placed in alumina crucibles and heated in the DSC under an inert Ar environment from 25 °C to 1470 °C with a heating rate of 10 °C/min.

4.2.4. Microstructural characterization

A Rigaku SmartLab X-ray diffractometer (XRD) equipped with a Cu K_α ($\lambda = 0.1542$ nm) radiation source measured the X-ray diffraction patterns of each sample. Each sample was scanned from 20° to 100° with a step size of 0.02° and a speed of 2 steps per second. The intensity data of

each sample was normalized for comparison. The lattice parameter of the identified phases from each XRD pattern was calculated using the Nelson-Riley extrapolation method [58].

A FEI Quanta 3D field emission gun scanning electron microscope (SEM) equipped with a pole piece mounted backscatter electron (BSE) detector was utilized for preliminary microstructural observation. All SEM micrographs are normal to the face of the disc. All samples were mechanically polished followed by a final vibratory polishing using alumina polishing suspension.

Automated crystal orientation mapping (ACOM) was performed on the as-HPT sample and PDA treated at 600 °C for 30 minutes. A Tecnai F-20 ST TEM operated at 200 kV, equipped with ASTAR NanoMegas system was used for precession electron diffraction (PED). TEM was operated in microprobe scanning transmission electron microscopy (μP-STEM) mode with an extraction voltage of 4.5 kV, a condenser aperture (C2) of 30 μm, a gun lens 3, a spot size 6, and a camera length of 80mm. Each map was acquired using a step size of 2 nm and a precession angle of 0.4 ° at each step.

After the acquisition, the data was analyzed using ASTAR package (Diff Gen2, Index2, MapViewer2) for indexing the spot diffraction pattern using the template matching procedure. The simulated diffraction patterns were given the lattice parameter as 3.6 Å for FCC phase and 2.86 Å for B2 phase as determined by the analysis of each samples XRD pattern as described above. The indexing was performed using one softening loop, three spot enhance loops, a spot detection radius of, 5 and a noise threshold of 10. Post processing of the orientation information and the calculation of grain sizes was performed using MTEX version 3.5.0 in MATLAB 2015a. Additional information on the elliptical fit method of grain size measurement is found in reference [70].

The energy dispersive X-ray spectroscopy (EDS) was done in STEM mode with condenser aperture (C2) of 50 μm and a spot size 5. The quantified measurement of composition for the two phases present in the HPT and post deformation annealing heat treated at 600 °C for 30 minutes sample were generated from point analysis of the STEM EDS maps.

4.2.5. Mechanical testing

Tensile tests were performed using an Instron E 3000 Electropuls® universal testing machine equipped with a 5 kN load cell and a video extensometer to resolve axial strain. Each tensile specimen was prepared by EDM with a 2 mm gauge length, 1 mm width and 0.5 mm thickness gauge section. To ensure the tensile specimen were comparable between samples, all coupons were cut such that the center of the gauge width aligned with the mid-radius position in the disc. The tensile direction is normal to the radial direction of the disc and the thickness of the coupon corresponds to the thickness of the disc. All tests were conducted with a nominal strain rate of $1x10^{-3}$ s^{-1}. Representative stress-strain curves are presented from the several coupons that were tested for each sample.

4.3. Results

4.3.1. Microstructural analysis of as-homogenized and as-HPT state

XRD and SEM analysis confirms a fully homogenized microstructure in the starting material prior to HPT. Figure 20 (a) contains the XRD pattern for the as-homogenized material, which is indexed to a single FCC pattern. The BSE micrograph presented in Figure 20 (b) presents the microstructure of the as-homogenized material through channeling contrast to resolve the equiaxed grain structure of the single FCC phase. The grains of the as-homogenized material are relatively coarse, with an average Feret diameter of 115 ± 31 μm. The darkest contrast in the BSE micrograph of Figure 20 (b) are pores in the as-homogenized material that are remaining from the

casting process. The material produced through the homogenization heat treatment exhibits a sufficiently uniform microstructure of a single FCC phase with coarse grains to accommodate strain during severe plastic deformation.

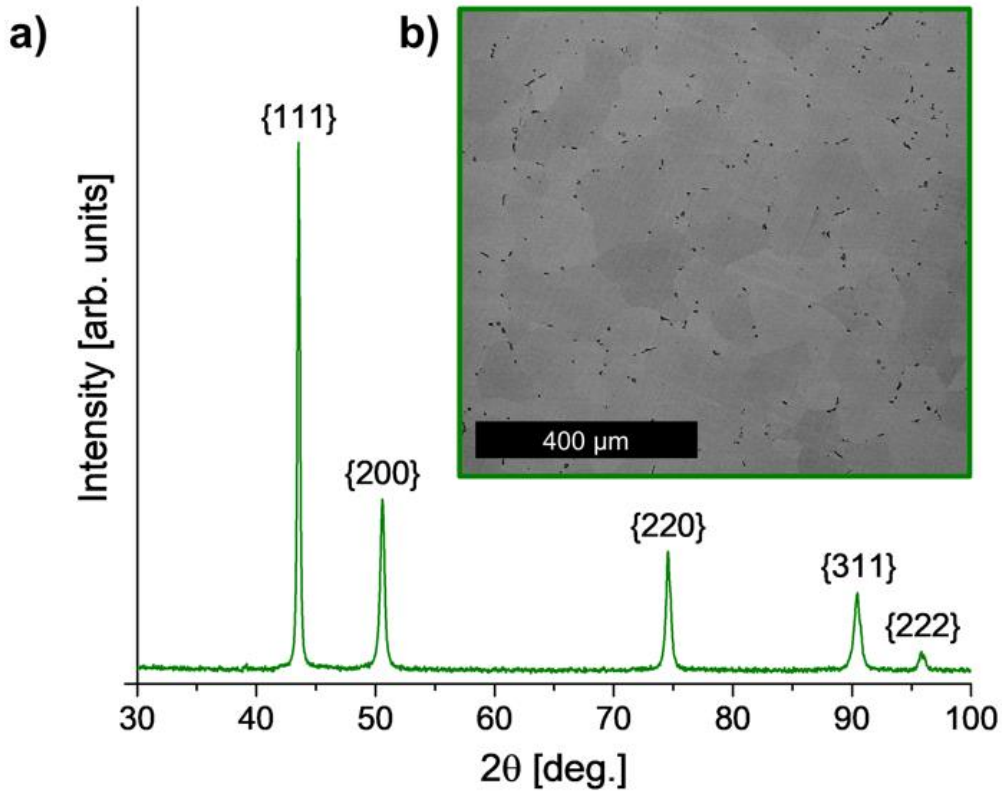

Figure 20. (a) XRD pattern of the as-homogenized $Co_{26}Cu_{10}Fe_{27}Mn_{10}Ni_{27}$ at.% HEA indexed to a single FCC phase (b) SEM BSE micrograph of the as-homogenized microstructure.

The level of strain introduced into the as-homogenized material through the HPT processing parameters is commonly expected to produce a nanocrystalline microstructure in similar FCC metals and alloys [71–73]. Therefore, the microstructural analysis of the as-HPT material was conducted by TEM techniques including ACOM and STEM EDS found in Figure 21 (a) and (b) are the ACOM texture map and phase map, respectively, for the as-HPT material. After HPT, the microstructure achieves a highly refined microstructure while maintaining a single FCC phase. The average grain size of the as-HPT material is 100.4 ± 2 nm and the accompanying grain

size distribution is presented in Figure 21 (c). The grains are significantly elongated with an aspect ratio of 3.34:1, which is inherent to the torsional nature of the strain applied to the samples. The chemical uniformity of the nanocrystalline FCC phase is confirmed by STEM EDS, found in Figure 21 (d), which shows no appreciable clustering of any of the constituents over a relatively broad area of the microstructure. Based on the above analysis, the HPT process successfully nanostructured the previously coarse grain FCC phase of the as-homogenized starting material.

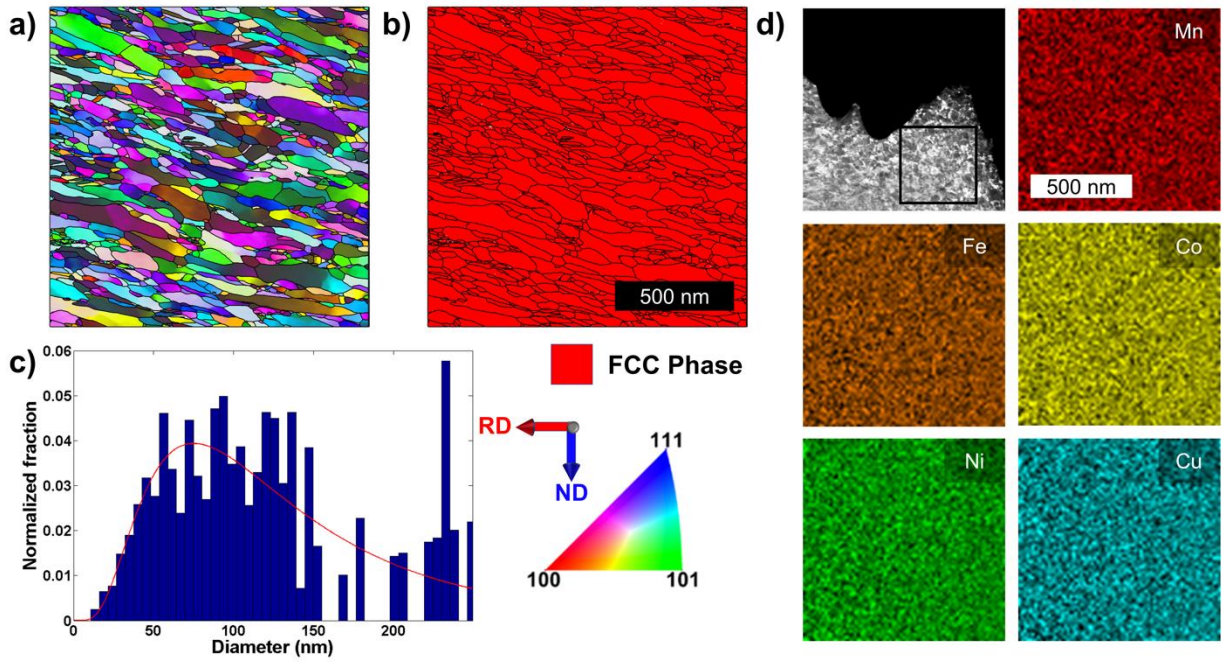

Figure 21. TEM analysis of the as-HPT microstructure including (a) automated crystal orientation mapping (ACOM) texture map, (b) ACOM phase map indexing the entire microstructure to the FCC matrix phase, (c) elliptical fit grain size distribution, and (d) STEM EDS compositional map.

4.3.2. Thermodynamic calculations and thermal analysis

The equilibrium step diagram produced by thermodynamic calculations using the CALPHAD method for the non-equiatomic $Co_{26}Cu_{10}Fe_{27}Mn_{10}Ni_{27}$ at.% HEA is presented in Figure 22 (a). Equilibrium step diagrams plot the relative amount of all phases as a function of temperature and are effective in mapping the predicted phase stability for a given composition.

CALPHAD predicts a melting range for the primary FCC matrix phase of the HEA from roughly 1295 °C to 1370 °C. In the solid state, CALPHAD predicts a broad single-phase region from melting to roughly 630 °C, below which secondary phases are predicted. Below 630 °C a B2 ordered BCC precipitate enriched in Fe-Co is predicted to readily form; at 400 °C the equilibrium amount of B2 predicted is nearly 50%. Below 535 °C, a Cu-rich FCC is predicted to form but with a significantly lower equilibrium amount of all phases. The phase stability predicted by CALPHAD will serve as a point of comparison for the following experimental results of thermal and microstructural analysis of the $Co_{26}Cu_{10}Fe_{27}Mn_{10}Ni_{27}$ at.% HEA.

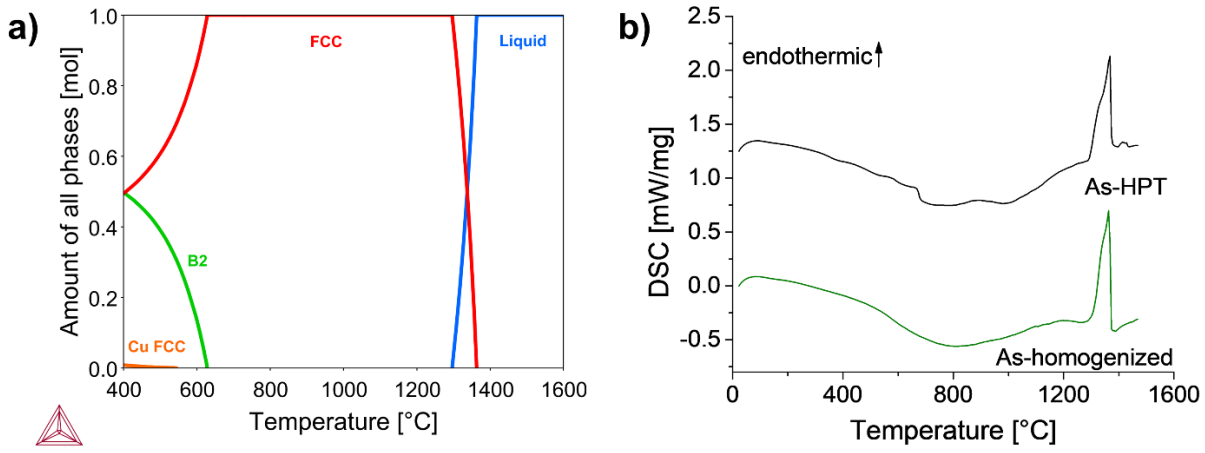

Figure 22. (a) CALPHAD step diagram of the designed $Co_{26}Cu_{10}Fe_{27}Mn_{10}Ni_{27}$ at.% composition mapping the equilibrium phases and their relative amount as a function of temperature and (b) differential scanning calorimetry curves for the coarse grain as-homogenized sample and the nanostructured as-HPT sample.

DSC curves of the as-homogenized and as-HPT $Co_{26}Cu_{10}Fe_{27}Mn_{10}Ni_{27}$ at.% HEA are plotted in Figure 22 (b), which provide context for the two PDA treatment temperatures investigated. While each sample exhibits a broadly curving background inherent to the DSC, several observations are apparent when comparing the coarse grained as-homogenized sample and the nanocrystalline as-HPT sample. Both samples possess a sharp endothermic peak corresponding

to the melting event from 1293 °C to 1378 °C with a peak intensity at 1368 °C. In the solid state prior to the melting event, the as-HPT sample exhibits several minor fluctuations from the background curvature that are not present in the as-homogenized sample. In the as-HPT sample from 253 °C to 688 °C several minor fluctuations are apparent with the largest peaking at 668 °C. In addition to these lower temperature fluctuations, a larger fluctuation is present from 793 °C to 988 °C with a peak intensity at 893 °C. When considering the predictions from CALPHAD, the fluctuations present in the DSC curves of the as-HPT sample may be attributable to the precipitation behavior of the B2 phase, with the lower temperature fluctuations relating to precipitation and the larger fluctuation at higher temperature relating to dissolution. To test this hypothesis, PDA treatments were conducted at 600 °C for 30 min to capture the precipitation event, and at 1000 °C to confirm complete dissolution.

4.3.3. Microstructural analysis of the post deformation heat treatments

Selected from the above thermal analysis of the as-HPT material two 30-minute PDA treatments were conducted at 600 °C and 1000 °C to investigate the phase stability in this $Co_{26}Cu_{10}Fe_{27}Mn_{10}Ni_{27}$ at.% HEA. The following details the microstructural analysis of these two heat treated samples to establish the phase stability of this material and quantitatively compare it to the CALPHAD predictions for this HEA composition.

Figure 23 (a) shows the XRD patterns of the two post deformation heat treated materials as well as the as-HPT material for reference. As confirmed by the TEM results of Figure 21, the as-HPT XRD pattern exhibits a single FCC pattern with broad peaks indicative of a refined grain structure [74]. The lattice parameter of the FCC phase is 3.60 Å, as calculated from this XRD pattern. After heat treatment at 600 °C for 30 minutes, the material develops secondary peaks in

addition to the FCC pattern that index to a BCC structure with a lattice parameter of 2.86 Å. The BSE micrograph in Figure 23 (b) shows Z contrast that reveals nano-sized precipitates with darker contrast than the matrix phase. After PDA treatment at 1000 °C for 30 minutes, the XRD pattern returns to a single FCC pattern with no secondary peaks. The microstructure presented in the BSE micrograph of Figure 23 (c) possesses an equiaxed grain structure of the single FCC phase with an average Feret diameter of 30 ± 13 μm. This analysis suggests that there is a clear phase decomposition that occurs during the PDA treatment at 600 °C for 30 minutes which does not occur at high temperature, specifically 1000 °C.

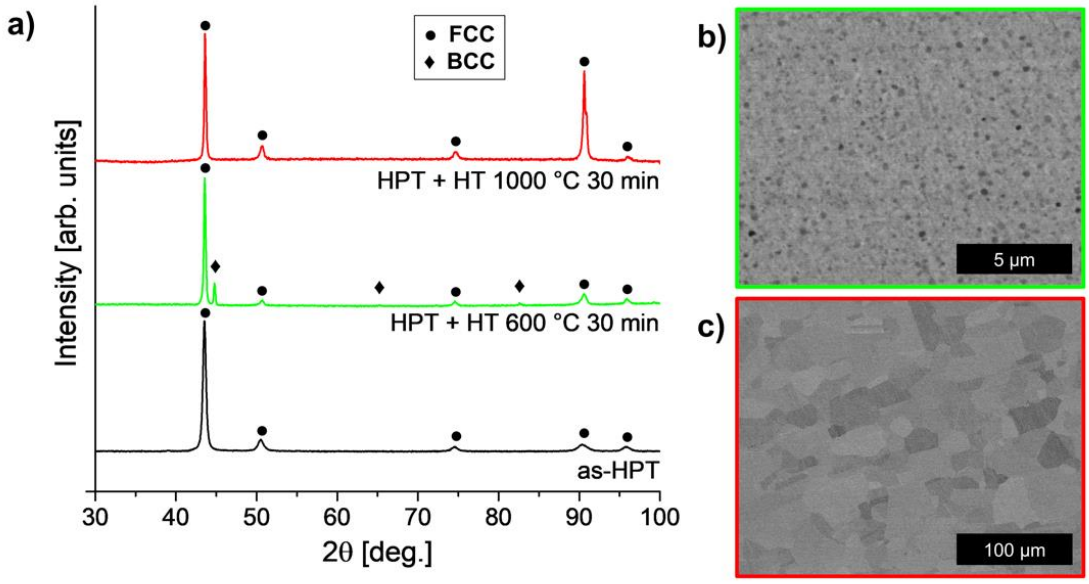

Figure 23. (a) XRD patterns of the as-HPT, HPT and heat treated at 600 °C for 30 min, and HPT and heat treated at 1000 °C for 30 min; (b) BSE SEM micrograph of the HPT and heat treated at 600 °C for 30 min sample; and (c) BSE SEM micrograph of the HPT and heat treated at 1000 °C for 30 min sample.

TEM analysis of the PDA treated material at 600 °C for 30 minutes is required to fully characterized the phase decomposition. Figure 24 (a) and (b) are texture and phase maps, respectively, from ACOM analysis of the material after PDA treatment at 600 °C for 30 minutes.

The material exhibits a two phase microstructure with a major FCC phase, with 91.2 vol%, and a minor B2 ordered BCC phase, with 8.8 vol%. The minor B2 phase exhibits intergranular precipitation with no indexing to the B2 phase within the major FCC phase. Figure 24 (c) and (d) plot the grain size distribution for the FCC and B2 phases, respectively. The size of the two phases is on the same order of magnitude with the FCC phase possessing an average grain size of 146 ± 2 nm and the B2 phase an average grain size of 131 ± 13 nm. Additionally, both phases in this aggregate microstructure exhibit a near equiaxed grain size; the aspect ratio of the FCC phase is 1.76:1 while the B2 phase is 1.71:1. Through this detailed TEM analysis of the material after PDA treatment at 600 °C for 30 minutes, the phase decomposition from the as-HPT single FCC phase is confirmed to form a secondary minor B2 Phase.

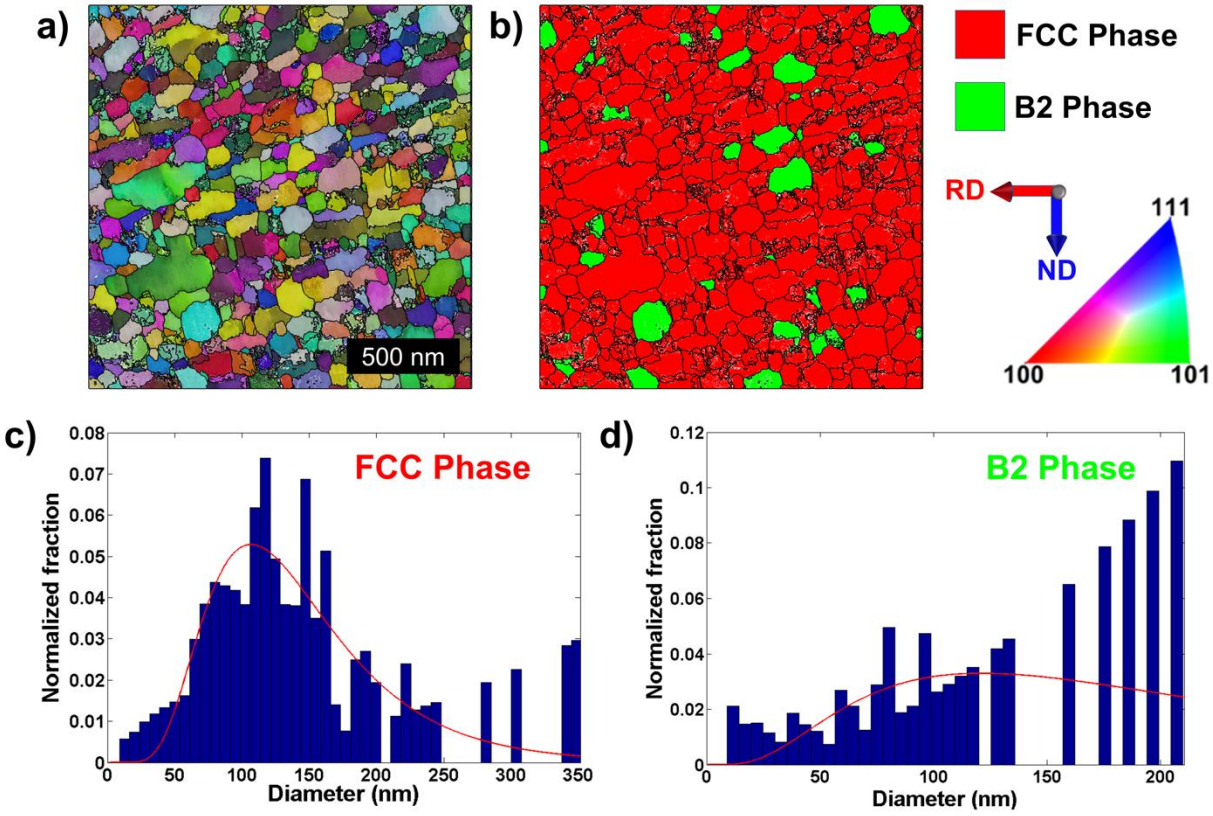

Figure 24. TEM analysis of the HPT and heat treated at 600 °C for 30 min microstructure including (a) ACOM texture map, (b) ACOM phase map indexing the FCC matrix phase and B2 precipitates, (c) elliptical fit grain size distribution of the matrix FCC phase, and (d) elliptical fit grain size distribution of the precipitate B2 phase.

To elucidate the chemical composition of the two phases present in the material after PDA treatment at 600 °C for 30 minutes, STEM EDS mapping was utilized as shown in Figure 25 (a). The elemental maps of STEM EDS show a significant enrichment of Fe and Co to the B2 secondary phase. A majority of the FCC phase exhibits a uniform chemistry near the bulk designed composition of the $Co_{26}Cu_{10}Fe_{27}Mn_{10}Ni_{27}$ at.% HEA with the exception of fine nano-sized domains of Cu segregation. These Cu-rich domains occur throughout the FCC phase as indexed by ACOM. Point analysis of the chemical composition from STEM EDS of the Cu-rich domains, produces a local composition of 23.6 ± 2.8 Co, 22.6 ± 3.5 Cu, 22.5 ± 3.1 Fe, 8.1 ± 1.3 Mn, and

23.2 ± 2.6 Ni at.%. Since the CALPHAD predictions of this HEA predicts only the major FCC and B2 phase are stable at equilibrium at 600 °C, the point analysis of the major FCC phase as well as the B2 phase are plotted against the predicted composition of the two phases from CALPHAD in Figure 25 (b) and (c). From this comparison of the experimentally measured composition and CALPHAD prediction, the composition of both the major FCC phase and minor B2 phase after PDA treatment at 600 °C for 30 minutes are in good agreement with the compositions predicted for this HEA at equilibrium at 600 °C.

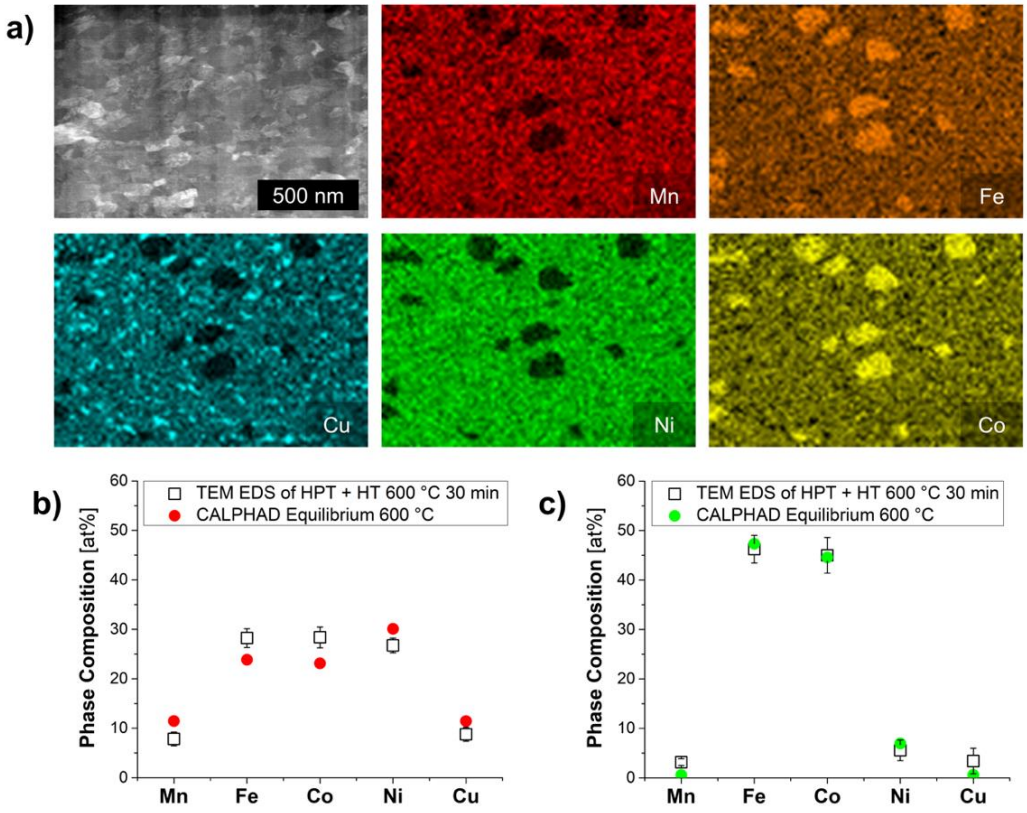

Figure 25. (a) STEM EDS compositional map the HPT and heat treated at 600 °C for 30 min microstructure, and a comparison of phase composition experimentally measured from STEM EDS of the HPT and heat treated at 600 °C for 30 min sample to the predicted composition from equilibrium CALPHAD calculations for the alloy at 600 °C for (b) the matrix FCC phase, and (c) the B2 phase.

4.3.4. Tensile properties

To assess the mechanical properties of the samples after HPT and PDA treatment, several tensile tests were conducted for each sample. Representative engineering stress-strain curves of the as-HPT, HPT and PDA treated at 600 °C for 30 minutes, and HPT and PDA treated at 1000 °C for 30 minutes samples are presented in Figure 26 (a).

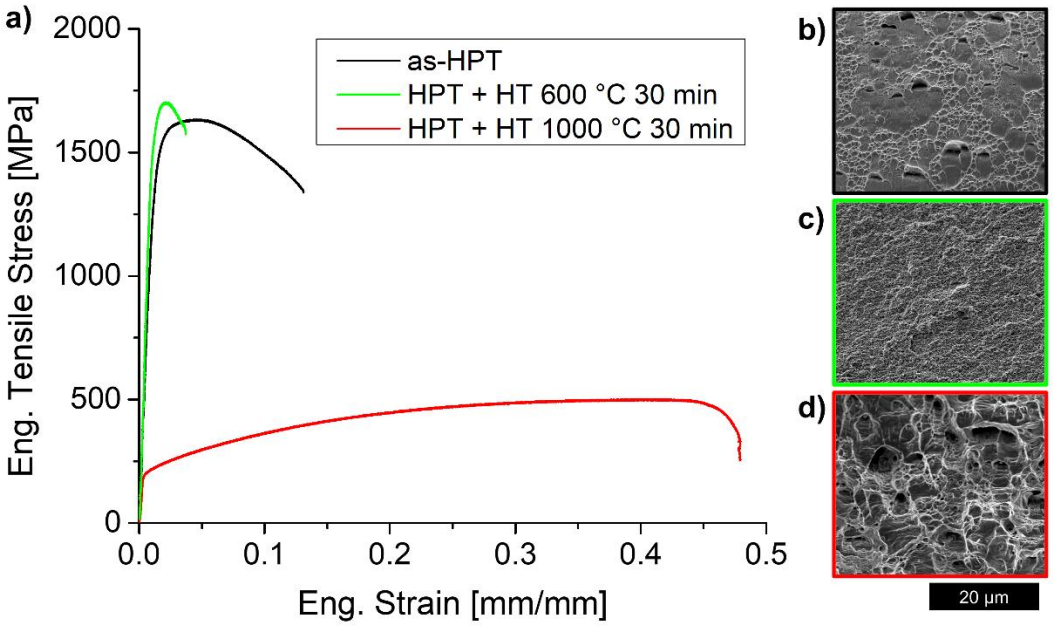

Figure 26. (a) Engineering stress-strain curves representative of the as-HPT sample, the HPT and heat treated at 600 °C for 30 min sample, and the HPT and heat treated at 1000 °C for 30 min sample; (b) fracture surface of the as-HPT sample exhibiting regions of ductile cup and cone topology and regions of cleaved fracture; (c) fracture surface of the HPT and heat treated at 600 °C for 30 min sample exhibiting finer cup and cone topology; (d) fracture surface of the HPT and heat treated at 1000 °C for 30 min sample exhibiting coarse uniform cup and cone topology.

Quantified measurements from these stress-strain curves and fracture analysis are presented in Table 3. The as-HPT material possesses a high yield strength of 1.38 GPa and a peak ultimate tensile strength (UTS) of 1.63 GPa. The as-HPT sample has significant strain at failure over 0.10 mm/mm with a relatively large area reduction of 35%. Figure 26 (b) contains a SE micrograph capturing the fracture surface of the as-HPT material, which exhibits a mixture of

regions of cup and cone topology and regions of cleaved topology. After PDA treatment at 600 °C for 30 minutes, the material achieves a higher yield strength and UTS as compared to the as-HPT material at 1.52 GPa and 1.70 GPa respectively. The material has reduced but appreciable strain at failure of 0.04 mm/mm and effectively 0% area reduction at the fracture surface. Figure 26 (c) presents the SE micrograph of the fracture surface from the material PDA treated at 600 °C for 30 minutes with a uniform cup and cone topology that is finer than the sample regions in the as-HPT material. Finally, after PDA treatment at 1000 °C for 30 minutes, the mechanical properties of the material are significantly different than the other two material states. The yield strength and UTS of the material after the higher temperature PDA treatment, decreased to 200 MPa and 500 MPa respectively and the strain at failure increased to 0.478 mm/mm with 81.5% area reduction at the fracture surface. The fracture surface of this material is captured in the SE micrograph of Figure 26 (d). The cup and cone topology of the fracture surface is significantly coarser than the other two material states. The mechanical properties are markedly different at each material state with a trend of high strength and minimal plasticity in the as-HPT state, hardening and embrittlement after lower temperature PDA treatments, and extreme softening after higher temperature PDA treatments.

Table 3. Mechanical properties of the as-HPT sample, the HPT and heat treated at 600 °C for 30 min sample, and the HPT and heat treated at 1000 °C for 30 min sample measured from the engineering stress-strain curves in Figure 26.

Sample	Elastic Modulus [GPa]	Yield Strength [MPa]	Ultimate Tensile Strength [MPa]	Strain at UTS [mm/mm]	Strain at failure [mm/mm]	Area Reduction [%]
As-HPT	127	1380	1630	0.05	0.13	35
HPT + HT 600 °C 30 min	163	1520	1700	0.02	0.04	~0
HPT + HT 1000 °C 30 min	102	200	500	0.435	0.478	81.5

4.4. Discussion

4.4.1. Phase stability

The step diagram of the $Co_{26}Cu_{10}Fe_{27}Mn_{10}Ni_{27}$ at.% HEA reveals two primary findings. First, it suggests that this non-equiatomic HEA exhibits a similar phase stability as other FCC based HEAs that possess a single FCC phase window at elevated temperatures near the melting point. Second, the results also predict the presence of a precipitation window at intermediate temperatures where secondary phases will form at equilibrium with the FCC matrix phase [64,75]. The resulting microstructure of the as-homogenized material in Figure 20 confirms the stability of the single FCC phase at high temperatures. This single FCC phase was maintained through the HPT process with no indication of a metastable deformation induced transformation occurring in this composition, which has been reported in other FCC based HEAs [76,77]. Comparisons between the CALPHAD step diagram and DSC thermal analysis of the nanocrystalline material exhibit good agreement and serve as an effective technique to investigating phase stability in

HEAs. For both the coarse grain as-homogenized and nano crystalline as-HPT samples, the melting events measured through DSC occur over generally the same temperature range as predicted by CALPHAD. Identifying not only the melting point but also the melting range for a given FCC HEA is important for understanding material properties as well and processability, including castability [78]. The importance of the starting microstructure in DSC thermal analysis is clear when comparing both the coarse grained and nanocrystalline samples in Figure 22 (b). Often in HEA research, studies will conduct DSC analysis on as-cast or coarse grained homogenized samples of the investigated composition, from which the thermal analysis reveals few thermal events related to diffusion limited phase transformations in the solid state [42,79]. When comparing samples of the $Co_{26}Cu_{10}Fe_{27}Mn_{10}Ni_{27}$ at.% HEA with significantly different grain sizes, relatively small fluctuations exist in the nano crystalline sample that are not present in the coarse grained sample. The difference in these samples is attributable to the role of grain boundaries in phase decomposition. In a nanocrystalline material, a high volume of the material is occupied by grain boundaries which act as fast diffusion pathways and preferential nucleation sites for secondary phase due to their relatively high energy landscape compared to the grain interior [63]. Due to the presence of this high volume of grain boundaries, when heated at the same nominal rate, in this study 10 °C/min, the nanocrystalline sample will exhibit more precipitation events than a coarse grain sample, which results in a higher intensity of the DSC signal from a given solid state phase transformation. Considering this role of starting microstructure in the resolution of DSC thermal analysis is critical to the entire field of HEA research when implementing the technique to investigate phase stability.

The resulting microstructures after PDA treatment at 600 °C and 1000 °C support the hypothesis made regarding the identity of the solid state thermal fluctuations of DSC observed in

the nanocrystalline as-HPT sample. Based on the step diagram in Figure 22 (a), the lower temperature fluctuations that peak at 668 °C are expected to correspond to the precipitation of the B2 phase that is predicted to be stable to 630 °C, while the broad fluctuation from 793 °C to 988 °C peaking at 893 °C is attributed to the dissolution of the B2 phase. After PDA treatment of the HPT sample at 600 °C for 30 minutes, the microstructure possesses a significant volume fraction of B2 precipitates that have similar character to the phase predicted by CALPHAD. CALPHAD calculations at 600 °C predict the B2 phase accounts for 13.1% of the microstructure and experimentally from ACOM analysis, after 30 minutes at 600 °C the microstructure is approaching that equilibrium volume fraction at 8.8%. Additionally, as plotted in Figure 25 (b) and (c) the experimental composition of the B2 phase, as well as the matrix FCC, are in good agreement with those predicted from CALPHAD. One aspect of the microstructure that was not well predicted by CALPHAD is the segregation of Cu in the FCC matrix phase after PDA treatment at 600 °C for 30 minutes. It is unclear whether the Cu segregation is an artifact of incomplete equilibration of local chemistry after the formation of the B2 phase or if the stability of the Cu-rich FCC phase is underpredicted in this composition. The Cu-rich FCC phase of the equiatomic CoCuFeMnNi alloy was also found to form at temperatures higher than what CALPHAD predicts, which is consistent with the results reported here [64]. While it is evident that the B2 phase does in fact form during the temperature range that exhibits the thermal fluctuations in DSC, the identity of each fluctuation is not clear at this point. It is speculated that the series of fluctuations at lower temperatures could relate to specific events such as the diffusion of specific constituents and nuclei formation prior to the phase transformation. The identification of these events by in situ TEM is the subject of future work. After PDA treatment of the HPT sample at 1000 °C for 30 minutes, no B2 phase is present within the microstructure which supports the identification of the second broad fluctuation as a

dissolution event. The phase stability predicted from the CALPHAD step diagram for the $Co_{26}Cu_{10}Fe_{27}Mn_{10}Ni_{27}$ at.% HEA presented in Figure 22 (a) is validated by microstructural observations and demonstrates the effectiveness of DSC thermal analysis in probing HEA phase stability with an appropriate starting microstructure.

4.4.2. Mechanical behavior

The elevated strength of the $Co_{26}Cu_{10}Fe_{27}Mn_{10}Ni_{27}$ at.% HEA after HPT is characteristic of FCC metals and HEAs that undergo grain refinement during severe plastic deformation and can be attributed in part to the well-established concept of Hall Petch strengthening [80]. But by tracking the changes in mechanical behavior between the three samples reported in Figure 26 and Table 3, the role of phase decomposition, particularly B2 precipitation, on the mechanical behavior can be elucidated. The as-HPT sample exhibits significant strain at failure and an area reduction of 35% which is indicative of neck formation during deformation that is enabled in nanocrystalline metals by dislocation accommodation as well as grain rotation in the FCC matrix [81]. The as-HPT and PDA treated at 600 °C for 30 minutes sample possess grain sizes on the same order of magnitude, meaning the variations to mechanical behavior between the samples is largely a result of B2 precipitates present after heat treatment as opposed to Hall-Petch softening. The B2 precipitates, which are close in size distribution to the FCC grains in the heat treated sample, contribute a composite strengthening to the overall material. From the tensile behavior, the yield strength and UTS increase with the aggregate addition of B2 precipitates as well as an increase to the stiffness as determined by the calculation of elastic modulus in Table 3. B2 secondary phases are often found to promote strength in FCC matrices due to their BCC crystal structure, which possess less dislocation slip systems than FCC crystals as well as their ordered nature, which can limit dislocation mobility [82]. While the strength increases, the B2 phase leads to significant

embrittlement based on the analysis of the fracture surface and the calculated area reduction of effectively 0%. Along with their inability to accommodate dislocation as FCC crystals do, the distribution of B2 precipitates throughout the material may limit the ability of FCC grains to rotate during deformation, which minimizes the necking ability for the nanocrystalline material. It is possible that further refinement of the PDA treatment parameters can optimize the size and distribution of B2 precipitates to improve the strength ductility balance, but the primary objective of this study was to identify the role of phase decomposition in the nanocrystalline microstructure of the HEA.

4.5. Summary

The phase decomposition of a nanocrystalline $Co_{26}Cu_{10}Fe_{27}Mn_{10}Ni_{27}$ at.% HEA was assessed by DSC thermal analysis and validated CALPHAD thermodynamic predictions of phase stability. The contributions of secondary phase precipitation on the mechanical behavior was determined by tensile tests. The following are key takeaways from this study:

1. The $Co_{26}Cu_{10}Fe_{27}Mn_{10}Ni_{27}$ at.% HEA exhibits a major FCC matrix phase and secondary phase formation of a Fe-Co rich B2 phase and Cu-rich FCC phase at intermediate temperatures.
2. The reduction of Cu and Mn in this equiatomic composition reduces the amount of Cu-rich FCC phase formation as compared to the equiatomic composition, leading to enhanced stability of the B2 phase.
3. CALPHAD predictions of the composition and volume fraction of the FCC matrix and B2 precipitate in the non-equiatomic composition are validated by experimental observations, with the exception of CALPHAD underpredicting the stability of the Cu-rich FCC.

4. DSC thermal analysis of the nanocrystalline material reveals fluctuations related to the precipitation and dissolution of secondary phases that is not observable in the coarse grain as-homogenized material.
5. The addition of the B2 phase to the nanocrystalline microstructure of HEA leads to an appreciable increase in stiffness and strength while inhibiting necking as compared to the single FCC phase in the as-HPT sample.

Chapter 5 : CALPHAD aided prediction of phase stability in the AlMoNbTiZr refractory high entropy alloy system

5.1. Background

Thus far, this dissertation research is focused on the CoCuFeMnNi HEA system which allowed for the investigation of critical aspects of HEA phase stability including the influence of processing, compositional variation and interfaces. This study aims to apply the methodology established above to develop multi-phase microstructures in a refractory HEA. Refractory high entropy alloys (RHEAs) are a subset of HEAs, also known as high entropy alloys, that demonstrate exceptional high strength at temperatures above 1000 °C [16,18,68,83]. Understanding the mechanisms that result in these properties as well as the role of each constituent element in a given RHEA system is critical to the development of these materials for high temperature structural applications. Recent work has established the tendency for RHEAs, that exhibit single BCC structure, with lower valence electron concentrations (VEC) to achieve a more ductile deformation behavior while higher VEC was more likely to deform in a brittle mode [84]. A proposed method for improving the high temperature strength of RHEAs is to develop an alloy with two BCC solid solution phases, one inherently ductile and the other brittle, that can be engineered in such a way that the microstructure consists of a network of the ductile BCC with reinforcing particles of the brittle BCC to strengthen the alloy, which is similar to that in eutectic HEAs [85,86]. Identifying a candidate RHEA system that would achieve such a microstructural concept, requires an effective method for predicting the phase stability in RHEAs. The CALculated PHAse Diagram (CALPHAD) method is a promising prediction tool to explore this space and identify compositions possessing target microstructures [5,65,66]. Due to the uncertainty in current CALPHAD predictions, it is important to validate this method in such complex compositional space with experiment. This study focuses on the CALPHAD guided addition of Al to the equiatomic

MoNbTiZr base alloy in order to establish the feasibility of CALPHAD to predict the phase stability of RHEAs, identify RHEA microstructures with minimal deleterious intermetallic formation, and assess the mechanical behavior of solid solution RHEAs.

5.2. Experimental methods

CALPHAD calculations were conducted using ThermoCalc's TCHEA3 database [6]. The fraction of assessed ternaries (FAT) for the system investigated is 0.33, which is a significant figure of merit established in recent research [68]. Three compositions within the AlMoNbTiZr system were synthesized by arc-melting a mixture of high-purity raw materials under an argon atmosphere. In order to ensure homogeneity, each ingot was flipped and re-melted for at least 5 times. Samples from the cast buttons were produced by electric discharge machining. Two batches of the three RHEAs were made due to compositional deviations in the first batch as reported in the following sections. Detailed chemical analysis for the first batch was conducted using direct current plasma emission spectroscopy (DCPES) by the independent analytical testing laboratory Luvak Laboratories, Inc. All DCPES analysis was conducted to ASTM E1097: standard guide for determination of various elements by direct current plasma atomic emission spectrometry. Heat treatments were conducted on samples at 1500 °C for 12 hr in an argon environment followed by an oil quench. Surfaces of all samples were polished by mechanical polishing ending with a final alumina vibratory polishing. The microstructure of both the as-cast and heat-treated samples were characterized using a Rigaku X-ray diffractometer (XRD) (Cu Kα radiation) and a Field-emission SEM (FEI Quanta3D) equipped with Oxford Instruments EDS and EBSD detectors. For the second batch of samples, two cylindrical micro-pillars with a diameter of ~ 3 μm and a height of ~6 μm were fabricated for each alloy from the polished surfaces using focused ion beam (FIB). In-situ micro-pillar compression was performed at room temperature using a PI85 Picoindenter (Bruker

Inc.), equipped with a 20 μm-diameter flat-top conical tip inside the SEM. In-situ mechanical testing was conducted under displacement control mode at a displacement rate of 10 nm/s, corresponding to a nominal strain rate of 1.6×10^{-3} s^{-1}.

5.3. Results and discussion

5.3.1. CALPHAD prediction of the AlMoNbTiZr system

The base alloy considered in this study is the equiatomic composition of MoNbTiZr. The addition of Mo to the previously studied equiatomic composition of NbTiZr [87] is hypothesized to promote the formation of a secondary BCC phase, enriched in Ti and Zr, that may possess a lower VEC than the primary BCC, which is now enriched in Mo and Nb. CALPHAD predictions of MoNbTiZr confirm this hypothesis be predicting an elevation of the solvus temperature of the secondary BCC. However, a systematic study of additional alloying elements was conducted to identify which would further enhance the stability of the secondary BCC. Miedema's model to calculate the change in mixing enthalpy of two dissimilar elements is used as a metric for the affinity of a given element with the other constituents [39]. These values of mixing enthalpy along with the metallic radius of each element are reported in Table 4. Al was identified as a promising additional alloying element due to its low mixing enthalpy with Ti and Zr.

Table 4. Values of mixing enthalpy ΔHmix [kJ/mol] calculated by Miedema's model for atomic pairs between all constituent elements in the AlMoNbTiZr RHEA system and the atomic radius of each element.

ΔH_{mix} [kJ/mol]	Al	Mo	Nb	Ti	Zr
Al	X	-5	-18	-30	-44
Mo		X	-6	-4	-6
Nb			X	2	6
Ti				X	0
Zr					X
Atomic radius [pm]	143	139	146	147	160

Figure 27 (a) presents the CALPHAD generated equilibrium isopleth diagram, which maps stable phases over a range of temperatures as a function of increasing Al content from MoNbTiZr to AlMoNbTiZr. From this isopleth diagram, a region of single BCC is present at low amount of Al, that represents a potential solutionizing window to achieve a single BCC, labeled BCC1. As Al content increases the stability of BCC2 increases, evident from the positive slope of the green phase line, to a critical concentration of Al at 8 at.% at which the single BCC window is not present. Based on this predicted phase diagram, the addition of Al should promote the secondary phase and segregate to that phase. Another important observation from the isopleth diagram is that as the concentration of Al increases, additional intermetallic phases become stable at elevated temperatures meaning they have a high probability of forming during synthesis and processing at conventional cooling rates. These phases are predicted to be enriched in Al and Zr and exhibit

crystal structures that are generally associated with phases deleterious to the mechanical properties of the alloy due to stress concentration. Accordingly, three compositions were selected to experimentally form and analyze to validate these predictions: equiatomic MoNbTiZr, $Al_4(MoNbTiZr)_{96}$ at.%, and $Al_8(MoNbTiZr)_{92}$ at.%. The equilibrium step diagrams of these three alloys are plotted in Figure 27 (b-d). The three step diagrams show the expected result of increasing Al on the phase formation in these alloys, specifically the increase in stability of the secondary BCC as well as the possible formation of intermetallic phases. These three plots will be compared to the experimental characterization of the three alloys in order to validate the CALPHAD method in terms of the actual composition of the RHEAs.

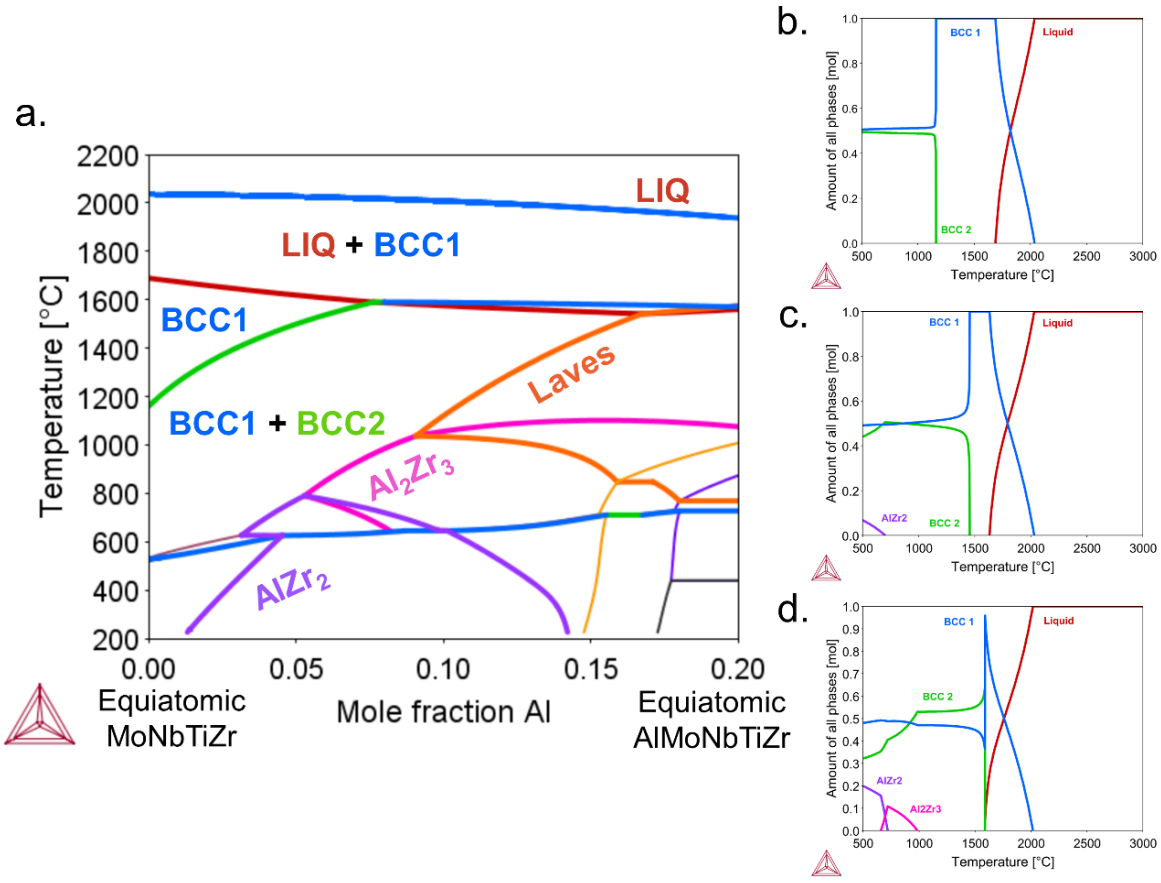

Figure 27. Thermodynamic calculations by the CALPHAD method including (a) an equilibrium isopleth diagram mapping stable phases at a range of temperatures as a function of the addition of Al to the equiatomic MoNbTiZr composition and equilibrium step diagrams plotting the amount of stable phases as a function of temperature for the three compositions studied: (b) equiatomic MoNbTiZr, (c) $Al_4(MoNbTiZr)_{96}$ at.%, and (d) $Al_8(MoNbTiZr)_{92}$ at.%.

5.3.2. First batch compositional deviation and CALPHAD validation

The first batch of candidate alloys systematically deviate from the target composition but offered the opportunity to further validate the application of CALPHAD analysis to the AlMoNbTiZr RHEA system with these experimental results. Table 5 presents the experimental composition of the three materials synthesized in the first batch determined by DCPES. Compared to the target composition all three alloys contain a higher concentration of Mo, but the Al content is generally on target and the ratio of the other constituents is relatively uniform. Oxygen content

in the alloys is below 0.5 at.%, which is low enough to not influence phase formation in the alloy. Recent studies show O has a significant influence on phase formation and mechanical behavior in higher concentrations near 2 at.% [88]. It was eventually determined that the calculation of feedstock material was incorrect and accounted for the Mo enrichment in the first batch of alloys. Nevertheless, the synthesized alloys with detailed chemical analysis offer an additional dataset to validate CALPHAD predictions within the AlMoNbTiZr system. To accomplish this, CALPHAD predictions were recalculated using the exact experimental composition for each alloy accounting for the enriched ratio of Mo with the other constituents.

Table 5. Detailed compositional analysis of the first batch of candidate alloys using DCPES.

First Batch	Al	Mo	Nb	Ti	Zr	O	Trace Metals (Hf, Cu, W, Fe)
Target MoNbTiZr at.%	0	25	25	25	25	0	0
Exp. MoNbTiZr at.%	0	30.4	22.7	23.6	22.5	0.4	0.4
Target $Al_4(MoNbTiZr)_{96}$ at.%	4	24	24	24	24	0	0
Exp. $Al_4(MoNbTiZr)_{96}$ at.%	4.3	30.1	21.8	23.1	22.2	0.3	0.3
Target $Al_8(MoNbTiZr)_{92}$ at.%	8	23	23	23	23	0	0
Exp. $Al_8(MoNbTiZr)_{92}$ at.%	9.8	29.6	21.4	22.2	22.0	0.4	0.4

The recalculated CALPHAD results specific to the experimentally measured compositions are presented in Figure 28. Based on these results, the deviation in the composition of these alloys

by Mo enrichment is predicted to shift the stability of the phases present in the target compositions. Comparing the isopleth calculated for the target compositions and the isopleth of the first batch compositions in Figure 27 (a) and Figure 28 (a), respectively, both exhibit the same high temperature window where a single BCC phase is stable at lower concentrations of Al, along with a region of two BCC phases stable at lower temperatures. For the first batch of alloys, CALPHAD predicts the single BCC window ends near 5 at.% compared to 8 at.% for the target. The step diagrams for each of the three samples made in the first batch found in Figure 28 (b-d) demonstrate how the amount of each phase may deviate from the target. At temperatures where both the BCC phases are present, the high temperature BCC 1 phase is now predicted to be a major phase at equilibrium for all three compositions. This ratio contrasts the target compositions, which exhibited a more equal ratio of the two BCC phases. This change in phase fraction is expected when considering the uniform deviation in the composition of the first batch of alloys to Mo-rich compositions. The high temperature BCC phase predicted by CALPHAD contains the higher melting point elements, so as the amount of Mo is increased this BCC phase becomes a high fraction of the stable phases at equilibrium. Another critical difference between the prediction of the first batch compared to the target compositions is the increased stability of intermetallic phases specifically the laves phase. As previously stated, the design goal of the target compositions was to avoid deleterious intermetallic phases, so the compositions created in the first batch no longer fit this requirement, but the characterization of these microstructures can offer additional validation to the CALPHAD predictions in the AlMoNbTiZr RHEA system. For the three alloys prepared in the first batch, the as-cast microstructures as well as the microstructures after high temperature heat treatments followed by oil quench are characterized in an attempt to validate the CALPHAD predictions of Figure 28.

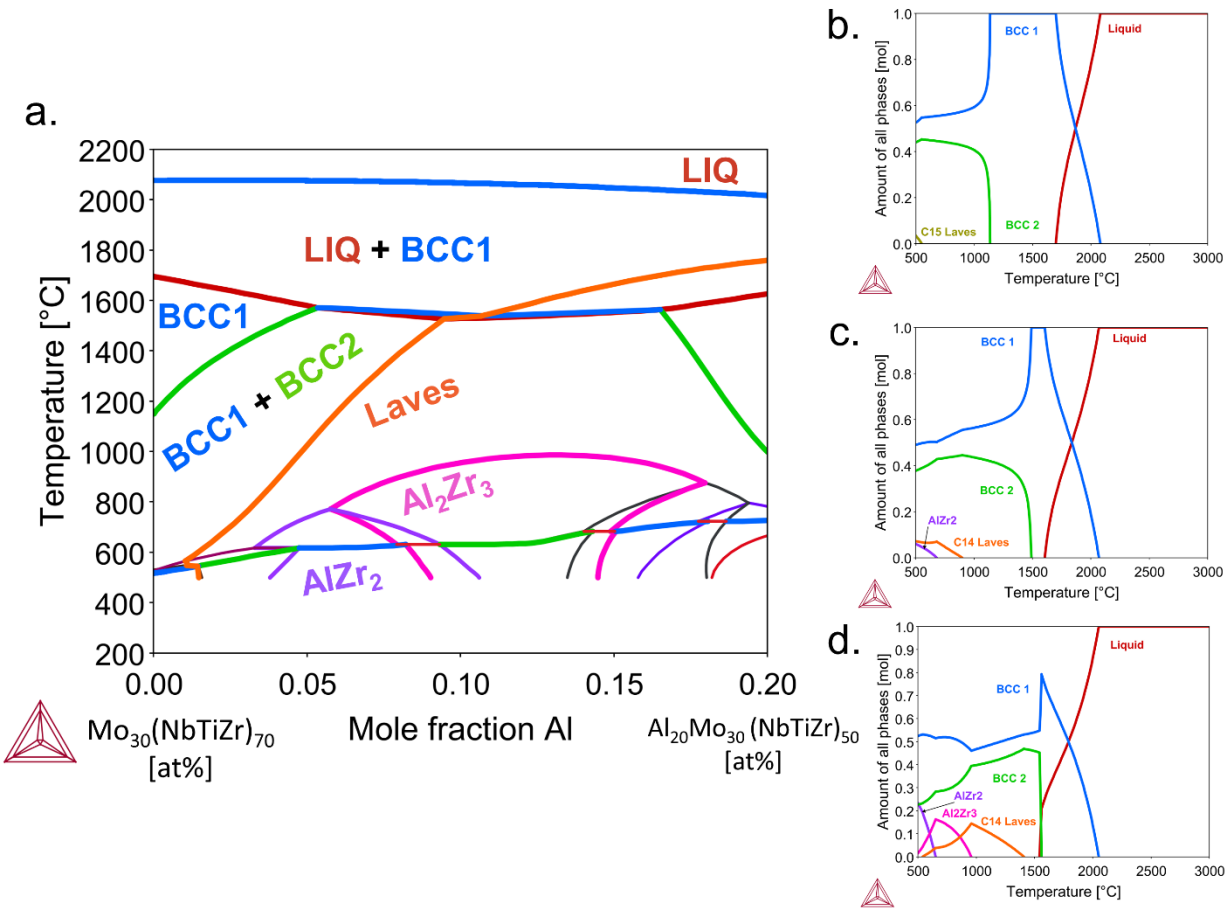

Figure 28. (a) Equilibrium isopleth diagram mapping stable phases at a range of temperatures as a function of the addition of Al to the experimentally determined MoNbTiZr non-equiatomic composition and equilibrium step diagrams plotting the amount of stable phases as a function of temperature for the three compositions formed in the first batch: (b) with no Al, (c) with 4.3 at.% Al, and (d) with 9.8 at.% Al.

Figure 29 presents the microstructural characterization of the alloy with no Al in the as-cast state as well as after heat treatment at 1300 °C for 10 hours and an oil quench, which based on the step diagram for this composition in Figure 28 (b) should be within the single BCC region of phase stability. From the XRD in Figure 29 (a), an appreciable left shoulder is present at lower angles with doublets forming at higher angles in the as-cast state indicates the presence of both BCC phases with no additional intermetallic peaks. SEM EDS in Figure 29 (b) confirms the presence of Mo-rich BCC1 dendrites in the microstructure and the Zr-rich BCC2 present in the

interdendritic region. After ten hours at 1300 °C, the homogenization process has begun but is not complete. Figure 29 (c) shows remaining segregation of Mo and Zr while the overall microstructure has coarsened significantly with fine Mo-rich regions corresponding to the previous dendrite cores, a majority possessing a more uniform distribution of the elements in the space between dendrite and interdendritic regions, and fine Zr-rich regions that correspond to the previous interdendritic region cores. The XRD pattern of the heat treated material in Figure 29 (a) shows a single set of BCC peaks but still exhibiting shoulders on the left side of each peak indicative of a remaining minor secondary BCC. It is expected that conducting the heat treatment at 1300 °C for more than ten hours will lead to a complete homogenization of the microstructure to a single BCC phase as predicted by CALPHAD. Overall, these observations serve to validate the prediction of two distinct BCC phases with no appreciable intermetallic phases after casting, and the possible presence of a single phase region at elevated temperature for this composition within the AlMoNbTiZr RHEA system.

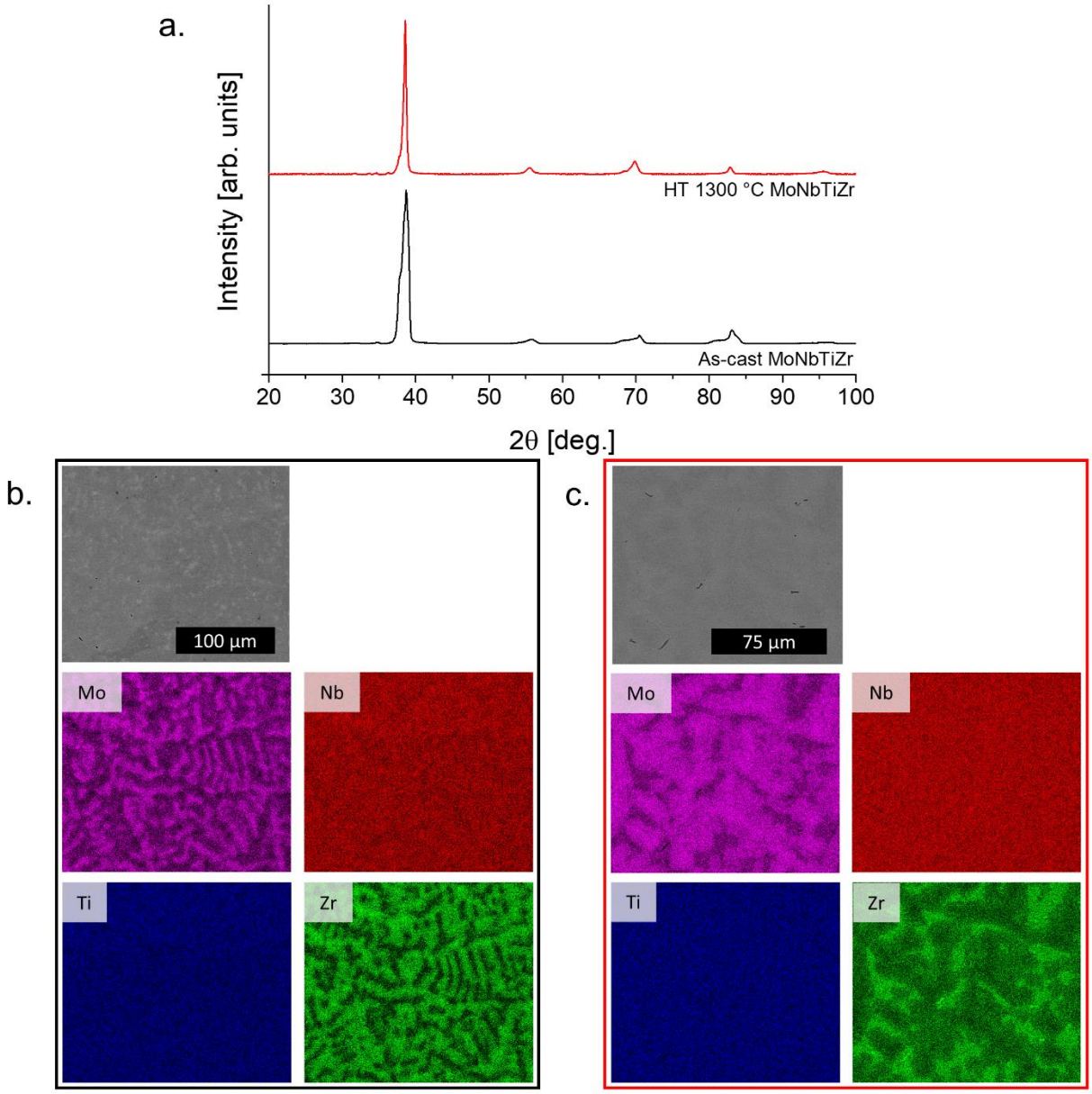

Figure 29. Microstructural analysis of the alloy with no Al from the first batch (a) XRD patterns for the as-cast state and after heat treatment at 1300 °C for 10 hours, (b) SEM EDS mapping of the as-cast state, and (c) SEM EDS mapping of the heat treated state.

The microstructural analysis of the first batch alloy containing 4.3 at.% Al provides further validation of the CALPHAD predictions. The XRD pattern of Figure 30 (a) for the as-cast state has clear doublets at each peak, meaning two distinct BCC phases are present. Figure 30 (b) presents a clear dendritic microstructure in the as-cast state with again Mo-rich BCC 1 dendrites

and Zr-rich BCC 2 interdendritic regions. From the elemental maps of SEM EDS, the segregation of Al to the Zr-rich BCC is also confirmed for the first time in this AlMoNbTiZr RHEA system. The predicted proportions of each BCC phase can also be confirmed by further examination of the XRD pattern for the as-cast state. The doublets for each BCC peak exhibit a lower intensity peak at lower two-theta values and a higher intensity peak at high two-theta values. Since Zr possess the largest metallic radii of the five constituents at 160 pm, see Table 4, the Zr-rich BCC will have a larger lattice parameter and in turn produce XRD peaks at lower two-theta values. With the understanding that the lower two-theta peaks correspond to BCC 2 while the higher angle peaks correspond to BCC 1, the relative intensities of the two patterns validates the prediction that BCC 1 will be the major phase in this composition. Heat treatment of this alloy was conducted at 1500 °C, which is predicted to be within the narrow single BCC phase window in Figure 28 (c). The XRD pattern for the heat treated material, presented in Figure 30 (a), shows a single BCC pattern with relatively symmetric narrow peaks. SEM EDS confirms this homogenization to a single BCC with equiaxed grains and uniform distribution of all constituent elements. While heat treatment of the alloy with no Al at 1300 °C did not completely homogenize the material, heat treatment at 1500 °C successfully homogenized the alloy with 4.3 at.% after ten hours due to the fact that the heat treatment temperature is closer to the melting point of the alloy and enhances the kinetics of diffusion. The observations of the first batch alloy containing 4.3 at.% Al confirmed the dual BCC stability, the segregation of Al to the Zr-rich phase, as well as the single BCC window at high temperature.

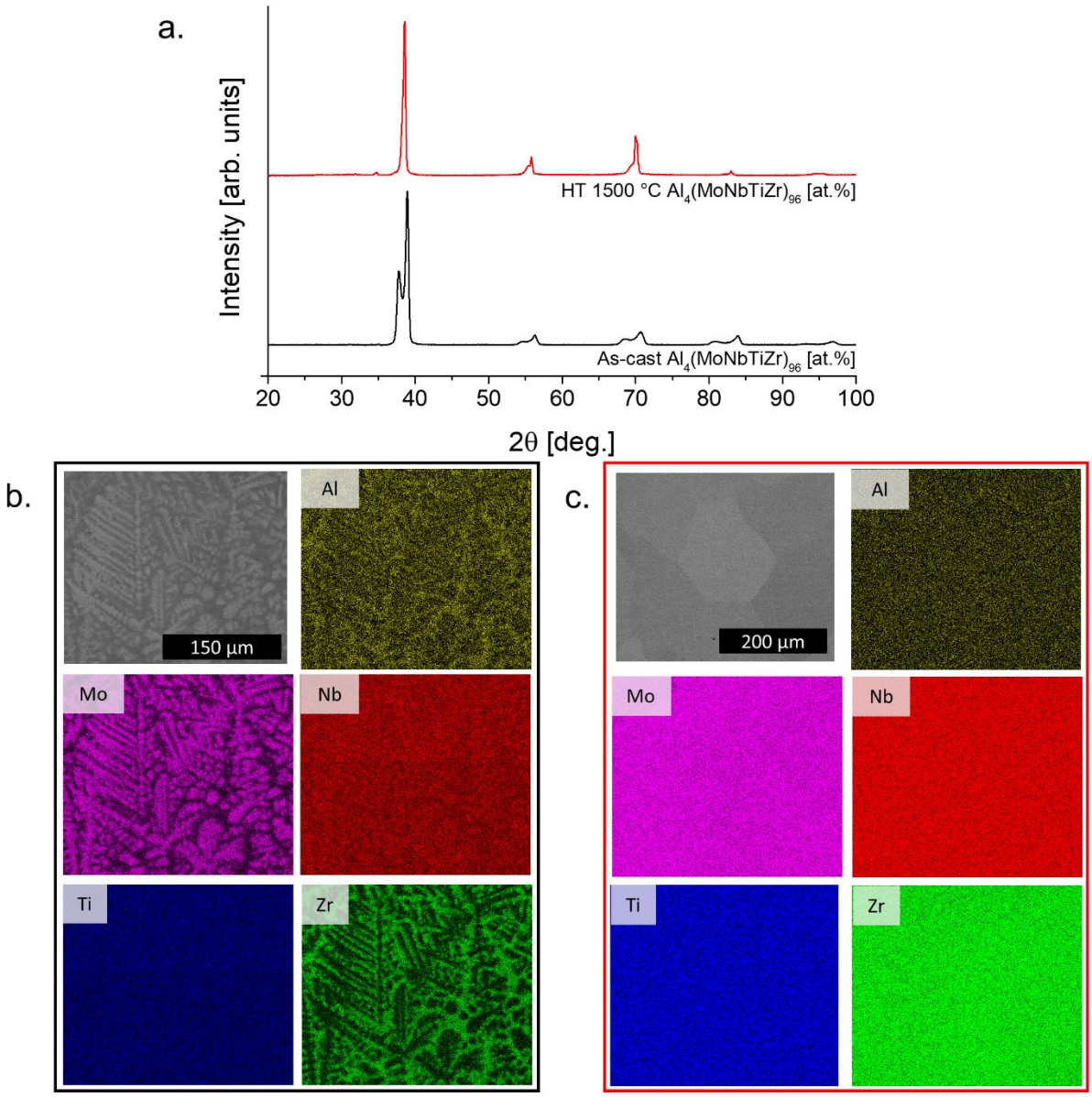

Figure 30. Microstructural analysis of the alloy with 4.3 at.% Al from the first batch (a) XRD patterns for the as-cast state and after heat treatment at 1500 °C for 10 hours, (b) SEM EDS mapping of the as-cast state, and (c) SEM EDS mapping of the heat treated state.

The first batch alloy containing 9.8 at.% Al exhibits a significantly different microstructure than the two alloys with lower Al content, as is expected based on the CALPHAD predictions. Figure 31 (a) shows the XRD pattern of the as-cast state containing major peaks corresponding to the BCC phases with a left shoulder indicative of the two the elemental segregation between Mo

and Zr as discussed previously. In addition to these BCC peaks, other minor peaks are present in the XRD pattern. When investigating the microstructure by SEM EDS, in Figure 31 (b), the same dendritic microstructure in the as-cast state is observed but with the addition of a needle like phase in the interdendritic region. The identity of this intermetallic phase cannot be indexed by existing XRD PDF files, since the phase most likely exhibits a solubility of each constituent that would alter the lattice parameters from a reference pure binary intermetallic phase. Whether it is a laves or Al-Zr rich intermetallic, those phases are predicted to be stable at high temperatures above 1000 °C as seen in Figure 28 (d) which means they could possibly form in the material by casting. After heat treatment at 1500 °C for 10 hours the material exhibits a single BCC pattern in XRD, Figure 31 (a), but still possess a small volume fraction of Zr regions in the microstructure as seen in the SEM EDS of Figure 31 (c). The grains of the microstructure after heat treatment are highly spherical with the Zr-rich regions between them, which is indicative of pre-melting occurring during the heat treatment. When inspecting the step diagram for this alloy in Figure 28 (d) 1500 °C is near the initiation of melting. Moreover, the step diagram for this alloy does not exhibit a region where a single BCC phase is stable which is validated by the remaining Zr-rich phase after heat treatment.

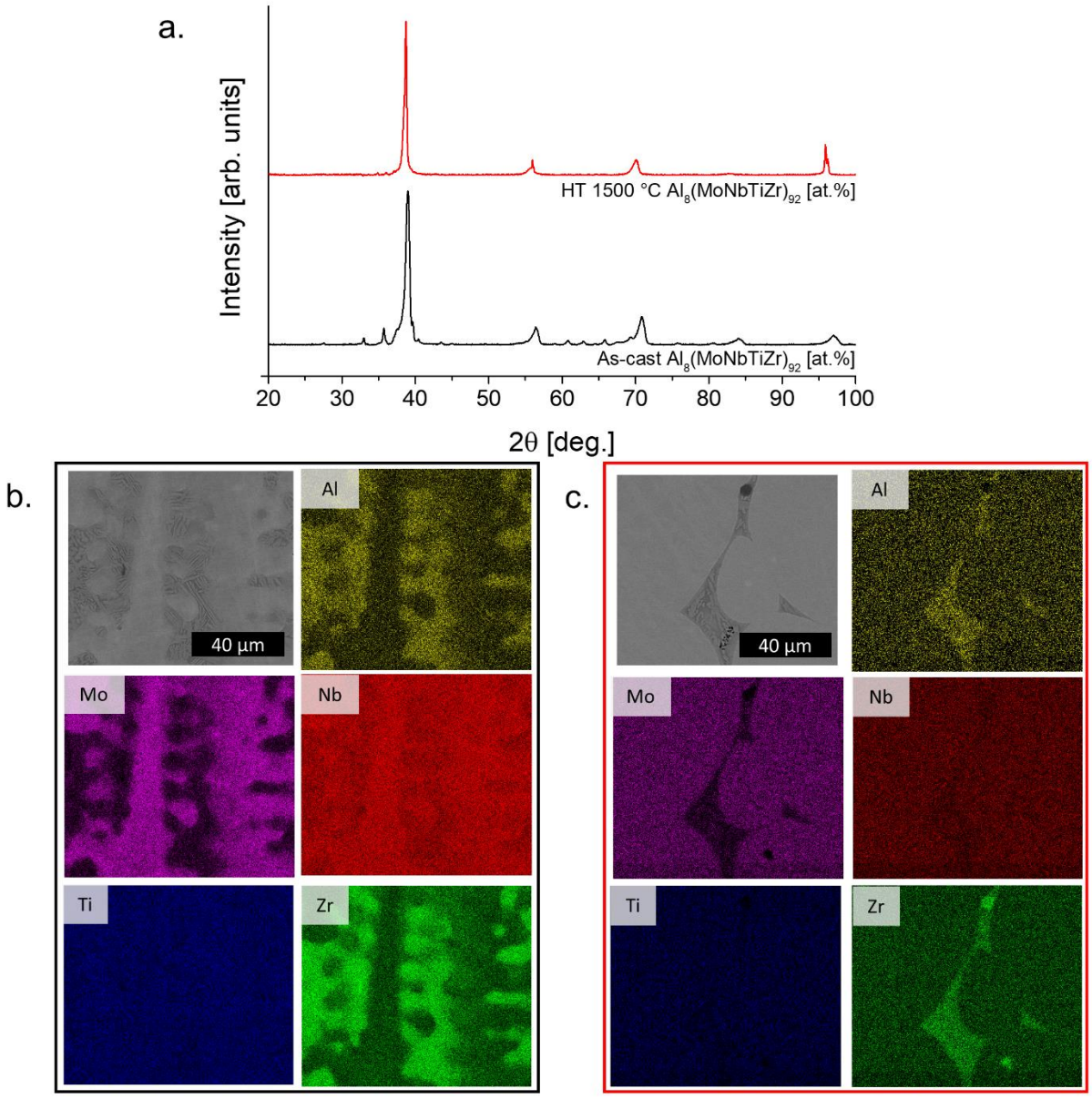

Figure 31. Microstructural analysis of the alloy with 9.8 at.% Al from the first batch (a) XRD patterns for the as-cast state and after heat treatment at 1500 °C for 10 hours, (b) SEM EDS mapping of the as-cast state, and (c) SEM EDS mapping of the heat treated state.

5.3.3. Phase formation and thermal stability in candidate compositions

From the arc-melted buttons of the second batch, with proper composition of feedstock material, samples were prepared for characterization of the as-cast microstructure as well as heat treated at 1500 °C to compare the high temperature phase equilibrium predicted by CALPHAD.

Figure 32 (a) contains the XRD patterns of each composition synthesized in the as-cast state. Each alloy exhibits peaks corresponding to a BCC crystal structure with broadness due to the presence of two BCC phases with different lattice constants. No intermetallic phases are evident from XRD in these as-cast samples. With the addition of Al, the separation of peaks, particularly at higher two theta values, increase. This observation verifies that Al partitions to one of the two BCC phases upon solidification. To identify which BCC phase Al partitions to, SEM EDS was utilized to map the composition of each phase. Figure 32 (b-c) shows the EDS maps of equiatomic MoNbTiZr and $Al_8(MoNbTiZr)_{92}$ at.%. With no Al, the equiatomic composition of MoNbTiZr exhibits some segregation, most evident from Mo enrichment in the dendritic regions and Zr to the interdendritic region. With the addition of 8 at.% Al, the segregation is significantly increased, and Al is found to segregate to the Zr-rich secondary BCC located at the interdendritic region. This trend was also observed in the alloy containing 4 at.% Al. This observation validates the CALPHAD prediction of Al stabilizing the secondary BCC.

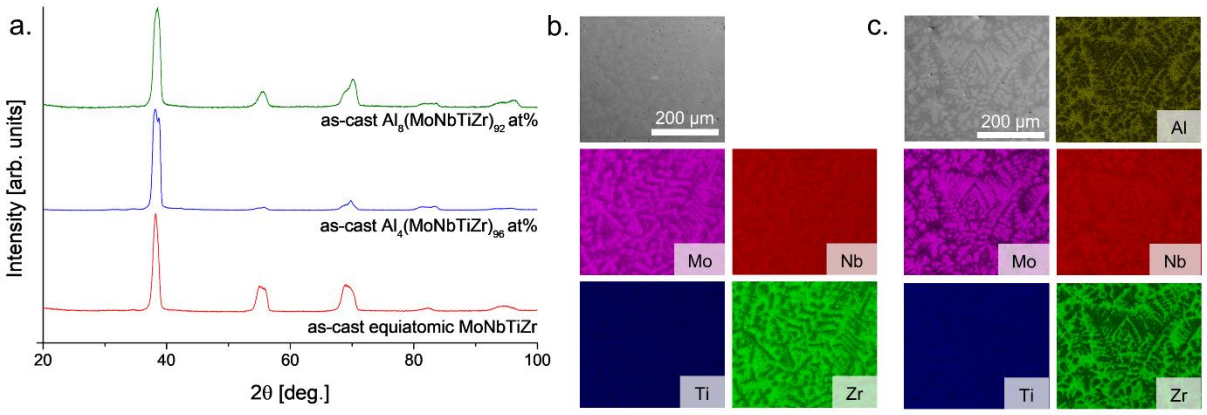

Figure 32. (a) X-ray diffraction patterns of the as-cast samples with increasing Al content showing increasingly broad peaks corresponding to the convolution of two BCC patterns and SEM EDS mapping of (b) MoNbTiZr sample in the as-cast state exhibiting slight chemical segregation in the solidification structure and (c) $Al_8(MoNbTiZr)_{92}$ at% sample in the as-cast state exhibiting significant chemical segregation in the solidification structure.

Another important component of the CALPHAD prediction was that these alloys, below 8 at.% Al, should homogenize to a single BCC phase at elevated temperature. To test these samples were heat treated at 1500 °C for 12 hr followed by an oil quench to freeze in the high temperature microstructure. The XRD patterns of the homogenized samples of each alloy are found in Figure 33 (a). Compared to the as-cast XRD patterns in Figure 32 (a), the peaks of the homogenized samples are narrower indicative of the elimination of the dual BCC microstructure to form a single BCC phase with no additional peaks corresponding intermetallic phases. Small doublets are observable on some higher angle peaks, which are due to the high intensity of the $K_{\alpha 2}$ peak. SEM EDS of the heat-treated and oil-quenched samples confirmed the homogenization of the microstructure of all three alloys. After heat treatment, each alloy possesses a single BCC microstructure with large (~500 μm diameter) equiaxed grains. The EDS mapping results for the alloy containing 4 at.% Al after homogenization are presented in Figure 33 (b) as a representative result of all three alloys.

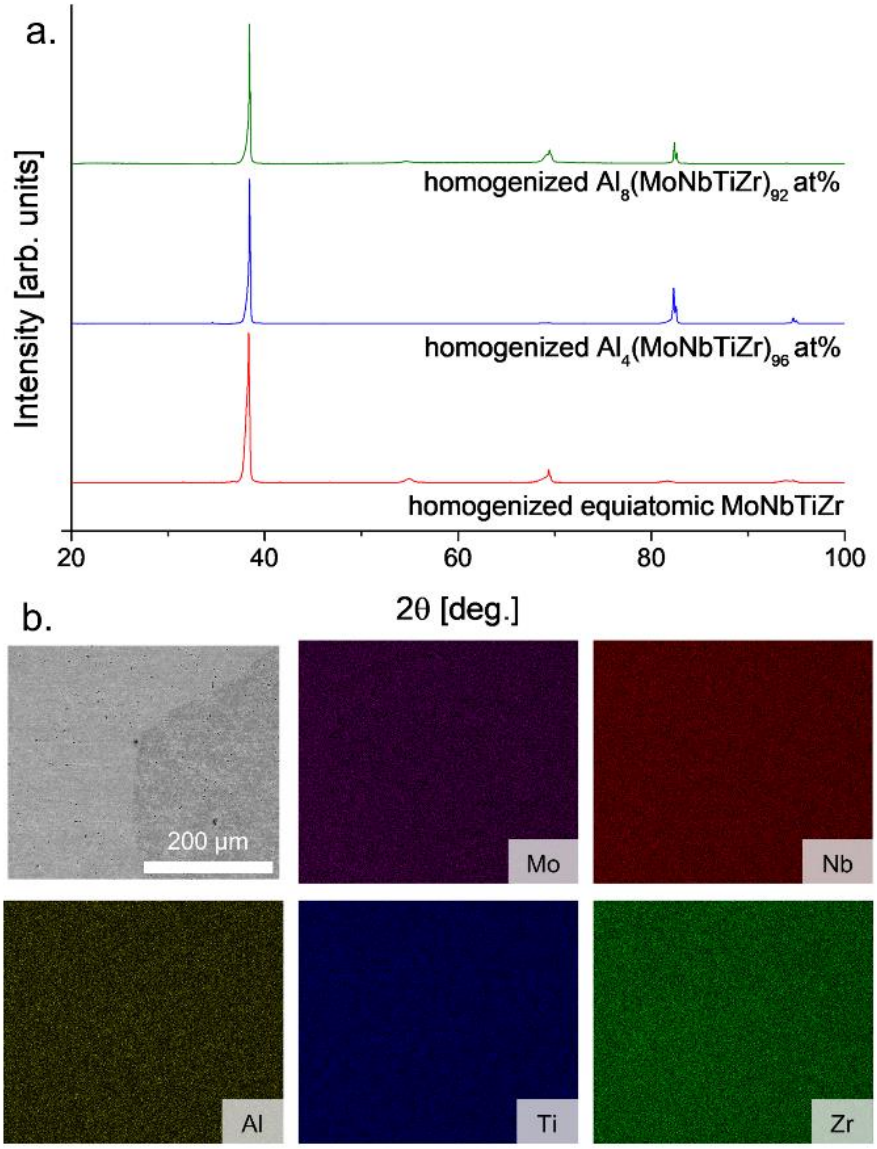

Figure 33. (a) X-ray diffraction patterns of the homogenized samples with increasing Al content showing a single relatively narrow BCC pattern for each sample and (b) SEM EDS mapping of Al4(MoNbTiZr)96 at% sample after homogenization exhibiting equiaxed grains and uniform chemistry.

Semi-quantitative compositional analysis of the three alloys from the second batch was conducted after homogenization using SEM EDS and is presented in Table 6. While the composition measured through SEM-EDS is not as accurate as the DCPES conducted for the first

batch, the results show significantly better agreement between the target composition and the experimental composition. Clearly the second batch does not have the enrichment of Mo that was observed in the first batch. The formation of a single BCC phase after homogenization confirms the predications from CALPHAD for the alloys with no Al and 4 at.% Al, but 8 at.% Al was not expected to be homogenized to a single BCC at 1500 °C. As seen in Table 6 the alloy with 8 at.% Al was measured to contain roughly 7 at.% Al. If this alloy is in fact depleted in Al, it would shift to the left on the isopleth, Figure 27 (a), which would see a region at 1500 °C where it can achieve a single BCC phase. Nevertheless, from this experimental characterization of the three materials, the CALPHAD method for this alloy system is effective for predicting the phases present. These findings motivate the future use of CALPHAD as a tool for the study of RHEAs.

Table 6. Semi-quantitative compositional analysis using SEM-EDS for the second batch of RHEAs.

Second Batch	Al	Mo	Nb	Ti	Zr
Target MoNbTiZr at.%	0	25	25	25	25
Exp. MoNbTiZr at.%	0	24.7 ±0.4	27.5 ±0.1	22.1 ±0.1	25.7 ±0.7
Target $Al_4(MoNbTiZr)_{96}$ at.%	4	24	24	24	24
Exp. $Al_4(MoNbTiZr)_{96}$ at.%	3.8 ±0.1	23.4 ±0.1	26.4 ±0.1	21.5 ±0.1	25.0 ±0.2
Target $Al_8(MoNbTiZr)_{92}$ at.%	8	23	23	23	23
Exp. $Al_8(MoNbTiZr)_{92}$ at.%	7 ±1.3	22.2 ±1.6	25.4 ±1.5	20.9 ±0.4	24.5 ±1.4

5.3.4. Influence of Al content on mechanical behavior

It is important to establish the mechanical behavior of the homogenized single-phase state, to study of effect of adding relatively low concentrations of Al to a disordered solid solution of MoNbTiZr. Initial Vickers microhardness testing of the homogenized samples produced hardness values of 512 ±6 HV, 558 ±5 HV, and 574 ±9 HV for the equiatomic MoNbTiZr, $Al_4(MoNbTiZr)_{96}$ at.%, and $Al_8(MoNbTiZr)_{92}$ at.%, respectively. The increase in hardness with increasing concentration of Al is indicative of a solid solution strengthening mechanism as Al is introduced in the disordered solid solution phase of MoNbTiZr. Since the grain size after homogenization grew to roughly 500 μm, single grains were targeted to produce micropillars for compression tests. EBSD was utilized to identify grains that had specific orientation such that the resulting loading direction in the FIBed micro pillar would be along <110> in the BCC crystal, aligning slip planes at a 45° angle in the pillar [89]. Figure 34 (a-b) presents a representative SEM micrograph of a FIBed micro pillar and stress-strain curves for alloys tested. All alloys exhibited compressive yield strengths at roughly 1500 MPa. The fluctuations observed in the yield strength for each single crystal micropillar is most likely associated to the variability in the Schmid factor pillar to pillar from deviation in the ideal orientation of the grain selected [90]. For the equiatomic MoNbTiZr alloy, after yielding the alloy deforms uniformly with small stress drops associated with the numerous slip traces observable in the postmortem pillar presented in Figure 34 (c). With the addition of Al to MoNbTiZr, plastic flow becomes far more irregular with large scale stress fluctuations. These differences in plastic flow were consistent across all three micropillar tests of each alloy. From these observations, it is expected that the presence of Al in the BCC crystal significantly changes the dislocation behavior.

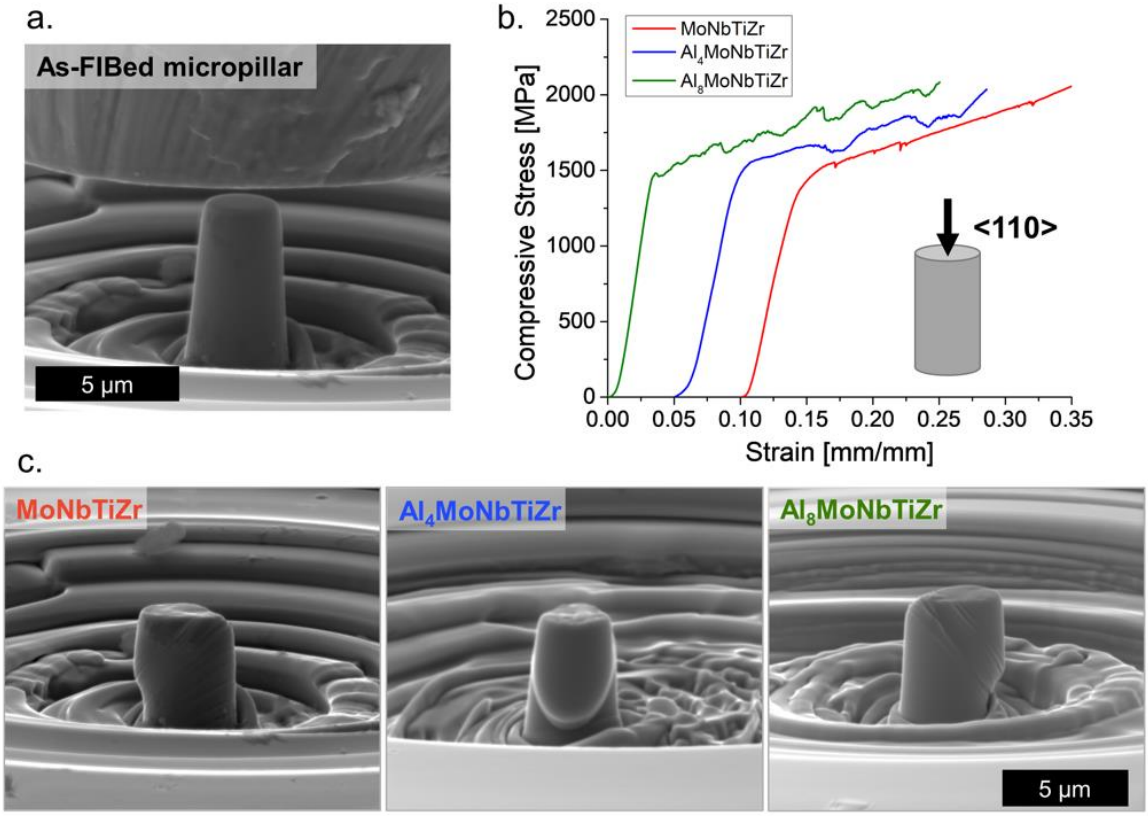

Figure 34. (a) Representative SEM micrograph of the <110> oriented single crystal micropillar prior to testing, (b) compressive stress-strain curves for each alloy with intentional offset for visibility, and (c) micrographs of the postmortem micropillars corresponding to the stress-strain curves in (b) demonstrating clear formation of slip traces at 45° to the loading direction.

5.4. Summary

CALPHAD predictions within the AlMoNbTiZr RHEA system were validated based on experimental assessments of two different batches of alloys with unique compositions. While the alloys of the first batch are off target from the intended compositions, their microstructural evolution from the as-cast state and after high temperature heat treatment enabled the validation of additional CALPHAD predictions within the AlMoNbTiZr RHEA system. The presence of two BCC phases was confirmed, one enriched in Mo and the other in Zr. Al was confirmed to segregate to the Zr-rich phase. The single BCC region at high temperature was verified for the alloy with 4.3

at.% Al. The presence of intermetallic phases in the alloy with 9.8 at.% Al is consistent with the step diagram predicting phase stability. For the second batch that was closer to the target compositions, increasing the concentration of Al from 0 at.% up to 7 at.% promoted the formation of a secondary BCC, enriched in Al and Zr, in the as-cast condition. The stability of a single BCC phase at high temperatures in compositions below 8 at.% Al was confirmed by homogenizations followed by oil quench. Al addition in solid solution with the equiatomic ratio of Mo, Nb, Ti, and Zr increases the hardness of the material and leads to significant variation in the softening of the material during plastic flow.

Chapter 6 : Conclusions

This work has demonstrated a systematic approach to the design and investigation of phase stability in HEAs for structural applications. Based on foundational work in the field of HEAs, critical understanding of phase decomposition in given HEA and its impact on mechanical behavior is identified as an essential aspect of considering said alloy for application. To this end, several studies of targeted HEA compositions were conducted to develop effective methodologies to investigate phase stability and mechanical behavior in HEAs by coupling computational thermodynamic modeling, using the CALPHAD approach, with experimental observations.

The first HEA selected was the equiatomic composition in the CoCuFeMnNi HEA system. Through the detailed study of phase decomposition and how the reported secondary phases influence mechanical behavior, a framework for systematic experimental observation with retrospective CALPHAD analysis was established. Thermomechanical processing, followed by systematic post deformation annealing treatments, revealed the formation of two distinct secondary phases within the equiatomic FCC matrix phase. Low temperature annealing treatments at 600 °C and below led to the nucleation of Fe-Co rich ordered B2 precipitates that contributed precipitation hardening while sufficiently small in size, on the order of 140 nm in diameter. At temperatures < 800 °C Cu segregation, due to its immiscibility with the other constituents, eventually forms a Cu-rich disordered FCC phase that is determined to increase the yield strength of the alloy while reducing the ductility, likely attributable to the presence of additional interfaces. The composition of each phase was experimentally determined and compared to CALPHAD predictions with good agreement. Some short comings of the CALPHAD predictions were identified in the prediction of the Cu-rich disordered FCC phase.

From the understanding of phase stability in the equiatomic composition of CoCuFeMnNi gained by the first study, the next investigation focused on a unique non-equiatomic composition in the CoCuFeMnNi system. Cu and Mn was reduced in the non-equiatomic composition of $Co_{26}Cu_{10}Fe_{27}Mn_{10}Ni_{27}$ at.% HEA to investigate the role of these elements on the mechanical behavior. Processing both the equiatomic and non-equiatomic HEA by HPT enabled a comparative study of the mechanical behavior of the equiatomic CoCuFeMnNi HEA with the non-equiatomic $Co_{26}Cu_{10}Fe_{27}Mn_{10}Ni_{27}$ at.% HEA in and nanocrystalline state and in a coarse grain state after high temperature heat treatment at 1000 °C to maintain a single FCC phase. By experimentally forming and processing by HPT the equiatomic composition of this alloy system along with a non-equiatomic composition with reduced content of Cu and Mn, the differences in their behavior are associated to the different contents of Cu and Mn. More twins were present in the non-equiatomic composition, which could be associated with a lowered the stacking fault energy due to the reduction of Cu and Mn. The equiatomic composition achieved higher strengths at both the as-HPT state and the heat-treated state, demonstrating that Cu and Mn contribute to solid solution strengthening due to their large atomic size compared to the other constituents.

After determining the prominent differences in the equiatomic and non-equiatomic CoCuFeMnNi HEAs in the single phase state, the HPT processed non-equiatomic HEA was further analyzed to elucidate the precise phase stability of this alloy at intermediate temperatures. The non-equiatomic composition of $Co_{26}Cu_{10}Fe_{27}Mn_{10}Ni_{27}$ at.% possesses a reduced concentration of both Cu and Mn to minimize the amount of Cu-rich disordered FCC formation. To determine the implications of this compositional change and the role of processing of the phase stability, the material was processed by HPT to achieve a nanocrystalline face centered cubic (FCC) matrix. DSC thermal analysis of the nanocrystalline sample identified two temperature points for post

deformation heat treatments at 600 °C and 1000 °C. Characterization of the microstructure by automated crystal orientation mapping (ACOM) determined the formation of Fe-Co rich B2 precipitates after heat treatment at 600 °C, while the heat treatment at 1000 °C maintained a single FCC phase. The CALPHAD method correctly predicted the phase stability of the B2 phase as well as the composition and volume fraction of each phase at 600 °C, with the exception of minor Cu segregation within the FCC phase. The presence of the B2 phase increased the stiffness as well as strength of the nanocrystalline HEA while simultaneously causing embrittlement. From this work, DSC is established as an effective tool for experimentally screening for secondary phase formation in HEAs, so long as the microstructure is sufficiently refined.

The final study of this dissertation again probes the phase stability and mechanical behavior in HEAs but transitions from the 3d-transition metal based CoCuFeMnNi HEA system to a refractory based AlMoNbTiZr HEA system. The CALPHAD approach predicted a specific phase stability of a dual BCC microstructure with varying stability of secondary phases. To validate these predictions targeted non-equiatomic compositions from this system were experimentally formed by arc melting. Two batches were created, the first with incorrect Mo-rich compositions and the second batch with an experimental composition closer to the target for each alloy. By recalculating the CALPHAD predictions for these experimentally formed alloys in the first batch, both batches were characterized in the as-cast state as well as heat treated to validate CALPHAD approach for the AlMoNbTiZr HEA system. For the target alloys Al additions below 8 at.% enhanced the formation of a secondary BCC upon solidification while maintaining a single-phase BCC region at elevated temperatures. The hardness of the alloys increased with the increase of Al and deformation behavior in single-crystal micropillar samples are markedly different with and without Al. As a whole, this dissertation provides a synergistic framework of experiment and modeling to

probe the phase stability and mechanical behavior of HEAs. This approach can be further enhanced and applied to the entire field to accelerate the development of HEAs for structural applications.

Chapter 7 : Recommendations for further research

This dissertation research makes significant headway for the field of HEAs, to better understand the phase stability and mechanical behavior in HEAs as well as establish a more nuanced approach to compositional design within the compositional space occupied by HEAs. Critical findings from this work present key directions that are essential to the growth of the field. These include the improvement of the CALPHAD approach for HEAs, augmentation of mechanical property models to apply to HEA solid solution phases, and the expansion of interfacial science within HEAs. While this is not a comprehensive list of directions for the field, these are the most essential for the promotion of HEAs as viable engineering materials.

Based on the previous chapters, the CALPHAD approach, using the current HEA database from ThermoCalc, is effective in determining features of a particular HEA composition or system. Important aspects of a given composition were identified and validated with experiment including solidus and liquidus temperatures, identity of the primary solid phase, identity of possible secondary phases, and phase compositions. While these are informative for the design of an alloy, more refined aspects of phase stability were consistently unreliable particularly the specification of secondary phase solvus temperatures. To enhance the predictive power of the CALPHAD approach for HEAs, the thermodynamic database must be improved. While companies such as ThermoCalc have made great strides to produce databases applicable to the complex concentrated compositional space of HEAs, many require additional data to be more universally applicable. A combination of both theoretical and experimental analysis required to fill these gaps. This work may come in the form of density functional theory DFT calculations of multicomponent systems within the realm of HEAs, as well as experimental thermal analyses using calorimetry techniques of experimentally prepared compositions with representative starting microstructures. With a more

uniformly assessed compositional space the application of the CALPHAD approach with provide further guidance to the design of HEAs.

In addition to thermodynamic modeling, the effective modeling of material properties including strength is essential to HEA development. In chapter 3, the comparison of the equiatomic CoCuFeMnNi HEA to the non-equiatomic composition $Co_{26}Cu_{10}Fe_{27}Mn_{10}Ni_{27}$ at.% established the trend that reducing the concentration of Cu and Mn led to a reduction in the tensile strength of the samples with similar yield strengths. While this trend eludes to the role of each constituent element on the solid solution strengthening of the alloys, the precise strength associated to solid solution strengthening in this alloy cannot be established using conventional solid solution strengthening models [91,92]. Recently, novel models have been proposed by a variety of researchers with varying accuracy and applicability to various subsets of HEAs [93–96]. Further evolution of these models of solid solution strengthening and other properties models will enable the application of integrated computational materials engineering (ICME) for HEAs.

The influence of interfaces on the phase stability in the nanocrystalline $Co_{26}Cu_{10}Fe_{27}Mn_{10}Ni_{27}$ at.% HEA presented in chapter 4, exposes the need for further development of interfacial sciences in HEAs. Grain boundaries in the nanocrystalline HEA provided diffusion pathways and preferential nucleation sites within the material during heat treatment at intermediate temperature. The study found the intergranular precipitation of a B2 phase as well as segregation of constituent elements namely Cu. This boundary dependent phase formation has led to a follow up study currently underway to probe further the initiation of phase decomposition in this nanocrystalline HEA using in situ TEM heating experiments coupled with ACOM mapping, chemical mapping, and atom probe tomography (APT). Preliminary results have found specific orientation relationships between matrix and precipitate phases as well as several unique

compositions of grain boundary segregants. Beyond the CoCuFeMnNi system, investigating the role of interfaces in the behavior of HEAs should be considered more in the field of HEAs.

HEAs and their design approach present a novel method to developing engineering materials. While the understanding of these materials has grown immensely in recent years, additional work is required to further integrate them as engineering materials. This includes the expansion of databases used for CALPHAD, articulation of new property models applicable to the complex concentrated phases present in HEAs, and the focus of interfacial science in HEAs. Together these specific areas will accelerate the research of HEAs, promote the use of ICME design, and create opportunities for applying HEAs to engineering applications.

REFERENCES

[1] J.W. Yeh, Recent Progress in High-entropy Alloys, Eur. J. Control. 31 (2006) 633–648.

[2] E.J. Pickering, R. Muñoz-Moreno, H.J. Stone, N.G. Jones, Precipitation in the equiatomic high-entropy alloy CrMnFeCoNi, Scr. Mater. 113 (2016) 106–109. https://doi.org/10.1016/j.scriptamat.2015.10.025.

[3] D. Miracle, B. Majumdar, K. Wertz, S. Gorsse, New strategies and tests to accelerate discovery and development of multi-principal element structural alloys, Scr. Mater. 127 (2017) 195–200. https://doi.org/10.1016/j.scriptamat.2016.08.001.

[4] D.B. Miracle, High-Entropy Alloys: A Current Evaluation of Founding Ideas and Core Effects and Exploring "Nonlinear Alloys," JOM. 69 (2017) 2130–2136. https://doi.org/10.1007/s11837-017-2527-z.

[5] S. Gorsse, D.B. Miracle, O.N. Senkov, Mapping the world of complex concentrated alloys, Acta Mater. 135 (2017) 177–187. https://doi.org/10.1016/j.actamat.2017.06.027.

[6] H. Mao, H.-L. Chen, Q. Chen, TCHEA1: A Thermodynamic Database Not Limited for "High Entropy" Alloys, J. Phase Equilibria Diffus. 38 (2017) 353–368. https://doi.org/10.1007/s11669-017-0570-7.

[7] B. Cantor, I.T.H. Chang, P. Knight, A.J.B. Vincent, Microstructural development in equiatomic multicomponent alloys, Mater. Sci. Eng. A. 375–377 (2004) 213–218. https://doi.org/10.1016/j.msea.2003.10.257.

[8] J.-W. Yeh, S.-K. Chen, S.-J. Lin, J.-Y. Gan, T.-S. Chin, T.-T. Shun, C.-H. Tsau, S.-Y. Chang, Nanostructured High-Entropy Alloys with Multiple Principal Elements: Novel Alloy Design Concepts and Outcomes, Adv. Eng. Mater. 6 (2004) 299–303. https://doi.org/10.1002/adem.200300567.

[9] C.-Y. Hsu, J.-W. Yeh, S.-K. Chen, T.-T. Shun, Wear resistance and high-temperature compression strength of Fcc CuCoNiCrAl0.5Fe alloy with boron addition, Metall. Mater. Trans. A. 35 (2004) 1465–1469. https://doi.org/10.1007/s11661-004-0254-x.

[10] J.-W. Yeh, S.-J. Lin, T.-S. Chin, J.-Y. Gan, S.-K. Chen, T.-T. Shun, C.-H. Tsau, S.-Y. Chou, Formation of simple crystal structures in Cu-Co-Ni-Cr-Al-Fe-Ti-V alloys with multiprincipal metallic elements, Metall. Mater. Trans. A. 35 (2004) 2533–2536. https://doi.org/10.1007/s11661-006-0234-4.

[11] P.-K. Huang, J.-W. Yeh, T.-T. Shun, S.-K. Chen, Multi-Principal-Element Alloys with Improved Oxidation and Wear Resistance for Thermal Spray Coating, Adv. Eng. Mater. 6 (2004) 74–78. https://doi.org/10.1002/adem.200300507.

[12] T.K. Chen, T.T. Shun, J.W. Yeh, M.S. Wong, Nanostructured nitride films of multi-element high-entropy alloys by reactive DC sputtering, Surf. Coat. Technol. 188–189 (2004) 193–200. https://doi.org/10.1016/j.surfcoat.2004.08.023.

[13] M.-H. Tsai, J.-W. Yeh, High-Entropy Alloys: A Critical Review, Mater. Res. Lett. 2 (2014) 107–123. https://doi.org/10.1080/21663831.2014.912690.

[14] Y. Zhang, T.T. Zuo, Z. Tang, M.C. Gao, K.A. Dahmen, P.K. Liaw, Z.P. Lu, Microstructures and properties of high-entropy alloys, Prog. Mater. Sci. 61 (2014) 1–93. https://doi.org/10.1016/j.pmatsci.2013.10.001.

[15] E.J. Pickering, N.G. Jones, High-entropy alloys: a critical assessment of their founding principles and future prospects, Int. Mater. Rev. 61 (2016) 183–202. https://doi.org/10.1080/09506608.2016.1180020.

[16] D.B. Miracle, O.N. Senkov, A critical review of high entropy alloys and related concepts, Acta Mater. 122 (2017) 448–511. https://doi.org/10.1016/j.actamat.2016.08.081.

[17] B.E. MacDonald, Z. Fu, B. Zheng, W. Chen, Y. Lin, F. Chen, L. Zhang, J. Ivanisenko, Y. Zhou, H. Hahn, E.J. Lavernia, Recent Progress in High Entropy Alloy Research, JOM. 69 (2017) 2024–2031. https://doi.org/10.1007/s11837-017-2484-6.

[18] E.P. George, D. Raabe, R.O. Ritchie, High-entropy alloys, Nat. Rev. Mater. 4 (2019) 515–534. https://doi.org/10.1038/s41578-019-0121-4.

[19] M.C. Gao, J.W. Yeh, P.K. Liaw, Y. Zhang, eds., High-Entropy Alloys - Fundamentals and Applications, Springer, 2016. http://www.springer.com/us/book/9783319270111 (accessed April 23, 2017).

[20] J. Bishop-Moser, D.B. Miracle, Manufacturing High Entropy Alloys Pathway to Industrial Competitiveness, MForesight, 2018.

[21] J.-W. Yeh, S.-Y. Chang, Y.-D. Hong, S.-K. Chen, S.-J. Lin, Anomalous decrease in X-ray diffraction intensities of Cu–Ni–Al–Co–Cr–Fe–Si alloy systems with multi-principal elements, Mater. Chem. Phys. 103 (2007) 41–46. https://doi.org/10.1016/j.matchemphys.2007.01.003.

[22] L.R. Owen, E.J. Pickering, H.Y. Playford, H.J. Stone, M.G. Tucker, N.G. Jones, An assessment of the lattice strain in the CrMnFeCoNi high-entropy alloy, Acta Mater. 122 (2017) 11–18. https://doi.org/10.1016/j.actamat.2016.09.032.

[23] K.-Y. Tsai, M.-H. Tsai, J.-W. Yeh, Sluggish diffusion in Co–Cr–Fe–Mn–Ni high-entropy alloys, Acta Mater. 61 (2013) 4887–4897. https://doi.org/10.1016/j.actamat.2013.04.058.

[24] M. Vaidya, S. Trubel, B.S. Murty, G. Wilde, S.V. Divinski, Ni tracer diffusion in CoCrFeNi and CoCrFeMnNi high entropy alloys, J. Alloys Compd. 688, Part B (2016) 994–1001. https://doi.org/10.1016/j.jallcom.2016.07.239.

[25] B. Gludovatz, A. Hohenwarter, D. Catoor, E.H. Chang, E.P. George, R.O. Ritchie, A fracture-resistant high-entropy alloy for cryogenic applications, Science. 345 (2014) 1153–1158. https://doi.org/10.1126/science.1254581.

[26] F. Otto, A. Dlouhý, Ch. Somsen, H. Bei, G. Eggeler, E.P. George, The influences of temperature and microstructure on the tensile properties of a CoCrFeMnNi high-entropy alloy, Acta Mater. 61 (2013) 5743–5755. https://doi.org/10.1016/j.actamat.2013.06.018.

[27] D.J.M. King, S.C. Middleburgh, A.G. McGregor, M.B. Cortie, Predicting the formation and stability of single phase high-entropy alloys, Acta Mater. 104 (2016) 172–179. https://doi.org/10.1016/j.actamat.2015.11.040.

[28] H.L. Lukas, S.G. Fries, B. Sundman, Computational thermodynamics: the Calphad method, Cambridge university press, Cambridge, 2007.

[29] H.-L. Chen, H. Mao, Q. Chen, Database development and Calphad calculations for high entropy alloys: Challenges, strategies, and tips, Mater. Chem. Phys. (2017). https://doi.org/10.1016/j.matchemphys.2017.07.082.

[30] A. Abu-Odeh, E. Galvan, T. Kirk, H. Mao, Q. Chen, P. Mason, R. Malak, R. Arroyave, Exploration of the High Entropy Alloy Space as a Constraint Satisfaction Problem, ArXiv171202442 Cond-Mat. (2017). http://arxiv.org/abs/1712.02442 (accessed June 7, 2018).

[31] N.L. Okamoto, S. Fujimoto, Y. Kambara, M. Kawamura, Z.M.T. Chen, H. Matsunoshita, K. Tanaka, H. Inui, E.P. George, Size effect, critical resolved shear stress, stacking fault energy, and solid solution strengthening in the CrMnFeCoNi high-entropy alloy, Sci. Rep. 6 (2016) 35863. https://doi.org/10.1038/srep35863.

[32] F. Otto, A. Dlouhý, K.G. Pradeep, M. Kuběnová, D. Raabe, G. Eggeler, E.P. George, Decomposition of the single-phase high-entropy alloy CrMnFeCoNi after prolonged anneals at intermediate temperatures, Acta Mater. 112 (2016) 40–52. https://doi.org/10.1016/j.actamat.2016.04.005.

[33] Y.-F. Kao, T.-J. Chen, S.-K. Chen, J.-W. Yeh, Microstructure and mechanical property of as-cast, -homogenized, and -deformed AlxCoCrFeNi ($0 \leq x \leq 2$) high-entropy alloys, J. Alloys Compd. 488 (2009) 57–64. https://doi.org/10.1016/j.jallcom.2009.08.090.

[34] J.Y. He, H. Wang, Y. Wu, X.J. Liu, H.H. Mao, T.G. Nieh, Z.P. Lu, Precipitation behavior and its effects on tensile properties of FeCoNiCr high-entropy alloys, Intermetallics. 79 (2016) 41–52. https://doi.org/10.1016/j.intermet.2016.09.005.

[35] J.Y. He, W.H. Liu, H. Wang, Y. Wu, X.J. Liu, T.G. Nieh, Z.P. Lu, Effects of Al addition on structural evolution and tensile properties of the FeCoNiCrMn high-entropy alloy system, Acta Mater. 62 (2014) 105–113. https://doi.org/10.1016/j.actamat.2013.09.037.

[36] W.H. Liu, Z.P. Lu, J.Y. He, J.H. Luan, Z.J. Wang, B. Liu, Y. Liu, M.W. Chen, C.T. Liu, Ductile CoCrFeNiMox high entropy alloys strengthened by hard intermetallic phases, Acta Mater. 116 (2016) 332–342. https://doi.org/10.1016/j.actamat.2016.06.063.

[37] B. Gwalani, S. Gorsse, D. Choudhuri, M. Styles, Y. Zheng, R.S. Mishra, R. Banerjee, Modifying transformation pathways in high entropy alloys or complex concentrated alloys

via thermo-mechanical processing, Acta Mater. 153 (2018) 169–185. https://doi.org/10.1016/j.actamat.2018.05.009.

[38] M. Pohl, O. Storz, T. Glogowski, Effect of intermetallic precipitations on the properties of duplex stainless steel, Mater. Charact. 58 (2007) 65–71. https://doi.org/10.1016/j.matchar.2006.03.015.

[39] A. Takeuchi, A. Inoue, Classification of Bulk Metallic Glasses by Atomic Size Difference, Heat of Mixing and Period of Constituent Elements and Its Application to Characterization of the Main Alloying Element, Mater. Trans. 46 (2005) 2817–2829. https://doi.org/10.2320/matertrans.46.2817.

[40] Tazuddin, K. Biswas, N.P. Gurao, Deciphering micro-mechanisms of plastic deformation in a novel single phase fcc-based MnFeCoNiCu high entropy alloy using crystallographic texture, Mater. Sci. Eng. A. 657 (2016) 224–233. https://doi.org/10.1016/j.msea.2016.01.065.

[41] A. Takeuchi, T. Wada, Y. Zhang, MnFeNiCuPt and MnFeNiCuCo high-entropy alloys designed based on L10 structure in Pettifor map for binary compounds, Intermetallics. 82 (2017) 107–115. https://doi.org/10.1016/j.intermet.2016.12.002.

[42] R. Sonkusare, P. Divya Janani, N.P. Gurao, S. Sarkar, S. Sen, K.G. Pradeep, K. Biswas, Phase equilibria in equiatomic CoCuFeMnNi high entropy alloy, Mater. Chem. Phys. 210 (2018) 269–278. https://doi.org/10.1016/j.matchemphys.2017.08.051.

[43] R. Agarwal, R. Sonkusare, S.R. Jha, N.P. Gurao, K. Biswas, N. Nayan, Understanding the deformation behavior of CoCuFeMnNi high entropy alloy by investigating mechanical properties of binary ternary and quaternary alloy subsets, Mater. Des. 157 (2018) 539–550. https://doi.org/10.1016/j.matdes.2018.07.046.

[44] D.A. Porter, K.E. Easterling, M.Y. Sherif, Phase Transformation in Metals and Alloys, Third, Taylor & Francis Group, LLC, 2009.

[45] Z. Wu, H. Bei, F. Otto, G.M. Pharr, E.P. George, Recovery, recrystallization, grain growth and phase stability of a family of FCC-structured multi-component equiatomic solid solution alloys, Intermetallics. 46 (2014) 131–140. https://doi.org/10.1016/j.intermet.2013.10.024.

[46] F.J. Humphreys, M. Hatherly, Recrystallization and Related Annealing Phenomena, Elsevier, 2012.

[47] K. Ma, H. Wen, T. Hu, T.D. Topping, D. Isheim, D.N. Seidman, E.J. Lavernia, J.M. Schoenung, Mechanical behavior and strengthening mechanisms in ultrafine grain precipitation-strengthened aluminum alloy, Acta Mater. 62 (2014) 141–155. https://doi.org/10.1016/j.actamat.2013.09.042.

[48] M. Aykol, A.O. Mekhrabov, M.V. Akdeniz, Effect of vanadium on atomic ordering characteristics and anti-phase boundary energies of B2–FeCo alloys, Intermetallics. 18 (2010) 893–899. https://doi.org/10.1016/j.intermet.2009.12.029.

[49] J.Y. He, H. Wang, H.L. Huang, X.D. Xu, M.W. Chen, Y. Wu, X.J. Liu, T.G. Nieh, K. An, Z.P. Lu, A precipitation-hardened high-entropy alloy with outstanding tensile properties, Acta Mater. 102 (2016) 187–196. https://doi.org/10.1016/j.actamat.2015.08.076.

[50] D.-H. Lee, I.-C. Choi, M.-Y. Seok, J. He, Z. Lu, J.-Y. Suh, M. Kawasaki, T.G. Langdon, J. Jang, Nanomechanical behavior and structural stability of a nanocrystalline CoCrFeNiMn high-entropy alloy processed by high-pressure torsion, J. Mater. Res. 30 (2015) 2804–2815. https://doi.org/10.1557/jmr.2015.239.

[51] N. Park, X. Li, N. Tsuji, Microstructure and Mechanical Properties of Co21Cr22Cu22Fe21Ni14 Processed by High Pressure Torsion and Annealing, JOM. 67 (2015) 2303–2309. https://doi.org/10.1007/s11837-015-1586-2.

[52] P.F. Yu, H. Cheng, L.J. Zhang, H. Zhang, Q. Jing, M.Z. Ma, P.K. Liaw, G. Li, R.P. Liu, Effects of high pressure torsion on microstructures and properties of an Al0.1CoCrFeNi high-entropy alloy, Mater. Sci. Eng. A. 655 (2016) 283–291. https://doi.org/10.1016/j.msea.2015.12.085.

[53] D.-H. Lee, J.-A. Lee, Y. Zhao, Z. Lu, J.-Y. Suh, J.-Y. Kim, U. Ramamurty, M. Kawasaki, T.G. Langdon, J. Jang, Annealing effect on plastic flow in nanocrystalline CoCrFeMnNi high-entropy alloy: A nanomechanical analysis, Acta Mater. (2017). https://doi.org/10.1016/j.actamat.2017.08.057.

[54] Q.H. Tang, Y. Huang, Y.Y. Huang, X.Z. Liao, T.G. Langdon, P.Q. Dai, Hardening of an Al0.3CoCrFeNi high entropy alloy via high-pressure torsion and thermal annealing, Mater. Lett. 151 (2015) 126–129. https://doi.org/10.1016/j.matlet.2015.03.066.

[55] B. Schuh, F. Mendez-Martin, B. Völker, E.P. George, H. Clemens, R. Pippan, A. Hohenwarter, Mechanical properties, microstructure and thermal stability of a nanocrystalline CoCrFeMnNi high-entropy alloy after severe plastic deformation, Acta Mater. 96 (2015) 258–268. https://doi.org/10.1016/j.actamat.2015.06.025.

[56] A.P. Zhilyaev, T.G. Langdon, Using high-pressure torsion for metal processing: Fundamentals and applications, Prog. Mater. Sci. 53 (2008) 893–979. https://doi.org/10.1016/j.pmatsci.2008.03.002.

[57] K. Edalati, Z. Horita, High-pressure torsion of pure metals: Influence of atomic bond parameters and stacking fault energy on grain size and correlation with hardness, Acta Mater. 59 (2011) 6831–6836. https://doi.org/10.1016/j.actamat.2011.07.046.

[58] J.B. Nelson, D.P. Riley, An experimental investigation of extrapolation methods in the derivation of accurate unit-cell dimensions of crystals, Proc. Phys. Soc. 57 (1945) 160. https://doi.org/10.1088/0959-5309/57/3/302.

[59] D.L. Beke, G. Erdélyi, On the diffusion in high-entropy alloys, Mater. Lett. 164 (2016) 111–113. https://doi.org/10.1016/j.matlet.2015.09.028.

[60] S. Mahajan, C.S. Pande, M.A. Imam, B.B. Rath, Formation of annealing twins in f.c.c. crystals, Acta Mater. 45 (1997) 2633–2638. https://doi.org/10.1016/S1359-6454(96)00336-9.

[61] Z. Zhang, M.M. Mao, J. Wang, B. Gludovatz, Z. Zhang, S.X. Mao, E.P. George, Q. Yu, R.O. Ritchie, Nanoscale origins of the damage tolerance of the high-entropy alloy CrMnFeCoNi, Nat. Commun. 6 (2015) 10143. https://doi.org/10.1038/ncomms10143.

[62] Z. Fu, L. Jiang, J.L. Wardini, B.E. MacDonald, H. Wen, W. Xiong, D. Zhang, Y. Zhou, T.J. Rupert, W. Chen, E.J. Lavernia, A high-entropy alloy with hierarchical nanoprecipitates and ultrahigh strength, Sci. Adv. 4 (2018) eaat8712. https://doi.org/10.1126/sciadv.aat8712.

[63] H. Shahmir, J. He, Z. Lu, M. Kawasaki, T.G. Langdon, Effect of annealing on mechanical properties of a nanocrystalline CoCrFeNiMn high-entropy alloy processed by high-pressure torsion, Mater. Sci. Eng. A. 676 (2016) 294–303. https://doi.org/10.1016/j.msea.2016.08.118.

[64] B.E. MacDonald, Z. Fu, X. Wang, Z. Li, W. Chen, Y. Zhou, D. Raabe, J. Schoenung, H. Hahn, E.J. Lavernia, Influence of phase decomposition on mechanical behavior of an equiatomic CoCuFeMnNi high entropy alloy, Acta Mater. 181 (2019) 25–35. https://doi.org/10.1016/j.actamat.2019.09.030.

[65] S. Gorsse, F. Tancret, Current and emerging practices of CALPHAD toward the development of high entropy alloys and complex concentrated alloys, J. Mater. Res. (2018) 1–25. https://doi.org/10.1557/jmr.2018.152.

[66] S. Gorsse, O.N. Senkov, About the Reliability of CALPHAD Predictions in Multicomponent Systems, Entropy. 20 (2018) 899. https://doi.org/10.3390/e20120899.

[67] tchea3_extended_info.pdf, (n.d.). https://www.thermocalc.com/media/35873/tchea3_extended_info.pdf (accessed July 24, 2020).

[68] O.N. Senkov, S. Gorsse, D.B. Miracle, High temperature strength of refractory complex concentrated alloys, Acta Mater. 175 (2019) 394–405. https://doi.org/10.1016/j.actamat.2019.06.032.

[69] Key_Technical_Data_en_DSC_404_F1_F3_Pegasus.pdf, (n.d.). https://d2brmtk65c6tyc.cloudfront.net/media/thermal-analysis/Data-Sheets/Key_Technical_Data_en_DSC_404_F1_F3_Pegasus.pdf?1568871973&Policy=eyJTdGF0ZW1lbnQiOlt7IlJlc291cmNlIjoiaHR0cHM6XC9cL2QyYnJtdGs2NWM2dHljLmNsb3VkZnJvbnQubmV0XC9tZWRpYVwvdGhlcm1hbC1hbmFseXNpc1wvRGF0YS1TaGVldHNcL0tleV9UZWNobmljYWxfRGF0YV9lbl9EU0NfNDA0X0YxX0YzX1BlZ2FzdXMucGRmPzE1Njg4NzE5NzMiLCJDb25kaXRpb24iOnsiRGF0ZUxlc3NUaGFuIjp7IkFXUzpFcG9jaFRpbWUiOjE1OTUwMjA0NDR9fX1dfQ__&Signature=JRrdfGwqGVgC4xObCM-

v7aFgLKsLzXjRHE7YlhjU62OfZgjVt1srw4FqiFI56AkzIlmfNJcXIZ1dSzn91ziOwxn4Ht4Ul5hWdAdOClDhSV7fvWRL1QuCqodAroox17MLz9TJynpooXtC2z1U52QCxxELTCYwpIjcS8BdnTd1A~E_&Key-Pair-Id=APKAIBNUHYIJDHQEJVRQ (accessed July 16, 2020).

[70] A. Kobler, A. Kashiwar, H. Hahn, C. Kübel, Combination of in situ straining and ACOM TEM: A novel method for analysis of plastic deformation of nanocrystalline metals, Ultramicroscopy. 128 (2013) 68–81. https://doi.org/10.1016/j.ultramic.2012.12.019.

[71] K. Edalati, Z. Horita, T. Furuta, S. Kuramoto, Dynamic recrystallization and recovery during high-pressure torsion: Experimental evidence by torque measurement using ring specimens, Mater. Sci. Eng. A. 559 (2013) 506–509. https://doi.org/10.1016/j.msea.2012.08.132.

[72] Y. Ito, Z. Horita, Microstructural evolution in pure aluminum processed by high-pressure torsion, Mater. Sci. Eng. A. 503 (2009) 32–36. https://doi.org/10.1016/j.msea.2008.03.055.

[73] Y.H. Zhao, X.Z. Liao, Y.T. Zhu, Z. Horita, T.G. Langdon, Influence of stacking fault energy on nanostructure formation under high pressure torsion, Mater. Sci. Eng. A. 410–411 (2005) 188–193. https://doi.org/10.1016/j.msea.2005.08.074.

[74] H.G. Jiang, M. Rühle, E.J. Lavernia, On the applicability of the X-ray diffraction line profile analysis in extracting grain size and microstrain in nanocrystalline materials, J. Mater. Res. 14 (1999) 549–559. https://doi.org/10.1557/JMR.1999.0079.

[75] J.E. Saal, I.S. Berglund, J.T. Sebastian, P.K. Liaw, G.B. Olson, Equilibrium high entropy alloy phase stability from experiments and thermodynamic modeling, Scr. Mater. 146 (2018) 5–8. https://doi.org/10.1016/j.scriptamat.2017.10.027.

[76] J. Su, D. Raabe, Z. Li, Hierarchical microstructure design to tune the mechanical behavior of an interstitial TRIP-TWIP high-entropy alloy, Acta Mater. 163 (2019) 40–54. https://doi.org/10.1016/j.actamat.2018.10.017.

[77] Z. Li, C.C. Tasan, H. Springer, B. Gault, D. Raabe, Interstitial atoms enable joint twinning and transformation induced plasticity in strong and ductile high-entropy alloys, Sci. Rep. 7 (2017) 40704. https://doi.org/10.1038/srep40704.

[78] J.-G. Jung, Y.-H. Cho, J.-M. Lee, H.-W. Kim, K. Euh, Designing the composition and processing route of aluminum alloys using CALPHAD: Case studies, Calphad. 64 (2019) 236–247. https://doi.org/10.1016/j.calphad.2018.12.010.

[79] M.J. Yao, K.G. Pradeep, C.C. Tasan, D. Raabe, A novel, single phase, non-equiatomic FeMnNiCoCr high-entropy alloy with exceptional phase stability and tensile ductility, Scr. Mater. 72–73 (2014) 5–8. https://doi.org/10.1016/j.scriptamat.2013.09.030.

[80] W.H. Liu, Y. Wu, J.Y. He, T.G. Nieh, Z.P. Lu, Grain growth and the Hall–Petch relationship in a high-entropy FeCrNiCoMn alloy, Scr. Mater. 68 (2013) 526–529. https://doi.org/10.1016/j.scriptamat.2012.12.002.

[81] N. Krasilnikov, W. Lojkowski, Z. Pakiela, R. Valiev, Tensile strength and ductility of ultra-fine-grained nickel processed by severe plastic deformation, Mater. Sci. Eng. A. 397 (2005) 330–337. https://doi.org/10.1016/j.msea.2005.03.001.

[82] M.J. Marcinkowski, H. Chessin, Relationship between flow stress and atomic order in the FeCo alloy, Philos. Mag. J. Theor. Exp. Appl. Phys. 10 (1964) 837–859. https://doi.org/10.1080/14786436408225388.

[83] O.N. Senkov, G.B. Wilks, D.B. Miracle, C.P. Chuang, P.K. Liaw, Refractory high-entropy alloys, Intermetallics. 18 (2010) 1758–1765. https://doi.org/10.1016/j.intermet.2010.05.014.

[84] S. Sheikh, S. Shafeie, Q. Hu, J. Ahlström, C. Persson, J. Veselý, J. Zýka, U. Klement, S. Guo, Alloy design for intrinsically ductile refractory high-entropy alloys, J. Appl. Phys. 120 (2016) 164902. https://doi.org/10.1063/1.4966659.

[85] Y. Lu, Y. Dong, S. Guo, L. Jiang, H. Kang, T. Wang, B. Wen, Z. Wang, J. Jie, Z. Cao, H. Ruan, T. Li, A Promising New Class of High-Temperature Alloys: Eutectic High-Entropy Alloys, Sci. Rep. 4 (2014) 6200. https://doi.org/10.1038/srep06200.

[86] P. Shi, W. Ren, T. Zheng, Z. Ren, X. Hou, J. Peng, P. Hu, Y. Gao, Y. Zhong, P.K. Liaw, Enhanced strength–ductility synergy in ultrafine-grained eutectic high-entropy alloys by inheriting microstructural lamellae, Nat. Commun. 10 (2019) 489. https://doi.org/10.1038/s41467-019-08460-2.

[87] O.N. Senkov, S. Rao, K.J. Chaput, C. Woodward, Compositional effect on microstructure and properties of NbTiZr-based complex concentrated alloys, Acta Mater. 151 (2018) 201–215. https://doi.org/10.1016/j.actamat.2018.03.065.

[88] Z. Lei, X. Liu, Y. Wu, H. Wang, S. Jiang, S. Wang, X. Hui, Y. Wu, B. Gault, P. Kontis, D. Raabe, L. Gu, Q. Zhang, H. Chen, H. Wang, J. Liu, K. An, Q. Zeng, T.-G. Nieh, Z. Lu, Enhanced strength and ductility in a high-entropy alloy via ordered oxygen complexes, Nature. 563 (2018) 546–550. https://doi.org/10.1038/s41586-018-0685-y.

[89] Y. Zou, H. Ma, R. Spolenak, Ultrastrong ductile and stable high-entropy alloys at small scales, Nat. Commun. 6 (2015) 7748. https://doi.org/10.1038/ncomms8748.

[90] R. Soler, J.M. Molina-Aldareguia, J. Segurado, J. LLorca, Effect of Misorientation on the Compression of Highly Anisotropic Single-Crystal Micropillars, Adv. Eng. Mater. 14 (2012) 1004–1008. https://doi.org/10.1002/adem.201200019.

[91] R. Labusch, A Statistical Theory of Solid Solution Hardening, Phys. Status Solidi B. 41 (1970) 659–669. https://doi.org/10.1002/pssb.19700410221.

[92] R.L. Fleisgher, Solution hardening, Acta Metall. 9 (1961) 996–1000. https://doi.org/10.1016/0001-6160(61)90242-5.

[93] I. Toda-Caraballo, A general formulation for solid solution hardening effect in multicomponent alloys, Scr. Mater. 127 (2017) 113–117. https://doi.org/10.1016/j.scriptamat.2016.09.009.

[94] M. Walbrühl, D. Linder, J. Ågren, A. Borgenstam, Modeling of solid solution strengthening in multicomponent alloys, Mater. Sci. Eng. A. 700 (2017) 301–311. https://doi.org/10.1016/j.msea.2017.06.001.

[95] C. Varvenne, G.P.M. Leyson, M. Ghazisaeidi, W.A. Curtin, Solute strengthening in random alloys, Acta Mater. 124 (2017) 660–683. https://doi.org/10.1016/j.actamat.2016.09.046.

[96] C. Varvenne, A. Luque, W.A. Curtin, Theory of strengthening in fcc high entropy alloys, Acta Mater. 118 (2016) 164–176. https://doi.org/10.1016/j.actamat.2016.07.040.